

Copy 2

SHORT-CRESTED WAVE FORCES ON A
RIGID SEGMENTED VERTICAL CYLINDER

By

ANDREW MALCOLM CORNETT

B.Sc., Queen's University at Kingston, 1983

A THESIS SUBMITTED IN PARTIAL FULFILLMENT OF
THE REQUIREMENTS FOR THE DEGREE OF
MASTER OF APPLIED SCIENCE

in

THE FACULTY OF GRADUATE STUDIES
Department of Civil Engineering

We accept this thesis as conforming
to the required standard

THE UNIVERSITY OF BRITISH COLUMBIA

October 1987

© Andrew Malcolm Cornett, 1987.

In presenting this thesis in partial fulfilment of the requirements for an advanced degree at the THE UNIVERSITY OF BRITISH COLUMBIA, I agree that the Library shall make it freely available for reference and study. I further agree that permission for extensive copying of this thesis for scholarly purposes may be granted by the Head of my Department or by his or her representatives. It is understood that copying or publication of this thesis for financial gain shall not be allowed without my written permission.

Department of Civil Engineering

THE UNIVERSITY OF BRITISH COLUMBIA
2075 Wesbrook Place
Vancouver, Canada
V6T 1W5

Date: October 1987

ABSTRACT

This thesis investigates water particle kinematics and the wave forces exerted on a slender rigid vertical cylinder in regular bi-directional wave fields. The instrumented portion of this cylinder is partitioned into nine independent segments enabling measurement of the vertical profile of hydrodynamic loading both in-line and transverse to the direction of wave propagation. Experiments conducted at the Hydraulics Laboratory of the National Research Council in Ottawa are described and some results are compared with the predictions of a wave force model based on the Morison equation and linear fluid kinematics. The influence of the crossing angle between the two wave components on the forces experienced by the column is determined.

These experiments consider short-crested wave behavior in intermediate and deep water resulting from the interaction of two identical regular wave trains crossing at angles of 30, 60 and 90 degrees. The limit corresponding to unidirectional monochromatic waves is also investigated to provide a reference condition for comparison with the short-crested results. Conditions at the location of maximum short-crested wave height are of primary interest, however, forces at locations between the anti-node and node of the flow are also examined. In all, water surface elevations, flow velocities, and wave forces were measured in 24 short-crested and 8 different long-crested wave conditions spanning the range of Keulegan-Carpenter number between 4 and 14.

The results of this study confirm the findings of previous researchers that short-crested waves with a certain period travel faster and rise higher before breaking than do their long-crested counterparts, but that in-line wave forces are not necessarily increased. Lift force maxima equal to half the maximum in-line force were measured; these forces can contribute significantly to the magnitude and direction of the total force resultant.

Table of Contents

ABSTRACT ii

Table of Contents iii

List of Tables vi

List of Photographs vii

List of Figures viii

Nomenclature xi

Acknowledgement xiv

1.0 INTRODUCTION 1

1.1 MOTIVE 1

1.2 LITERATURE REVIEW 2

1.2.1 Short-Crested Wave Theory 2

1.2.2 Instability Criterion 5

1.2.3 Studies on Short-Crested Wave Forces 8

1.3 RESEARCH OBJECTIVES 9

2.0 THEORETICAL BACKGROUND 11

2.1 SHORT-CRESTED KINEMATICS 11

2.2 WAVE FORCE MODEL 13

2.3 WAVE GENERATION 16

3.0 FACILITIES, INSTRUMENTATION AND EXECUTION 19

3.1 OFFSHORE WAVE BASIN 19

3.1.1 Physical Characteristics 19

3.1.2 Directional Wave Generator 19

3.1.3 Computerized Wave Machine Control 20

3.2 INSTRUMENT CONFIGURATION 21

3.2.1 Phase 1 21

| | |
|--|----|
| 3.2.2 Phase 2 | 22 |
| 3.3 INSTRUMENTATION | 23 |
| 3.3.1 Segmented Column | 23 |
| 3.3.2 Bi-directional Current Meters | 26 |
| 3.3.3 Wave Probes | 27 |
| 3.3.4 Video System | 27 |
| 3.3.5 Data Acquisition System | 27 |
| 3.4 INSTRUMENT CALIBRATION | 28 |
| 3.4.2 Current Meters | 28 |
| 3.4.3 Segmented Column Calibration | 29 |
| 3.5 WAVE SYNTHESIS | 30 |
| 3.5.1 Long-crested Waves | 32 |
| 3.5.2 Short-crested Waves | 32 |
| 3.6 TEST PROGRAM | 34 |
| <u>4.0 DATA PROCESSING AND ANALYSIS PROCEDURES</u> | 35 |
| 4.1 WATER SURFACE ELEVATION ANALYSIS | 37 |
| 4.2 CURRENT ANALYSIS | 38 |
| 4.3 FORCE ANALYSIS | 40 |
| 4.3.1 Force Coefficients Analysis | 41 |
| 4.3.2 Segmental Force Analysis | 44 |
| 4.3.3 Total Force Analysis | 45 |
| <u>5.0 RESULTS AND DISCUSSION</u> | 47 |
| 5.1 GENERAL OBSERVATIONS | 49 |
| 5.2 COMPARISONS WITH THEORY | 52 |
| 5.2.1 Water Surface Elevation Data | 52 |
| 5.2.2 Kinematics Data | 53 |

| | |
|--|----|
| 5.2.3 Force Coefficient Data | 54 |
| 5.2.4 Lift Forces | 56 |
| 5.2.5.Total Forces | 59 |
| 5.3 COMPARISON BETWEEN TESTS | 62 |
| 5.3.2 Influence of Crossing Angle | 62 |
| 5.3.3 Influence of Location | 64 |
| 5.3.4 Importance of Lift Forces | 66 |
| <u>6.0 CONCLUSIONS AND RECOMMENDATIONS</u> | 67 |
| 6.1 CONCLUSIONS | 67 |
| 6.2 RECOMMENDATIONS FOR FURTHER STUDY | 70 |
| BIBLIOGRAPHY | 71 |
| APPENDIX A | 75 |
| APPENDIX B | 78 |
| TABLES | 80 |
| PHOTOGRAPHS | 88 |
| FIGURES | 92 |

List of Tables

| | PAGE |
|--|------|
| <i>Tables begin on page 80.</i> | |
| <i>Table 4.1: Phase 2 Wave Characteristics Data.</i> | 80 |
| <i>Table 5.1: Crossing Wave Superposition Characteristics Data.</i> | 81 |
| <i>Table 5.2: Measured and Predicted Velocities Under Long-Crested Waves.</i> | 82 |
| <i>Table 5.3: Force Coefficient Estimates from Predicted Kinematics in Long-Crested Waves.</i> | 83 |
| <i>Table 5.4: Inertia Coefficient Estimates from Measured Kinematics.</i> | 84 |
| <i>Table 5.5: Lift Force Data.</i> | 85 |
| <i>Table 5.6: Predicted and Measured Total In-Line Force Maxima.</i> | 86 |
| <i>Table 5.7: Repeatability Data.</i> | 87 |

List of Photographs

| | <i>PAGE</i> |
|--|-------------|
| <i>Photographs begin on page 88.</i> | |
| <i>Photograph 1.1: General View of the Offshore Wave Basin and A Regular Short-Crested Wave Field.</i> | <i>88</i> |
| <i>Photograph 3.1: View Along the Top of the Segmented Wave Machine.</i> | <i>88</i> |
| <i>Photograph 3.2: Close-Up View of the Phase 1 Test Apparatus.</i> | <i>89</i> |
| <i>Photograph 3.3: View of the Phase 2 Test Apparatus.</i> | <i>89</i> |
| <i>Photograph 3.4: Close-Up View Down Into One Segment.</i> | <i>90</i> |
| <i>Photograph 3.5: The Author Conducting an Initial Condition Calibration Test.</i> | <i>90</i> |
| <i>Photograph 5.1: View of Short-Crested Waves and the Segmented Column.</i> | <i>91</i> |

List of Figures

| | PAGE |
|--|------|
| Figures begin on page 92. | |
| Figure 2.1: Definition sketch of crossing wave flow. | 92 |
| Figure 2.2: Water particle orbits under crossing waves (from Fuchs, 1951). | 93 |
| Figure 2.3: Definition sketch of oblique wave generation. | 94 |
| Figure 3.1: Plan of the Offshore Wave Basin. | 95 |
| Figure 3.2: Plan of instrumentation during phase 1. | 96 |
| Figure 3.3: Plan of instrumentation during phase 2. | 97 |
| Figure 3.4: Sketch of the segmented column. | 98 |
| Figure 3.5: Initial condition test response of transducer 4-X. | 99 |
| Figure 3.6: Initial condition test response of transducer 4-Y. | 100 |
| Figure 3.7: Plot of wave characteristics used during phase 2. | 101 |
| Figure 4.1: Wave time series and characteristics measured during test MRE2. | 102 |
| Figure 4.2: In-line wave profile snapshots from test MB32. | 103 |
| Figure 4.3: Transverse wave profile snapshots from test MB32. | 104 |
| Figure 4.4: Raw current meter data from test SN53. | 105 |
| Figure 4.5: Measured and predicted current characteristics and time series from test MN53. | 106 |
| Figure 4.6: Raw X axis force data from test SN64. | 107 |
| Figure 4.7: Raw Y axis force data from test SN64. | 108 |
| Figure 4.8: Kinematic and force time series used to obtain force coefficients from segment 5 during test SN64. | 109 |
| Figure 4.9: Total X, Y and resultant force time series from test SC17. | 110 |
| Figure 4.10: In-line and transverse force profiles from test SC17. | 111 |
| Figure 4.11: Comparison plot of total force and force profiles from test SC17. | 112 |

| | PAGE |
|--------------|---|
| Figure 5.1: | Raw X axis force data from test SC17. 113 |
| Figure 5.2: | Raw Y axis force data from test SC17. 114 |
| Figure 5.3: | Plot of short-crested wave celerity versus component wave celerity. 115 |
| Figure 5.4: | Measured and predicted forces for segments 1-8 from test SN53. 116 |
| Figure 5.5: | Plot of C_m versus KC data from segments 1-5. 117 |
| Figure 5.6: | Plot of C_d versus KC data from segments 6-9. 118 |
| Figure 5.7: | Published C_m and C_d values from 'U-tube' tests (from Sarpkaya and Isaacson, 1981). 119 |
| Figure 5.8: | Plot of C_L versus KC. Data from segment 3. 120 |
| Figure 5.9: | Plot of f_R versus KC. Data from segment 3. 121 |
| Figure 5.10: | X and Y axis force time series responses from segment 3 at 5 locations in the same short-crested flow. 122 |
| Figure 5.11: | Total force comparison plot from test SC34. 123 |
| Figure 5.12: | Plot of measured and predicted maximum positive total in-line forces. Data from all tests. 124 |
| Figure 5.13: | Total force comparison plot from test SB15. 125 |
| Figure 5.14: | Plot of total dimensionless in-line force maxima versus crossing angle. 126 |
| Figure 5.15: | Plot of dimensionless in-line force maxima from segments 1 and 2 versus crossing angle. 127 |
| Figure 5.16: | Plot of total dimensionless in-line force maxima versus phase between the two component waves. 128 |
| Figure 5.17: | Plot of dimensionless in-line and transverse force maxima from segments 1 and 2 versus phase between the two component waves. 129 |
| Figure 5.18: | Ratio of maximum lift force to in-line force from segment 3 versus wave period. 130 |

| | | |
|-------------|--|-----|
| Figure A.1: | Responses from initial condition testing in-line with the X axis of segment 4. | 131 |
| Figure A.2: | Responses from initial condition testing oblique to the X and Y axes of segment 4. | 132 |

Nomenclature

| | |
|-----------------|--|
| B | Width of wave generator segment. |
| C_F | Dimensionless force coefficient. |
| C_d | Drag force coefficient. |
| C_L | Lift force coefficient. |
| C_m | Inertia force coefficient. |
| D | Diameter of segmented cylinder. |
| F | Force. |
| F' | Force per unit length. |
| F^T | Total force. |
| H | Wave height. |
| KC | Keulegan-Carpenter number. |
| L | Wave length in the direction of propagation. |
| Re | Reynold's number. |
| S | Wave steepness ($= H/L$). |
| T | Wave period. |
| Q | Amplitude of resultant fluid velocity |
| U | Amplitude of fluid velocity in x direction. |
| V | Amplitude of fluid velocity in y direction. |
| a | Wave amplitude. |
| c | Wave celerity. |
| c_g | Group wave celerity. |
| c_t | Damping of a transducer. |
| d | Depth of water. |
| f_N | Natural frequency of free vibrations. |
| f_r | frequency ratio. |
| $f_1 \dots f_6$ | Force parameters. |
| g | Acceleration due to gravity. |
| k | Wave number in the direction of propagation. |
| k_t | Stiffness of a transducer. |
| k/D | Roughness. |
| l | Wave length of regular short-crested flow perpendicular to the direction of propagation. |
| m | In-line short-crested wave number. |

| | |
|-----------------------------|--|
| m_t | Mass of a transducer. |
| n | Transverse short-crested wave number. |
| r | A wave number parameter ($= [m + n]$). |
| t | Time. |
| (x,y,z) | Cartesian co-ordinate system. |
| (x_{ref},y_{ref}) | Co-ordinates of the test area within the Offshore Wave Basin |
| (u,v,w) | Components of fluid velocity. |
| $(\dot{u},\dot{v},\dot{w})$ | Components of fluid acceleration. |
| s,s,s | Displacement, velocity and acceleration of a transducer. |
| $ F_r $ | Amplitude of force resultant. |
| Δt | A time interval. |
| $\Delta\phi$ | A phase relation between two crossing long-crested waves. |
| ΦF_r | Direction of force resultant. |
| α | Total crossing angle. |
| β | Frequency parameter ($= Re/KC$). |
| γ | A parameter representing wave phase information. |
| η | Water surface elevation. |
| θ | Direction of wave propagation. |
| ν | Kinematic viscosity of water. |
| ζ | Damping ratio of a transducer. |
| ω | Angular frequency of a wave train. |
| π | Pi ($=3.14752\dots$). |
| ρ | The density of water. |
| σ | An error term. |
| ϕ | The phase of a wave train. |

Subscripts

| | |
|-------|---------------|
| c | Component. |
| L | Lift. |
| lc | Long-crested. |
| max | Maximum. |
| m | Measured. |
| p | Predicted. |

sc *Short-crested.*
seg *Segment.*
x *In the x direction.*
y *In the y direction.*

Acknowledgement

The author wishes to express immense gratitude to the staff of the Hydraulics Laboratory at the National Research Council of Canada in Ottawa for their advice and assistance throughout this project. Thanks are also extended to the Council and the Hydraulics Laboratory for the use of their facilities and the opportunity to conduct research in a state-of-the-art environment.

The author would also like to thank his supervisor, Dr. Michael Isaacson, for his guidance and encouragement throughout the preparation of this thesis.

Financial support from the Natural Sciences and Engineering Research Council of Canada and the National Research Council of Canada is gratefully acknowledged.

1.0 INTRODUCTION

1.1 MOTIVE

Short-crested waves are surface gravity waves with a crest length in the order of the wave length in the direction of propagation. These waves are common in nature; they occur in all water depths and are often ordered in a regular pattern such that the water surface profile perpendicular to the direction of propagation is somewhat periodic. From above, the water surface is characterized by a regular honeycomb or diamond pattern of alternating crests and troughs. Short-crested waves can result from a number of mechanisms. They can be directly generated by strong winds which are spatially varied in their turbulent intensity. They can also result indirectly from interactions between long-crested waves caused by diffraction around the end of a large structure, oblique reflection on vertical or sloping surfaces, differential refraction across shoaling bathymetry and cross propagation between two waves travelling in different directions, possibly originating from different sources.

Previous researchers have identified that short-crested waves travel faster and can have higher wave heights and crest elevations before breaking than their long-crested counterparts. These waves are thus a potential hazard to marine structures. Short-crested waves can also lead to more extensive suspension of bottom sediments, and have been held responsible for nearshore sediment circulation cells observed along many partially reflective shorelines, and particularly, adjacent to vertical seawalls.

An image of regular short-crested waves generated in the laboratory is presented in photograph 1.1. These waves were produced through the interaction of two identical long-crested wave trains propagating across each other. The water particle kinematics vary spatially in three dimensions but, along with the water surface elevation, are periodic in line with and normal to the direction of propagation. In

the limit where the crossing angle approaches zero, this wave field reduces to that of a unidirectional progressive wave. In the other limit, as the crossing angle approaches 180 degrees, the wave field becomes a series of standing waves. Both of these limit states are comparatively well understood.

The traditional approach to the design of coastal and offshore structures often considers only the incidence of a long-crested wave and, in some situations, the effects of standing waves generated by normal reflection from a vertical or steeply sloping wall. Real seas are, however, more often short-crested than not and the consideration of these waves can be of great importance in the success of coastal and offshore engineering works. Despite their prevalence in nature, short-crested waves have received relatively little attention in laboratory investigation and engineering design. This may be the result of a lack (until recently) of research facilities capable of generating short-crested seas and the complexity of wave theory required to accurately simulate the extensive nonlinearities associated with short-crestedness.

Complete understanding of the mechanism and affects of the complex short-crested flow condition, including the forces exerted on a rigid vertical slender cylinder, will enhance our ability to safely and effectively design for the marine environment.

1.2 LITERATURE REVIEW

1.2.1 Short-Crested Wave Theory

Many researchers have considered solutions to the short-crested wave problem. Most have approached the exact solution by approximating the nonlinear interaction of two regular waves to successive orders of accuracy via a Stokes type perturbation scheme. This style of approach is inherently most suited to deeper water.

Jeffreys (1924) introduced the term *short-crested* to characterize wave systems that are periodic in two orthogonal directions (in the direction of propagation and along the wave crest) in which the associated wavelengths are of the same order of magnitude.

Fuchs (1952) obtained a second order solution for water of an arbitrary finite depth based on the work of Stokes (1847). This was extended to third order by Chappellear (1961) who used a formal power-series expansion involving a parameter proportional to the wave steepness in the direction of propagation of the short-crested waves. This yielded a solution in dimensional form which did not converge towards standing waves as the crossing angle approached 180 degrees. Hsu, Tsuchiya, and Silvester (1979) obtained a different third order solution by recalculating the perturbation expansion in a nondimensional form using the steepness of the component, rather than the short-crested, waves. This solution has the advantage that it encompasses all crossing angles including the limits for standing and two-dimensional progressive Stokes waves.

These same authors (Hsu et al (1980)) have applied their theory to the prediction of sediment transport due to the short-crested waves found adjacent to a reflective sea wall. Their third order solution has been recast in terms of wave height by Fenton (1985) and applied to the study of pressures on a seawall due to obliquely incident waves.

A numerical approach has been pursued by Roberts and Shwartz (1983) and Roberts (1983). They have used a Fourier approximation to numerically solve a high order perturbation expansion in wave steepness.

All of these researchers have restricted their investigations to the interactions of two identical waves. Although specific predictions vary, these theories indicate that short-crested waves travel faster, have higher wave heights and crest elevations before breaking, and can

be up to sixty percent steeper than long-crested waves in the same water depth.

A recent paper by LeMehaute (1986) confirms these conclusions pertaining to the highest short-crested wave by considering only the planes containing the loci of free surface elevation peaks in a periodic short-crested wave field rather than developing a theory for the whole three-dimensional space. He argues that, "the maximum characteristics of a short-crested wave (resulting from the interaction of two identical waves crossing at an angle) are those of two-dimensional waves, provided the wave length is taken as the distance between (short-crested) peaks, and the wave height is twice the height of the primary components." He goes on to present the maximum possible free surface elevation of the peak of short-crested waves as a function of relative depth and crossing angle, assuming the breaking criterion based on Stokes' theory for limit waves applies to the short-crested situation.

Miles (1977) studied obliquely interacting solitary waves, which may approximate short-crested waves in the extreme shallow water limit, and classified these interactions as 'mild' or 'strong' depending on the degree of nonlinearity involved. Mild interactions are those in which the parent waves undergo only a transient change, whereas strong interactions are those where the degree of nonlinearity is such that the parent waves suffer semi-permanent change as a result of the interaction. He found that two solitary waves of small height to depth ratio, H/d , could interact at certain crossing angles such that a third wave was created whose celerity must be greater than that of either of the two incident waves.

Halliwell and Machen (1981) consider short-crested breaking waves in shallow water. They conclude that the interaction wave proposed by Miles not only travels faster, but is higher than either of the two incident waves and can attain a higher wave height before instability triggers wave breaking. This is in complete agreement with the

theoretical results pertaining to Stokes waves obtained by the researchers mentioned previously.

1.2.2 Instability Criterion

Waves dissipate energy primarily through wave breaking. This mechanism controls the maximum wave height, water surface elevation, and wave steepness of any wave form, including short-crested waves, in a particular marine environment. Since these maximum wave characteristics are of great interest to coastal and ocean engineers, information concerning the wave breaking mechanism, and particularly, the criterion governing the onset of wave breaking, is of critical importance.

Wave breaking begins when a wave becomes unstable. Two principal instability criteria have been proposed in the literature; they are referred to as 'kinematic' and 'dynamic', after Dean (1968). The kinematic instability condition, applicable to the forward breaking of a progressive wave, has been traditionally taken to correspond to the limit at which the horizontal particle velocity at the wave crest becomes equal to the wave celerity as initially proposed by Stokes (1880). Recent advances concerning the accurate numerical description of breaking waves indicate that this criterion may only be approximate.

The dynamic breaking criterion, applicable to the vertical instability of a pure standing wave, is given by the limit at which the vertical water particle acceleration at the wave crest exceeds the acceleration due to gravity.

Miche (1944) gives the maximum steepness of a progressive wave as $H/L = 0.142 \tanh(kd)$ for water of finite uniform depth. This simple expression serves as a useful engineering approximation over a wide range of depths, but in shallow water should be replaced by the prediction of solitary wave theory, $H/d = 0.83$, given first by Yamada (1957).

Penny and Price (1952) give the maximum standing wave steepness in deep water to the fifth order as $H/L = 0.218$. By considering this result and the laboratory data of Danel (1952), Wiegel (1964) proposed the following simple expression for the steepness of a standing wave $H/L = 0.218 \tanh(kd)$ which is of the same form as the progressive wave limit given above.

The instability criterion for short-crested waves is likely to progress from kinematic to dynamic as the crossing angle between the two primary wave components interacting to form the short-crested wave field is increased. Exactly how this transition takes place is not well understood.

Precise estimates of breaking wave heights are available for the specific case when the two incident wave trains are identical. LeMehaute (1986) and Roberts (1983) provide theoretical estimates of the maximum short-crested wave amplitude. LeMehaute's predictions cover the full range of relative depths and crossing angles whereas Roberts' more detailed theory is only valid for deep water.

Laboratory research concerning short-crested breaking waves has not been extensive. Halliwell and Machen (1981) describe a short series of experiments in which short-crested waves formed by the interaction of a regular incident wave train and its oblique reflection from a vertical wall were observed to break as they shoaled up a sloping wooden beach. They present their results in terms of short-crested breaking wave height versus water depth at breaking and conclude that short-crested breaking waves are higher than the maximum expected breaking waves according to design guidance based on two-dimensional progressive wave results, and that, "a plunging short-crested wave can occur where existing design guidance indicates that a spilling wave would be expected for that wave steepness and beach slope." This second result is significant because plunging breakers

initiate more sediment suspension and exert greater impact forces than do all other types of breaking waves.

Another study concerning short-crested wave breaking in shallow water is reported by Watanabe, Hara, and Horikawa (1984). They developed a new breaker index diagram for the onset of breaking in a compound wave train from the conventional one (pertaining to progressive waves) by converting the governing parameter from the ratio between breaker depth and deep-water wave height into the ratio between orbital velocity at a wave crest and wave celerity. Small scale model tests conducted in a narrow flume indicate that these new breaker indices give satisfactory estimates of the onset of breaking for short-crested waves.

Machen (1984) describes a series of experiments involving the generation of short-crested breaking waves through the interaction of two progressive wave trains propagating in water of uniform depth. He presents results relating short-crested breaking wave steepness to relative water depth at a crossing angle of 70 degrees which indicate that the limiting steepness of these waves approximates the limiting steepness of standing waves over a range of intermediate relative depth, confirming the prediction of Roberts (1983) that deep water short-crested waves could be up to sixty percent steeper than progressive waves. The second half of Machen's paper concerns the measurement of water particle velocities within the breaking wave crests. His interesting results indicate that for the same conditions mentioned above, the ratio of horizontal water particle velocity at the crest to the short-crested wave celerity is less than one. This would imply that at breaking the traditional kinematic stability criterion had not been exceeded, but concurs with the results of Dean (1968) who finds, from an investigation of progressive wave instability using stream function theory, that the velocity ratio (horizontal water particle velocity at the wave crest divided by wave celerity) corresponding to the normally accepted wave breaking limit (given as $H/d=0.78$) is

roughly 0.75 in both shallow and deep water; substantially less than the value of unity often quoted in the literature.

1.2.3 Studies on Short-Crested Wave Forces

The Morison equation is often used to estimate the wave force on slender structural members where the presence of the body does not significantly affect the incident flow kinematics. This formulation assumes the wave force to be comprised of a linear inertial component and a nonlinear drag component. Numerous experiments (summarized by Sarpkaya and Isaacson (1981)) have been conducted with long-crested waves to validate the Morison equation and to determine appropriate values of the drag and inertia coefficients. Results indicate that these coefficients depend primarily upon the Reynold's number, Re , and Keulegan-Carpenter number, KC , of the flow, as well as the relative roughness of the cylinder. The applicability of the Morison equation to three dimensional flow conditions, and short-crested waves in particular, has not been thoroughly explored.

Research concerning the impact forces of nearly breaking waves on a vertical cylinder indicate that very steep waves create two additional forces which dramatically increase wave loading. These additional forces arise from the impact of the steep, breaking wave front against the cylinder and the difference in water levels between the lee and stoss sides of the cylinder during this impact. Sawaragi and Nochino (1984) report that during their experiments concerning the forces of nearly breaking waves on a slender vertical cylinder they measured a total load up to seven times as large as the value predicted by the Morison equation alone.

Kjeldsen (1982) serves as an excellent review of the interesting work carried out at the Norwegian Hydrodynamic Laboratories concerning the generation of violent breaking freak waves by spatial and temporal superposition of wave solitons. These dangerous short-crested waves are the result of a complex interaction between many individual waves

travelling at different speeds in different directions. They represent the most severe wave conditions possible in a design sea state and are thus of particular interest to designers of coastal and offshore structures.

Proper application of the Morison equation relies on an accurate description of the water particle kinematics in the absence of the cylinder. In short-crested waves generated through the interaction of two progressive waves crossing at an angle, these kinematics can be roughly approximated by the linear superposition of the kinematics from each incident wave, or more accurately estimated from a nonlinear theory such as that of Hsu et al (1979). When the short-crested wave impacting the cylinder is near breaking, the additional forces relating to free surface effects must be included in the analysis. These have been found to depend on the shape of the breaking wave front, the breaking pattern, and the spatial relationship between the breaking point and the cylinder. Since short-crested waves can be higher and up to sixty percent steeper than long-crested waves before becoming unstable, it is likely that these additional terms will be even more significant for short-crested breaking waves than for their long-crested counterparts.

1.3 RESEARCH OBJECTIVES

A review of the literature has revealed a lack of experimental data concerning the forces exerted by short-crested waves on structures. This thesis represents an attempt to partially fill this void. Two main objectives were identified for a program of laboratory tests;

- (1) investigate the effect of short-crestedness on wave forces,
- (2) determine the applicability of the Morison equation to the prediction of these forces.

Short-crested waves were generated in the Offshore Wave Basin, of the Hydraulics Laboratory at the National Research Council of Canada in Ottawa through the interaction of two identical regular wave trains propagating across each other at specific angles. Forces were obtained by a rigid vertical column instrumented to measure two perpendicular horizontal force components at nine different elevations. A range of short-crested flow conditions were achieved by changing the height and period of each component wave and the crossing angle between them. The location of the column within the flow was controlled by the relative phase between the two component waves. Long-crested waves were also utilized as a bench-mark for comparison with the short-crested results.

The scope of these tests was limited to the investigation of non-breaking waves. Although breaking waves are known to lead to much larger wave forces than non-breaking waves, it was felt that the objectives of this study could best be achieved through consideration of relatively stable flow conditions. Two significant advantages associated with the study of only non-breaking waves are that fluid kinematics throughout the wave can be reliably predicted by theory, and free surface effects, such as wave impact loading and runup, are often small enough that they can be ignored without significant error.

A logical extension of the work documented in this thesis is verification of the breaking wave force data obtained by Kjeldsen and his co-workers at Trondheim.

2.0 THEORETICAL BACKGROUND

This thesis investigates short-crested waves produced from the interaction of two identical regular wave trains propagating across each other. Critical parameters defining this flow condition are sketched in Figure 2.1. Two identical components, each with wave height, H_C , and period, T_C , cross at a total angle, α , creating a short-crested wave train with height, H_{SC} , propagating in the direction bisecting the angle between the two components. The diamond pattern of crests and troughs resulting from this interaction is temporally and spatially regular. A cartesian co-ordinate system (x,y,z) is defined so that short-crested waves travel in the positive x direction and z is taken upwards from the still water level. The origin of this co-ordinate system moves in the direction of short-crested wave propagation at the speed of the short-crested wave celerity so that the wave form does not change with time. For all α , the short-crested wave height, wave length and wave celerity will be greater than that of the component waves; however, the wave period remains unchanged. From geometry, $L_{SC} = L_C/\cos(\alpha/2)$, while the distance in the y direction between vertical planes containing short crested wave peaks is $l = L_C/(2\sin(\alpha/2))$. Also, the short-crested wave celerity is given by $c_{SC} = c_C/\cos(\alpha/2)$ which can be rewritten as $c_{SC} = \omega/(k\cos(\alpha/2))$ where ω and k represent the angular frequency and wave number respectively of a component wave.

2.1 SHORT-CRESTED KINEMATICS

Many theories of varying order have been developed to quantify the kinematics within the regular short-crested wave field defined above. The most simple of these, linear short-crested theory, assumes the short-crested kinematics to result from linear superposition of the kinematics of the two component waves. Scalar quantities such as wave height are summed while vector quantities such as velocity are added vectorially. The linear equations presented below are after Fuchs (1952).

In-line and transverse wave numbers are defined as $m = 2\pi/L_{SC}$ and $n = 2\pi/l$ respectively with $r^2 = m^2 + n^2$. (Refer to Figures 2.1 and 2.2 for a visual representation of these terms.) The first order surface profile is

$$\eta = \frac{H_{SC}}{2} \sin(mx) \cos(ny) \quad 2.1$$

The components of water particle velocity (u, v, w) are

$$u = \frac{gH_{SC}}{2c} \frac{\cosh[r(d+z)]}{\cosh(rd)} \sin(mx) \cos(ny)$$

$$v = \frac{gnH_{SC}}{2cm} \frac{\cosh[r(d+z)]}{\cosh(rd)} \cos(mx) \sin(ny) \quad 2.2$$

$$w = \frac{grH_{SC}}{2cm} \frac{\cosh[r(d+z)]}{\cosh(rd)} \cos(mx) \cos(ny)$$

Several significant results emerge from such a straightforward analysis. Firstly, water particle kinematics are, in general, three dimensional, but reduce to two dimensions at specific locations. Figure 2.2, taken from Fuchs (1952) depicts several typical first order particle orbits within a short-crested wave field. Secondly, along each vertical plane paralleling the x axis where the combined wave crest is a maximum, the velocity component in the y direction vanishes. At these locations, kinematics are two dimensional. Thirdly, even though the celerity of the short-crested resultant is always greater than the celerity of a component wave, the same is not true for water particle velocities in the direction of wave propagation. According to linear theory, $u_{SC} = 2u_c \cos(\alpha/2)$ which implies that the in-line short-crested velocity is less than the component in line velocity when the crossing angle exceeds 120 degrees.

In situations where the wave steepness and/or wave height to water depth ratio is large, a higher order theory is required to accurately describe water particle kinematics.

Short-crested waves generated through the interaction of two progressive long-crested wave trains propagating across each other can be thought of as a combination of progressive and standing waves. In vertical planes containing the wave height maxima aligned in the direction of short-crested propagation, the fluid kinematics and water surface elevation characteristics resemble those of a progressive wave. However, transverse to the direction of propagation, the short-crested kinematics mimic those of standing waves. Extending this standing wave comparison, anti-nodes can be defined along lines containing progressive wave height maxima while nodes can be defined along lines between anti-nodes where the two component waves cancel each other out and little movement of the water surface is realized. The locations of nodes and antinodes are identified in Figure 2.1.

2.2 WAVE FORCE MODEL

A complete three-dimensional force model for a rigid vertical pile should account for temporally varying drag, inertia and lift forces. Lift forces are associated with vortex shedding and act transverse to the direction of fluid flow. In short-crested waves, each of these three forcing mechanisms can, in general, act both in-line and transverse to the direction of wave propagation during a wave period. Where steep or breaking waves are encountered, the additional effects of wave runup, impulsive wave impact and negative pressure gradient across the cylinder must be considered. These factors contribute to a hydrodynamic loading situation that is very complex, highly variable, and consequently, rather poorly understood.

Predictive models of wave force are thus generally restricted to the loading induced by 'green water' flows. General practice calls for a designer to define the harmonically oscillating kinematics of the flow condition in question and then use some formulation of the Morison equation to predict wave force. For two dimensional flow, this

relationship gives the in-line force per unit length experienced by a cylinder as:

$$F' = \frac{1}{2} \rho D C_d u |u| + \frac{\pi D^2}{4} \rho C_m \dot{u} \quad 2.3$$

Both the coefficients of drag, C_d , and inertia, C_m , have been shown to depend on the Reynold's number, $Re = UD/\nu$, and Keulegan-Carpenter number, $KC = UT/D$, of the flow and the relative roughness, k/D , of the cylinder, where U is the amplitude of in-line velocity.

The maximum harmonic lift force transverse to the direction of fluid flow is given, in terms of force per unit length, by:

$$F'_L = \frac{1}{2} \rho D C_L U^2 \quad 2.4$$

where C_L is the lift coefficient which like C_d and C_m also varies with Re , KC and k/D .

Three-dimensional flow requires a more general form of the Morison equation where fluid kinematics are resolved into orthogonal components normal to the cylinder. For a rigid vertical cylinder in a flow characterized by two orthogonal horizontal velocity components, $u(t)$ and $v(t)$, the forces per unit length in the x and y directions are

$$F'_x = \frac{1}{2} \rho D C_d |q| u + \rho \frac{\pi D^2}{4} C_m \dot{u} \quad 2.5$$

$$F'_y = \frac{1}{2} \rho D C_d |q| v + \rho \frac{\pi D^2}{4} C_m \dot{v}$$

with $q(t) = [u(t)^2 + v(t)^2]^{1/2}$.

Ideally, drag and inertia coefficients specific to the flow conditions in each direction should be used, (KC and Re usually differ in the x and y directions because of the difference in velocity amplitude) however, because of inherent imprecision in the estimation of drag and inertia coefficients such consideration is not warranted.

These two orthogonal force components can be combined vectorially to yield the magnitude, $|F_r|$, and direction, ΦF_r , of the force resultant according to

$$|F_r| = [F_x^2 + F_y^2]$$

2.6

$$\Phi F_r = \tan^{-1} [F_y / F_x]$$

The lift force on a vertical cylinder in three-dimensional flow can also act in all directions throughout a cycle, but at any one time will be roughly normal to the instantaneous velocity. The maximum lift force can be resolved into two components given by:

$$F'_{Lx} = \frac{1}{2} \rho DC_{Lx} QV$$

2.7

$$F'_{Ly} = \frac{1}{2} \rho DC_{Ly} QU$$

where Q represents $q(t)$ evaluated at the time when either $u(t)$ or $v(t)$ equals U or V . The lift coefficient in each direction should be based on directionally specific KC and Re numbers.

Total forces can be predicted by integrating Morison's equation from the mud line ($z = -d$) to the free surface ($z = \eta$), using appropriate kinematics at each level. Even though drag and inertia coefficients are known to vary over the height of the column, constant representative values are most often used. For two-dimensional flow in the x direction, this model can be written:

$$F_x^T = \frac{1}{2} \rho DC_d \int_{z=-d}^{z=\eta} u |u| dz + \frac{\pi D^2}{4} \rho C_m \int_{z=-d}^{z=\eta} \dot{u} dz \quad 2.8$$

or in discretized form,

$$F_x^T = \frac{1}{2} \rho DC_d \sum_{i=1}^N u_i |u_i| \Delta z + \frac{\pi D^2}{4} \rho C_m \sum_{i=1}^N \dot{u}_i \Delta z \quad 2.9$$

Similar expressions can be developed for three-dimensional flow.

Assuming that the maximum lift force per unit length in a particular direction occurs at the same instant in time along the whole column, the maximum lift force components per unit length can also be integrated over the entire column to give the total lift force maxima:

$$F_{Lx}^T = \frac{1}{2} \rho D \int_{z=-d}^{z=\eta} C_{Lx} V^2 dz$$

2.10

$$F_{Ly}^T = \frac{1}{2} \rho D \int_{z=-d}^{z=\eta} C_{Ly} U^2 dz$$

Some uncertainty arises when linear theory is used to evaluate fluid kinematics at elevations above the still water level where the flow is not explicitly defined. Several extensions to linear theory have been proposed to approximate fluid kinematics within a wave crest including, extrapolation of the fluid velocity profile upwards from the mean water level, assumption of a constant velocity within a wave crest equal to the mean water level velocity and vertical stretching of the linear theory profile to fit the instantaneous free surface. The second technique, assumption of a constant velocity within a wave crest equal to the mean water level velocity is favored because it has been found to give reasonable results, its prediction falls between the other two and is very easy to implement.

2.3 WAVE GENERATION

The desire to create short-crested waves in the offshore wave basin through the superposition of two identical obliquely propagating long-crested components necessitated the development of specialized wave synthesis software to generate driving signals for each of the 60 segments in the wave machine.

A definition sketch showing some of the generator segments and part of the wave basin is shown in Figure 2.3. A cartesian co-ordinate

system is imposed in which the origin is coincident with the midpoint of the first segment and the x axis extends into the basin orthogonal to the wave machine. The following development will identify the motions of each segment of the wave generator required to produce specific short-crested waves at the test location having co-ordinates (x_{ref}, y_{ref}) , based on the snake principle discussed by Isaacson (1984).

The short-crested wave field at any position (x, y) and time t can be defined using linear theory by an expression for the instantaneous water surface elevation resulting from the superposition of two long-crested components, $\eta = \eta_1 + \eta_2$ where:

$$\eta_1(x, y, t) = a_1 \cos[k_1 x \cos(\theta_1) + k_1 y \sin(\theta_1) + \phi_1 - \omega_1 t] \quad 2.11$$

$$\eta_2(x, y, t) = a_2 \cos[k_2 x \cos(\theta_2) + k_2 y \sin(\theta_2) + \phi_2 - \omega_2 t]$$

For the special case of two identical component waves, where $a_1 = a_2$, $k_1 = k_2$, $\omega_1 = \omega_2$, $\theta_1 = +|\theta|$ and $\theta_2 = -|\theta|$:

$$\eta = a \cos(\gamma_1 - \omega t) + a \cos(\gamma_2 - \omega t) \quad 2.12$$

where

$$\begin{aligned} \gamma_1 &= kx \cos(\theta) + ky \sin(\theta) + \phi_1 \\ \gamma_2 &= \gamma_1 + \Delta\phi \end{aligned} \quad 2.13$$

and $\Delta\phi$ represents the spatially dependent phase difference between the two components at the test area given by

$$\Delta\phi = \phi_2 - \phi_1 - 2ky_{ref} \sin(\theta) \quad 2.14$$

The planes of constant y where the two waves interact in phase and superpose constructively are identified by $\Delta\phi=0$ and given by:

$$y_i = \frac{\phi_2 - \phi_1}{2k \sin(\theta_i)} \quad ; \quad \theta_i = i2\pi\theta \quad , \quad i = 1, 2, 3, \dots \quad 2.15$$

More significantly, re-arrangement of equation 2.14 gives the phase of the second wave component, ϕ_2 , required to achieve any desired phase relationship (specified by $\Delta\phi$) with the first component at any location in the basin.

$$\phi_2 = \Delta\phi + \phi_1 + 2ky_{\text{ref}} \sin(\theta) \quad 2.16$$

These expressions, together with those presented by Isaacson (1984) relating water surface elevation to board motion, have been incorporated into a computer program designed to synthesize the driving signals required to generate short-crested waves.

3.0 FACILITIES, INSTRUMENTATION AND EXECUTION

3.1 OFFSHORE WAVE BASIN

3.1.1 Physical Characteristics

All experiments were conducted in the Offshore Engineering wave basin at the Hydraulics Laboratory of the National Research Council in Ottawa, Canada. This state-of-the-art facility is 50m wide, 30m long, and 3m deep. A new 60 segment, multi-mode, directional wave generation machine occupies a 30m portion along the north wall of the basin. The working area for this study was reduced to a 30m by 19.2m rectangle by the location of a partition and the intrusion of wave absorbing devices along three sides of the basin as shown in Figure 3.1.

The wave absorbing devices are comprised of multiple vertical layers of perforated metal sheeting. The porosity of each layer decreases into the absorber. Jamieson (1987) has documented the development and performance of these unique wave absorbers. Extensive testing of the 6.75m absorber opposite the wave generator indicates that reflection coefficients in the order of 5% are achieved for waves up to 0.7m in height over a range of wave period from 1 to 3 seconds.

3.1.2 Directional Wave Generator

The 60 segment directional wave machine in the Offshore wave basin became operational in April, 1986. A picture of the machine is presented in Photograph 3.1. For the first 10 months, only long-crested waves normal to the wave machine could be generated over its entire length. The full potential of the machine to generate random multi-directional waves lay dormant awaiting the complete implementation of the distributed, micro-processor based, direct digital control system. De-bugging of this control system was delayed because it could not proceed concurrently with ongoing testing in the basin. Full directional generation capability was first achieved in March 1987.

The tests documented in this thesis were performed during March and April and were the first to utilize the directional capabilities of the new wave generation system. There were several unforeseen challenges associated with being the first user of the new system, but there was also the significant reward of being the first to apply the full potential of this advanced Canadian technology.

Directional long-crested waves are generated through the controlled snake-like movement of the segmented wave board. Each of the 0.5m wide segments in the NRC machine is supported and moved independently by its own articulation mechanism. Precise co-ordination and control of these independent segments is essential in order to achieve authentic reproduction of desired wave conditions in the basin. Adjustment of each control linkage mechanism enables the paddles to move in either piston mode, hinged flapper mode, or a combination of both. This flexibility enables the profile of board motion to closely approximate the variety of velocity profiles found in shallow and deep water waves. Closely matching the velocity boundary condition reduces spurious cross-mode wave activity resulting from excess input of energy to the water.

Each segment is driven by a MOOG hydraulic actuator with a stroke of 0.2m and a rated static force of 45kN. Mechanical stroke amplification is achieved by means of a lever arm. The 60 actuators are driven by a hydraulic power supply consisting of six pumps, each rated at 50 USGM and driven with a 75kW motor. Steep short-crested waves up to 1m in height have been generated by this machine operating in 2m of water.

3.1.3 Computerized Wave Machine Control

Control of the wave generation system originates from the host computer, an Hewlett-Packard 1000F minicomputer operating under the RTE IVB software executive system. An on-line control program named SWG allows the user to operate the machine by entering simple commands.

To make waves, the user must first synthesize a driving signal file in GEDAP format for each of the 60 paddles in the wave machine. An extensive range of two- and three-dimensional wave generation software exists as part of the GEDAP package to help carry out this driving signal synthesis. Various SWG commands allow the user to initialize the system, calibrate the wave machine, download the driving signal for each segment, start and stop the generation of waves, and adjust the span controlling the amplitude of paddle motions.

3.2 INSTRUMENT CONFIGURATION

This study explores the interaction between crossing regular long-crested waves and the forces exerted by the short-crested resultant on a rigid surface piercing cylinder. Laboratory testing took place in two stages. The first phase was concerned with determining characteristics of the flow without the cylinder while the second phase dealt mainly with the measurement of wave forces.

3.2.1 Phase 1

The purpose of phase 1 testing was to:

- (1) quantify the interaction of two identical regular long-crested waves crossing at specific angles,
- (2) measure the characteristics of the resulting short-crested waves including their height, period, celerity, steepness, asymmetry, profile, and internal kinematics,
- (3) define the driving signals to be used with the segmented column in phase 2.

The arrangement of instrumentation within the basin during phase 1 is depicted in Figure 3.2. A 'T' shaped array containing 13 wave probes was installed so that the intersection of the longer x and shorter y axes of the array lay coincident with the future location of the segmented column. This intersection point was 9.0m away from the

centerline of the wave machine. Two additional wave probes were located ahead of this array, one each 5m to either side of the centerline of the basin. These probes were positioned to record the individual long-crested components coming from each side of the wave machine before any interaction took place.

Each wave probe is approximately 1.0m long and was positioned to record crest elevations up to 0.6m above the mean water level. All wave probes were mounted to a horizontal beam supported above the water by vertical posts held rigid by numerous guy wires. This apparatus can be seen in Photograph 3.2.

Two bi-directional electro-magnetic current meters were installed below the intersection of the 'T' shaped array. These were positioned to measure water particle velocities in the horizontal plane at two elevations 1.08m and 1.68m above the floor of the basin. These elevations correspond to the midpoints of the first and third segments of the column. This arrangement enabled measured forces to be directly related to measured kinematics. Each current meter was held rigidly in place by a specially designed, non-electrically conductive mounting bracket as shown in the image in Photograph 3.2. These brackets reduced but did not eliminate the amount of electrical interference recorded by the current meters.

In total, 15 wave probes and 2 current meters were used in the first phase of this study.

3.2.2 Phase 2

The primary objective of the second phase of testing was to measure the forces exerted by specific short-crested waves on the segmented column. The waves to be used in phase 2 were identified and accurately measured in phase 1.

The configuration of equipment within the basin for phase 2 of the testing program differed only slightly from that in phase 1. The segmented column was positioned at the intersection of the 'T' array, oriented so that the 181N load cells would record forces in the direction of wave propagation while the 72.5N load cells would detect transverse forces. Figure 3.3 contains a plan view sketch of instrumentation within the basin during this phase, while photograph 3.3 shows an overall view of the instrumentation within the basin. The two bi-directional current meters were kept at the same elevations (coincident with the midpoints of segments 1 and 3) but were moved 24cm ahead of the stoss face of the column. Several wave probes were removed, leaving a shortened 'T' shaped array of 10 gauges to fill out the remaining complement of 32 available data acquisition channels.

3.3 INSTRUMENTATION

3.3.1 Segmented Column

The segmented column is a research tool intended to simulate a rigid, surface piercing cylindrical structure and provide information concerning the forces exerted on it due to hydrodynamic loading. Information concerning such loading can be applied to a pile, a structural member of a larger construction, or any similar slender vertical rigid body in the marine environment.

The column is 17cm in diameter and 2.4m long, of which the upper 1.5m is instrumented to measure forces. The force sensitive portion is divided into 9 independent segments of varying length. The two lower segments are each 35cm in length, the two middle segments measure 15cm and the upper five segments are each 10cm long. Non-uniform segmentation of the column in this manner ensures that the net force per segment under hydrodynamic loading is approximately the same. A sketch of the column is depicted in Figure 3.4.

Each segment contains two load cells arranged at right angles which measure orthogonal components of the total force exerted normal to the cylindrical surface. Both load cells are mounted on and react against a rigid circular base plate located near the bottom of a segment. The cylindrical outer shell of each segment is made from rigid lightweight seamless aluminum pipe and is supported above its base plate by a delicate network comprised of 5 slender rods and associated fittings. Each of the base plates is fitted with three rigid vertical sleeves rising just above the height of the external shell of the segment. These sleeves are designed to fit a support structure within the column and allow adjacent segments to remain independent when stacked one on top another. The inner workings of a typical segment can be seen in plan in photograph 3.4.

Three of the slender rods suspend the shell over the base plate, restricting the motion of the shell relative to the base plate in vertical translation and rotation about both horizontal axes. The two remaining slender bars provide the horizontal connection between the shell and the two load cells. All horizontal loading normal to the outside surface of the cylindrical shell, regardless of the elevation at which the loading is applied, is transmitted through these two bars to the two load cells which react against the rigid base plate, enabling forces to be registered by the load cells. No stiffening mechanism other than the 5 slender rods mentioned previously is provided to restrict torsional vibration of the shell about its vertical axis. Torsional vibration was seen as a potential problem should the cylinder be subjected to horizontal forces with a component tangential to the surface of the shell. The frequency of the torsional vibrations was determined during calibrations of the column so that their effect could be extracted from any record using digital filtering techniques during post processing if required. Filtering was not used in processing of the force records because very little excitation in the torsional mode was realized and the force signals were generally not significantly corrupted by noise.

The nine segments described above are held firmly in place to form a column by a rigid support structure consisting of a 61cm square, 1.6cm thick, steel base plate and a 61cm square, 0.7cm thick, steel top plate connected by three 2.0cm diameter, 2.45m long steel rods running the length of the column. Once the segments were stacked, the three steel rods running through them were post-tensioned against the three sleeves to increase the rigidity of the whole assembled structure.

The 18 load cells in the segmented column are manufactured by 'Innerpac'. They each contain a 'wheatstone bridge' electrical circuit bonded to a machined metal surface. Small strains in the metal, produced by external forces, change the relative resistance across adjacent arms of the bridge. This change in resistance is registered as a change in electrical potential across the arms of the bridge once the circuit is charged. Thus, forces resulting in mechanical strains are accurately and reliably converted into changes in electrical potential which can be readily monitored by data acquisition equipment.

The load cells oriented in the direction of wave propagation (the x direction) have an individual rated capacity of 181N while those oriented transversely are rated at 72.5N. Experience indicates that these load cells can be safely loaded up to 150% of their rated capacity. (Mogridge, personal communication.) The load cells have a combined non-linearity and hysteresis of 0.05% and a non-repeatability of +/- 0.01% of the rated full scale range. Temperature drift of the load cells is negligible.

Sealing the segmented column against water intrusion was necessary to prevent damage to the load cells and internal cabling. Another important concern was to keep the mass of each segment as low as possible so that the lowest natural frequency of vibration of the segment remained greater than the predominant excitation frequencies of the hydrodynamic loading.

Several alternative waterproofing strategies were investigated involving various materials and adhesives where the goal was to achieve a reliable seal while minimizing the coupling between axes and adjacent segments. After assembly, the entire column was wrapped in a sleeve of transparent vinyl bonded to non-instrumented portions of the column near the bottom and top. As a back-up measure should leakage occur, provision was made within the column for a suction tube. During testing, this tube was attached to a self priming pump external to the column. No evidence of leakage was discovered throughout the tests, however, some corrosion did occur induced by condensation within the column.

3.3.2 Bi-directional Current Meters

Two 'Marsh-McBirney' 512 OEM were used in this study to measure water particle kinematics. The instrument relies on the Faraday principle of electromagnetic induction to measure the magnitude of water velocity in two orthogonal directions. Simply stated, the sensor generates a magnetic field and records the voltage change resulting from the flow of water. Because these units are very sensitive to the presence of metallic objects near the sensor head and any nearby electrical conductors, they are best suited to the measurement of currents in the field. The signal conditioning within these instruments was designed for optimum performance over the frequency range normally found within prototype ocean waves, and reflected the designers bias towards field measurement. Use in the laboratory required reliable performance over a higher frequency range. To achieve this, a low-pass filter was removed from the internal electronics of both instruments prior to their calibration. Special mounting brackets were constructed out of bakelite, a suitably non-electrically conductive material, which held the sensors rigidly in place far enough away from metal support structures to minimize electrical interference in their operation.

3.3.3 Wave Probes

Capacitive wire wave probes were used to measure instantaneous water surface elevation. This type of gauge is used extensively and with great success throughout the NRC Hydraulics laboratory. Water level measurements made with these probes are accurate to within $\pm 1.0\text{mm}$, and are not influenced by spray above the continuous air/water interface.

3.3.4 Video System

All tests made with the segmented column in place were recorded by a video camera located along the east wall of the basin. The images from this camera were displayed on a video monitor and recorded on video tape. Playback of this video record in slow-motion reveals many interesting details concerning the interaction between the column and incident wave. Runup on the stoss face of the pile is particularly well revealed.

3.3.5 Data Acquisition System

The data acquisition system at the NRC hydraulics lab enables continuous analog signals flowing from a variety of instruments, including force transducers, current meters, and wave probes to be sampled at equally spaced intervals of time and eventually stored on computer in a data file as digital time series. Amplification and low-pass filtering of the analog signal in each channel is often included to minimize aliasing problems associated with the sampling operation.

The GEDAP buffered data acquisition system used in this study consists of the following components.

- Hewlett-Packard 1000F minicomputer operating under the RTE IVB software executive system,

- Neff Instrumentation Corporation data acquisition and control hardware,
- NRC GEDAP instrument conditioning rack,
- NRC GEDAP buffered data acquisition system software package.

An amplifier gain of 200 was applied to the analog signal from each force transducer in the segmented column. Analog low-pass filtering of the amplified response was executed using 2-pole Butterworth filters with a cut-off frequency of 10Hz. During a test, 32 channels were each sampled 40 times per second for a duration of 20 seconds. Much higher sampling rates can be achieved with the available equipment, but were not considered necessary.

3.4 INSTRUMENT CALIBRATION

3.4.1 Wave Probes

The wave probes were calibrated by raising the gauges through distances of 20cm and 40cm in still water. A 3 point quadratic polynomial calibration was calculated for each probe. In all cases, the second order term was less than 0.0022m/V, indicating that the probes were fairly linear. The offset value for each probe was obtained at the beginning of each day of testing.

3.4.2 Current Meters

Both bi-directional current meters were dynamically calibrated under waves in a 1.22m wide flume against a laser doppler anemometer and the predictions of linear theory. The response of the current meters in seven regular waves spanning the range of period from 0.67s to 2.80s and five irregular waves with average periods between 1.49s and 2.02s was investigated. In most cases, the current meters generated nearly identical readings but over predicted fluid velocity by varying amounts. No specific dependence between current meter calibra-

tion factor and wave period was identified, however, some variation with current magnitude is suggested by the data. A revised linear calibration factor of 0.5443m/s/V was established for both axes of the two current meters.

3.4.3 Segmented Column Calibration

The static and dynamic behavior of all segments (including coupling between axes and between segments, and the torsional response to tangential loading) was explored, both before and after waterproofing the column with an external layer of transparent polyvinyl. A more detailed account of these calibration tests is included in Appendix A.

Calibration of the transducers along both the x and y axes took place with the column lying horizontal, resting on the edges of the two square end plates designed specifically for this purpose. In addition to loading each axis in-line, both axes were simultaneously loaded at 45 degrees by one suspended weight. Tests of this type served to calibrate the load cells in each segment and verified the column's ability to accurately measure the components of a force applied in any direction.

The dynamic response characteristics of each transducer in the segmented column were identified by a form of calibration known as the initial condition test. Photograph 3.5 shows the author performing a calibration of this type. A 1.82kg mass is suspended from an aluminum single point loading rig by a single strand of piano wire. An oxy-acetylene torch is used to abruptly cut this wire without introducing unwanted vibrations to the segment just after sampling has begun. The free vibration response of both axes of the pre-loaded segment as well as adjacent segments on either side are sampled by the data acquisition for 5 seconds at a frequency of 400 Hz.

Figures 3.5 and 3.6 depict the response from initial condition tests conducted on the x and y axes of the column's fourth segment. In

this test, the segment is loaded by a static force of 20.1N resulting from gravity acting on the loading frame and the suspended 1.82kg mass. (Offsets have been taken on each channel to account for the self weight of the segment shell.) After approximately 0.5 seconds, the piano wire suspending the mass is abruptly severed, suddenly reducing the applied load to 2.3N. Careful execution of this test ensures that the segment is excited in only one mode of vibration, thus avoiding complexities in the free vibration response resulting from vibrational cross-coupling. The response of the transducer to this sudden change in loading is virtually instantaneous, however, a significant amount of overshoot is recorded as part of the free vibrations initiated within the transducer. This result is indicative of a stiff transducer with a moderate degree of damping and is typical of those obtained from other transducers within the column.

Final static calibration values were obtained immediately before installation of the segmented column in the wave basin. A mass of 20.01N, including the aluminum loading frame, was used. Second order polynomial calibration of the x axis was achieved by loading each segment in both the positive and negative sense. Differences in first order calibration value of up to 1.34 N/V in the x direction and 1.57 N/V in the y direction were realized between these and earlier calibration trials. These values represent changes of 8% and 20% respectively and apply to the transducers in segment 9. The calibration values for the transducers in the other segments remained more consistent with results obtained previously.

3.5 WAVE SYNTHESIS

Wave synthesis in the Offshore Wave Basin involves the creation of driving signals for each of the 60 independent wave boards that comprise the segmented wave generator. Each driving signal is a digital time series which specifies the location of a wave board every 0.1 seconds. Driving signals are created and stored as GEDAP data files on the HP1000 mini-computer.

The present study initiates the investigation of regular short-crested waves produced by the superposition of two long-crested waves crossing at a range of angles between 0 and 90 degrees. To generate these waves, the wave machine was partitioned into two sections, each responsible for the generation of one oblique long-crested wave. This approach has certain advantages.

- (1) Each long-crested wave can be generated and measured independent of its symmetrically opposed component enabling the superposition of the two waves to be studied.
- (2) Reflections from the side walls and side beaches are reduced because less wave energy is directed towards them.
- (3) Wave heights at the face of the machine, particularly at locations corresponding to anti-nodes in the short-crested wave pattern, are kept to moderate levels because there is no portion of the wave machine contributing energy to both wave components. This reduces the chances of cross-mode wave activity in front of the wave boards and wave breaking between the wave machine and the test area.

One disadvantage associated with this partitioned generation technique is that wave diffraction (essentially energy loss along the crest of a propagating wave from a region of greater wave height towards areas of lesser wave height) can reduce the height of each wave component realized at the test area. The resulting short-crested wave is still produced by the interaction of two identical long-crested waves crossing at a certain angle, but the wave heights and propagation directions of these components are no longer exactly those generated at the wave machine.

Existing wave synthesis software did not allow for partitioning of the wave machine or superposition of driving signals. Two new GEDAP wave synthesis programs were written to achieve this capability.

3.5.1 Long-crested Waves

The test program included 8 long-crested waves spanning the range of wave period from 1.69 to 2.83 seconds. Driving signals were synthesized based on the participation of all wave machine segments. Application of these driving signals led to waves which, in 7 out of 8 cases did not match the desired characteristics at the test location. Visual observation of the waves and inspection of the measurements recorded by many of the wave probes revealed that the long-crested waves were subject to significant spatial variabilities. Wave characteristics at the future location of the segmented column were of particular interest, so the driving signals were re-synthesized to achieve a satisfactory match between desired and measured wave characteristics at that site.

The reason(s) for the rather poor initial replication of the desired long-crested waves is not yet completely understood, however, several possibilities have been identified. One of these relates to the implementation of the new digital control system for the wave machine. The computer software used to generate driving signals for a regular wave train had not been updated to account for the differences in the performance of the wave machine under this new control system.

3.5.2 Short-crested Waves

Short-crested waves were created through the interaction of two identical regular long-crested waves propagating across each other at specific angles. Crossing angles of 30, 60 and 90 degrees were included in the test program. Long-crested waves propagating at angles of 15, 30 and 45 degrees to the wave machine were required to satisfy these requirements.

Location of the segmented column was selected through consideration of the diffraction expected to occur during the propagation of a 45 degree wave. A site 9.0m away from the wave machine was found to be

satisfactory, ie, the height and direction of propagation of a long-crested wave at 45 degrees was not significantly affected at this location.

Synthesis of driving signals for the generation of short-crested waves proceeded according to the partitioning technique described above. For waves crossing at 30 and 60 degrees, the generator was partitioned into two overlapping sections, each containing 40 segments. According to this scheme, the first 20 segments were dedicated to the generation of one long-crested component, the central 20 segments contributed to both components, and the last 20 segments contributed only to the second component wave. For waves crossing at 90 degrees, the generator was partitioned into two non-overlapping halves, each dedicated solely to the generation of one component wave.

One problem associated with the generation of regular oblique waves stems from the fact that energy input to the water assumes a component parallel to the face of the wave machine. If the side beaches are not perfectly absorbing, significant standing wave cross-mode activity can quickly establish itself, resulting in steady state conditions with a high degree of spatial variability. To reduce the significance of this problem, the test plan called for the generation and sampling of wave action in relatively short bursts before steady state conditions became fully established in the basin. Temporal modulation of each driving signal was built into the synthesis software to achieve these short bursts of wave activity. All driving signals were synthesized based on a 70 second record length. Within this duration were:

- a 30 second duration of full span,
- two 10 second durations for ramp-up and ramp-down,
- a variable lag time dependent on the paddle location, the wave group velocity, and the propagation direction,
- and a quiescent duration to fill out the record length.

Measurements are obtained over a duration of 20 seconds starting as soon as fully developed wave heights are observed at the test area.

3.6 TEST PROGRAM

Development of a test plan was dictated in part by the experimental apparatus. The 2.4m column height and its design water depth of 2.0m fixed the upper wave height limit to 0.7m. Experience with long-crested wave generation in the basin at that wave height indicated that the maximum wave height to wavelength ratio that could be achieved was approximately 0.1.

Starting with restrictions such as these, a test plan evolved consisting of 28 unique flow conditions, including 8 long-crested and 20 short-crested waves, that would discern the influence of short-crestedness on the forces measured at the column. The wave period and total wave height actually achieved for each of these 28 tests are presented graphically in Figure 3.7. The test plan enables many direct comparisons between various tests. For example, 11 different waves with a height near 0.67m and 8 different waves with a smaller height near 0.47m are specified.

In summary, phase 1 of the test program included the synthesis and measurement of the waves presented in Figure 3.7 and investigation of the superposition of long-crested waves crossing at angles of 30, 60 and 90 degrees in the absence of the segmented column. Phase 2 of the test program considered measurement of hydrodynamic forces on the segmented column driven by the long- and short- crested waves identified in phase 1. The two phases followed each other consecutively and were completed within a period of 3.5 weeks during March and April 1987.

4.0 DATA PROCESSING AND ANALYSIS PROCEDURES

This chapter describes the procedures used to extract useful information from the raw data collected during each test. Example outputs representing typical results are presented but few observations are discussed. Thorough discussion of the many interesting results identified by this work is reserved for Chapter 5.

In total, 100 unique measurement files were sampled during phase 1 of the test program while 32 files were obtained during phase 2. During phase 1, water surface elevation and current measurements were simultaneously obtained on 19 channels, 10 times a second for a duration of 20 seconds during each test. During phase 2, forces were included in the measurement scheme, raising the number of channels used to 32 and the sampling frequency to 40 Hz. At the end of each day of testing, all measurements were backed up on magnetic tape to ensure a secure, permanent record of the data collected.

The diverse analyses described in this chapter were all developed and applied as 'procedure files', essentially a collection of commands which enable the sequential execution of a number of GEDAP analysis programs and a plotting package. Many of the programs used in the following analyses existed at the hydraulics laboratory as part of the standard library of analysis programs. In addition to these, 10 programs were written or modified by the author to enable the unique analyses required by the current project. Procedure files are typically set up to execute repetitive analysis on a number of tests and are generally submitted over-night in batch form.

Detailed analysis was restricted to the 32 tests listed in Table 4.1 which include 8 long-crested waves, 19 unique short-crested flow conditions and 5 repeatability trials. These waves were identified during phase 1 and repeated during phase 2.

Water surface elevation and current analyses generally concentrate on the data collected during phase 1, while force analyses use the data collected during phase 2. The same driving signals were used in each test phase, thus the generated wave conditions can be considered to be identical. Comparison of some wave and current characteristics from corresponding tests in both phase 1 and phase 2 verify the similarity between the two trials.

Some processing operations were performed on all of the measured time series, regardless of their source. Program PDMLT was used to demultiplex the measured data into separate files each containing the data from one channel. Program SELPO was developed to select a portion of data equal to an integer multiple of the wave period. This is achieved by searching the record for the first and last occurrence of a particular event, such as up-crossing, down-crossing, maximum or minimum.

Several programs from the GEDAP analysis library were used often, but were not part of every procedure. Program AZCRN was used to perform zero-crossing analysis on water surface elevation and current records. An extensive set of average, significant and maximum characteristics are output by this program. Program XCR11 was used to calculate the cross-correlation function between two time series. An option allows the second time series to be shifted and recycled so that the cross-correlation between it and the first is maximized. Program RESMP is used to alter the intersample spacing within a record.

Discussion of the specific analyses performed is best organized according to the source of data under investigation. Accordingly, section 4.1 considers the analysis of water surface elevation records while section 4.2 deals with the analysis of current measurements and section 4.3 describes analyses involving the many force time series obtained during phase 2 of the test program.

4.1 WATER SURFACE ELEVATION ANALYSIS

The capacitance wave probes gave clean reliable signals that required no signal conditioning. Analysis procedures were developed to:

- 1) quantify various average wave characteristics including wave height, wave period, wave steepness, crest front steepness and vertical and horizontal asymmetry;
- (2) compare the wave profiles measured at various locations to give an indication of the spatial variability within the wave field;
- (3) present some of the measured time series in graphical form;
- (4) formulate successive snapshots of the wave profile along both the x and y axes by combining the information from various probes in a linear array.

A 'wave characteristics' analysis procedure was developed to achieve the first three objectives listed above. Figure 4.1 contains a typical example of the plot generated as output. Six key characteristics are summarized to the right of each time series plot. The location of the probes numbered in this figure are shown in Figure 3.2.

The wave characteristics at probe 15 are of particular interest because it is coincident with the location of the segmented column. The time series from other probes shown in Figure 4.1 cover a fairly large area in front and to either side of probe 15. Comparison between the time series pairs recorded at probes 7 and 9, 16 and 17, and 15 and 18, is particularly useful in revealing the spatial variability in the wave field, since under ideal circumstances, the waves recorded at each of the probes in these pairs should be identical.

Program AZCRN is designed to calculate wave characteristics for long-crested waves and relies on the linear estimate of wave length to

formulate wave steepness parameters. In crossing wave flows, the short-crested wave length is dependent on the crossing angle as well as wave height and period and is generally longer than the corresponding long-crested wave length. Program CSOLV was created to adjust the steepness characteristics estimated by AZCRN for the longer short-crested wave lengths. First, the average time taken for a group of wave crests to travel a known distance is determined by finding the time shift that maximizes the cross-correlation function generated between the two concurrent time series recorded at probes 18 and 15, which are known to be 2.57 meters apart. This information gives the short-crested wave celerity which, when multiplied by the period of the regular flow, leads to the wave length. Erroneous steepness estimates generated by AZCRN are then automatically corrected based on the proper short-crested wave length.

The fourth analysis objective, that of plotting a spatial domain profile of the water surface, both in-line and transverse to the direction of propagation, was achieved by two similar 'wave profile' procedures. Typical output from this procedure showing the progression with time of a wave through the frame defined by the linear array of probes oriented in the x direction (similar to the individual snapshots comprising a movie) is presented in Figure 4.2. The wave propagates from left to right within each frame, and the zero x-axis position corresponds to the location of probe 15 and the segmented column. The profile along the y axis for the same short-crested flow condition is presented in Figure 4.3.

4.2 CURRENT ANALYSIS

Current measurements obtained during both phase 1 and phase 2 were corrupted by electrical interference; because of this, their accuracy and reliability is in doubt. Figure 4.4 depicts a typical example of the unprocessed data recorded by both axes of both current meters under a regular long-crested wave. Channels 12 and 14 sense in the y direction and should indicate zero, while channels 11 and 13 should

sense a regular sinusoidal current. In this test, corruption manifests itself most noticeably as irregular high frequency noise on channel 11, but channel 13 is also affected. Unfortunately, the degree and frequency of corruption on each channel varies significantly from test to test making it difficult to extract through any generally applied technique.

An elaborate procedure was developed to salvage useful information from these corrupted records. The key program is called FLSCR, an acronym for frequency limited screening. FLSCR is a modified version of program SCREN, developed by Mansard (personal communication) in which oscillatory corruption is extracted from an irregular record, by successively fitting a sinusoid to the time series at the peak frequency of the energy spectrum and subtracting this component away from the record. Each cycle through the sinusoid fitting and subtraction operation, a new frequency component is extracted based on an updated spectrum. Program FLSCR incorporates the additional requirement that the selected frequency must fall within a certain user defined range for it to be extracted from the input record. In some cases, particularly where small velocities were recorded (most often the y channel of each current meter) low-pass filtering at a cut-off frequency of 2Hz was effective in eliminating low level random noise from the signal.

These two techniques were incorporated into procedures designed to determine current characteristics (such as the peak to peak velocity and the average period) and compare the current time series measured in the x direction (with noise extracted) to estimates from linear wave theory and non-linear Reinecker and Fenton stream function theory. A typical graphical result from one of these analyses depicting comparisons between measured current and the predictions of non-linear theory is presented in Figure 4.5. The processed measured kinematics retain a much reduced level of corruption compared to the raw data presented in Figure 4.4, but do not agree well with theoretical predictions.

4.3 FORCE ANALYSIS

Force measurements were successfully made during all 32 tests comprising the second phase of the test program. Unfortunately, the y direction transducers in segments 4 and 5 malfunctioned after the first 13 tests so that complete y direction force information was obtained in only long-crested and 30 degree crossing waves. All x axis transducers performed well throughout the entire test program. In spite of this malfunction, much useful information was obtained concerning the effect of short-crestedness on wave forces.

The raw unprocessed signals measured by all segments in the x and y axes during test SN64 (long-crested waves, $H=0.65\text{m}$, $T=2.83\text{s}$) are shown in Figures 4.6 and 4.7 respectively. These signals are relatively free of noise arising from free vibrations, or other sources such as electrical interference, and are typical of those measured throughout phase 2. Inspection of the raw force data from all 32 tests indicated that filtering would not be necessary. This is, no doubt, partly due to the fact that the nature of hydrodynamic loading under investigation is gradual rather than sudden. No dynamic breaking wave impacts are included in the test program, only gradually varying 'green water' wave forces.

Some of the responses in Figures 4.6 and 4.7 possess a non-zero offset which changes slightly between tests. The test procedure adopted during phase 2 included re-initialization of the zero force response for all transducers at the beginning of each day. In spite of this precaution, it would appear that small levels of time varying drift influence the forces measured during each test. Where these offsets are significant, compensation is achieved by subtracting an appropriate constant value from the whole force record using program VSCAD.

In a few tests, most segments appear to have been excited in the torsional vibration mode (discussed in Appendix A) although the mechanism through which this took place is unknown. Some evidence exists to indicate that the impact and runup of steep waves is responsible for this behavior, as ringing is most noticeable in tests with steep waves. Close inspection of these records indicate that the ringing has not affected the maximum force experienced on each segment during a cycle, only the temporal variation of force after the local maximum has been reached. Because of this, no attempt was made to filter or otherwise correct for this ringing response.

Several different analyses have been conducted using the force records measured by the segmented column. The purpose, methodology and a typical result from each will be briefly discussed in turn.

4.3.1 Force Coefficients Analysis

The poor quality of current measurements obtained throughout the test program precluded their extensive use in the determination of force coefficients for the segmented column in short-crested waves. However, a crude analysis using measured kinematics has been conducted to estimate inertia coefficients for segment 1 in all of the wave conditions tested in phase 2. In addition, drag and inertia force coefficients have been determined from the response of each segment to loading by all 8 long-crested waves and kinematics predicted by the non-linear numerical stream function theory of Reinecker and Fenton (1981). A least squares technique is used to find the values of C_d and C_m which minimize the total error between the force record measured in the x direction and the force predictions of Morison's equation (equation number 2.3).

The error term to be minimized, σ^2 , represents the difference between the measured force, F_m , and the predicted force, F_p , summed over the entire record and can be written as

$$\sigma^2 = \sum_{i=1}^N [F_m(t_i) - F_p(t_i)]^2 \quad 4.1$$

where N is the number of data points and F_p is given by the Morison equation. To find the values of C_d and C_m which minimize this error term, derivatives with respect to C_d and C_m are set equal to zero. Differentiating with respect to C_d yields:

$$\frac{\partial \sigma^2}{\partial C_d} = \sum_{i=1}^N 2 \left[F_{mi} - \frac{1}{2} \rho D C_d u_i |u_i| - \rho \frac{\pi D^2}{4} C_m \dot{u}_i \right] \cdot \left[-\frac{\rho D}{2} u_i |u_i| \right]$$

$$\sum_{i=1}^N -\rho D \left[F_{mi} - \frac{1}{2} \rho D C_d u_i |u_i| - \rho \frac{\pi D^2}{4} C_m \dot{u}_i \right] \cdot u_i |u_i| = 0$$

This can be expressed in the form:

$$f_1 = f_2 C_d + f_3 C_m \quad 4.2$$

Similarly, differentiating with respect to C_m yields:

$$\frac{\partial \sigma^2}{\partial C_m} = \sum_{i=1}^N 2 \left[F_{mi} - \frac{1}{2} \rho D C_d u_i |u_i| - \rho \frac{\pi D^2}{4} C_m \dot{u}_i \right] \cdot \left[-\frac{\rho \pi D^2}{4} \dot{u}_i \right]$$

$$\sum_{i=1}^N -\frac{\rho \pi D^2}{2} \left[F_{mi} - \frac{1}{2} \rho D C_d u_i |u_i| - \rho \frac{\rho \pi D^2}{4} C_m \dot{u}_i \right] \dot{u}_i = 0$$

This is also of the form:

$$f_4 = f_5 C_d + f_6 C_m \quad 4.3$$

Two simultaneous equations (numbers 4.2 and 4.3) emerge which are easily solved for the two unknown force coefficients:

$$C_d = \frac{f_1 f_6 - f_3 f_4}{f_2 f_6 - f_3 f_5} \quad 4.4$$

$$C_m = \frac{f_2 f_4 - f_1 f_5}{f_2 f_6 - f_3 f_5}$$

where:

$$f_1 = \sum_i F_{mi} |u_i| u_i$$

$$f_2 = \frac{1}{2} \rho D \sum_i u_i^4$$

$$f_3 = \rho \frac{\pi D^2}{4} \sum_i \dot{u}_i |u_i| u_i$$

4.5

$$f_4 = \sum_i F_{mi} \dot{u}_i$$

$$f_5 = \frac{1}{2} \rho D \sum_i \dot{u}_i |u_i| u_i$$

$$f_6 = \frac{\rho \pi D^2}{4} \sum_i \dot{u}_i^2$$

Fluid kinematics are predicted by stream function theory as developed by Reinecker and Fenton(1981). Segmental kinematics are evaluated at 10 elevations along each segment and integrated to yield time series representing the mean velocity and acceleration. Integration of the kinematics is necessary to accurately simulate the velocity and acceleration experienced by a segment when it is only partially submerged. Stream function wave theory was used in these investigations because it is thought to accurately predict the kinematics in steep waves up to the free surface. To ensure the proper phase relationship between measured force and predicted kinematics, the kinematics were matched to a water surface elevation time series recorded adjacent to the column.

Figure 4.8 depicts a typical graphical result generated from the force coefficients analysis of segment 5 during test SN64 (long-crested waves, $T=2.83s$, $H=0.65m$). The integrated theoretical kinematics used in the analysis are shown in the two time series towards the top of the Figure, while the bottom window contains both the measured in-line force and the force prediction of the Morison equation using the drag and inertia coefficients that minimize the total error. The force

coefficients extracted from the least squares analysis are printed immediately above the force time series along with the root mean squared error which serves as a measure of the goodness of fit between the measured and predicted forces.

As part of the force coefficients analysis scheme, Keulegan-Carpenter and Reynold's numbers were calculated for the flow condition at each segment during each test. The segmental Keulegan-Carpenter number is given by $KC_{seg} = U_{max}T/D$ while the segmental Reynold's number is $Re_{seg} = U_{max}D/\nu$ where U_{max} equals the maximum fluid particle velocity at the midpoint of the segment. When considering the column as a whole, Keulegan-Carpenter and Reynold's numbers at the mean water level are taken to be representative of the flow.

As mentioned previously, a few inertia coefficients have been determined from measured kinematics in both long- and short-crested waves using a crude technique based on relating force maxima to acceleration maxima. Estimates are obtained from forces measured on the x axis of segment 1 and currents measured on the lower current meter, located at the elevation of the segment midpoint. An inertia coefficient is obtained from:

$$C_m = \frac{4F_{max}}{\rho\pi D^2\dot{U}} \quad 4.6$$

where F_{max} is the maximum in-line force on segment 1 and \dot{U} is the maximum acceleration given by $\dot{U}=\omega U$; the maximum velocity multiplied by the angular frequency of wave action. Results from the application of this crude analysis, and comparisons with results from the more sophisticated least squares error minimization technique, are discussed in section 5.2.3.

4.3.2 Segmental Force Analysis

Force time series from those segments which remained submerged during all tests (numbers 1 and 2) were analyzed to obtain information

concerning the maximum force in each direction, the frequency of force oscillations, and the magnitude and direction of the force resultant. Comparison of these results between tests leads to an understanding of the effect of various parameters such as, crossing angle, relative depth, wave period and wave height on the forces experienced by a submerged member. By avoiding partially submerged segments, complications related to the difference in free surface effects between tests, such as runup, and crest front steepness, are excluded from the analysis.

The mean value of each force record was calculated and removed to ensure that different non-zero offsets did not affect the force maxima. This operation was thought to be particularly valid since only submerged segments were considered and the results were to be used in purely comparative analyses. The resultant force time series, $F_r(t)$, expressed in terms of magnitude, $|F_r|$, and direction, ΦF_r , by equations 2.6 were formed for each test. All three time series were then scanned for their maximum and minimum values. The frequency of oscillations in each direction were determined by computing the average period of the x and y force records.

4.3.3 Total Force Analysis

Total force analyses were conducted on the data recorded from all 32 tests performed in phase 2. The forces measured on each segment were summed over the whole column to give the total force experienced by the instrumented portion during a typical wave cycle. Segmental forces were also normalized with respect to segment height, giving force per unit length, and then plotted according to segment elevation to form the vertical force profile in both the in-line and transverse directions. Plots generated from the analysis of test SC17 (short-crested waves, $H=0.679\text{m}$, $T=2.755\text{s}$, $\alpha=30^\circ$) serving as examples of typical output, are presented in Figures 4.9 and 4.10. The first figure contains time series depicting the total in-line force, the total transverse force, and the magnitude and direction of the total

force resultant (where zero degrees corresponds to the positive x direction). The second figure depicts four wave force profiles extracted at key times within the wave cycle corresponding to x and y force maxima and minima.

Another analysis procedure was developed to compare measured in-line force time series and profiles to predictions based on the Morison equation. Linear theory was used to generate average short-crested kinematics (see section 2.1) at each segment. Kinematics within a wave crest are assumed equal to those at the still water level. Global (ie applicable to the whole column) drag and inertia force coefficients of $C_d = 0.7$ and $C_m = 1.7$ were determined from the analyses described in section 4.3.1. These values are assumed to apply to the entire column over the full range of flow conditions considered in the test program. Predicted force time series were calculated for each segment and then integrated over the column to yield total predicted forces. Figure 4.11 depicts the result of this analysis for the same test considered above. The measured and predicted in-line total force time series and vertical force profile are compared directly. In this case, the Morison equation force model is only a fair approximation of the measured forces.

5.0 RESULTS AND DISCUSSION

Consideration of the process whereby regular short-crested waves exert an unsteady force on a rigid vertical surface piercing pile reveals that the force magnitude per unit length must depend on 11 independent parameters in the form:

$$F' = f[\rho, g, \nu, H, L, \alpha, d, D, \Delta\phi, z, t] \quad 5.1$$

This relationship may be expressed in many dimensionless forms in which a non-dimensional force coefficient, C_F is dependent on eight dimensionless parameters. In one possible formulation, force per unit length is normalized with respect to wave height, cylinder diameter, fluid density and gravitational acceleration to form a force coefficient dependent on

$$\frac{F'}{\rho g H D} = C_F[Re, KC, \frac{H}{L}, \frac{d}{L}, \alpha, \Delta\phi, \frac{z}{d}, \omega t] \quad 5.2$$

Reynold's number, Keulegan-Carpenter number and angular frequency can all be expressed in terms of the original parameters using linear theory as follows. From the dispersion relation

$$\omega = \frac{2\pi}{T} = \left(\frac{2\pi g \tanh(2\pi d/L)}{L \cos(\alpha/2)} \right) \quad 5.3$$

In this problem, fluid velocity at the still water level is proportional to wave amplitude and can be expressed as

$$U = \frac{1}{2} \frac{\omega H \cos(\alpha/2)}{\tanh(kd)} \quad 5.4$$

An appropriate Reynold's number is

$$Re = \frac{UD}{\nu} = \frac{DH}{2\nu} \left(\frac{2\pi g \cos(\alpha/2)}{L \tanh(2\pi d/L)} \right) \quad 5.5$$

The Keulegan-Carpenter number can be written as

$$KC = \frac{UT}{D} = \frac{\pi H \cos(\alpha/2)}{D \tanh(kd)} \quad 5.6$$

If only force maxima on one segment over a wave cycle at locations corresponding to anti-nodes of the flow are considered, the last three terms in equation 5.2 drop out, leaving a force coefficient which theoretically depends on five dimensionless parameters.

Reynold's number incorporates the influence of fluid viscosity on a flow situation. Where oscillatory flow past a cylinder is of interest, the value of Reynold's number indicates the regime of flow in the near vicinity of the cylinder which is characterized by the type of boundary layer, the degree to which it is developed and its propensity to separate. These factors in turn have a dramatic effect on the drag, inertia and lift forces experienced by the cylinder. In this study, Reynold's numbers at the still water level vary between 1.2×10^5 and 1.5×10^5 . Under steady flow conditions, this range of Reynold's number would indicate a subcritical flow regime with a laminar boundary layer and fairly constant force coefficient values. In oscillatory flow, however, this range of Reynold's number corresponds to a critical regime in which the boundary layer around the cylinder is in transition from laminar to turbulent flow. Unfortunately, force coefficients tend to be rather variable over this critical domain.

The Keulegan-Carpenter number represents the ratio of wave amplitude to cylinder diameter and serves as a rough measure of whether wave forces are drag or inertia dominated. Within the flow conditions under investigation, this parameter varies between 7 and 14, indicating that drag and inertial forces are of comparable magnitude with inertia being more important in most cases.

Morison's formula is an engineering approximation to wave forces within this flow regime which ignores free surface effects and inherent interactions between viscous and inertial effects and assumes that the total force is the sum of independent inertial and drag components.

Results from this study indicate the extent of applicability of the Morison equation to short-crested flow conditions. With experimentally determined force coefficients and reasonable short-crested kinematics, the Morison equation can be used to effectively approximate total in-line wave force in situations where free surface effects and lift forces are relatively small.

Over the range of flow conditions included in the test program, results indicate that the force coefficient identified in equation 5.2 is most strongly influenced by the crossing angle between the two wave components. This parameter is thus most significant in the accurate estimation of non-breaking short-crested wave force. Dependence on wave steepness of the short-crested resultant and relative depth can also be discerned from the data obtained, although the influence of these parameters is less consistent and less pronounced. In particular, greater wave steepness leads to higher wave runup and the possibility of increased forces due to wave impact loading. This process is known to dominate the forces measured in very steep or breaking waves (Kjeldsen and Akre 1985). Wave impacts of this type were not specifically included within the current scope of work although a few events did occur. The primary focus of this discussion will, thus, be the effect of crossing angle and relative component wave phase on wave forces.

Results from each test are compared with theory and to the results from other tests to form a complete picture of the effects of short-crestedness on wave force. Specific observations applicable to all tests will be discussed in section 5.1. Comparisons with theory are presented in section 5.2 while section 5.3 contains the results of relative comparisons made between tests.

5.1 GENERAL OBSERVATIONS

Inspection of the video record obtained during each test shows that runup occurs on the stoss face of the column, accompanied by some

draw-down on the leeward face, with the passage of each wave crest. Runup is most pronounced during the passage of steep waves, approaching 15 percent of the incident wave height in some cases. The surface flow pattern around the column is often characterized by significant turbulence indicating that vortex shedding is taking place. Turbulence generated during the passage of a wave crest is typically dragged back past the column as the direction of flow is reversed during the following trough. Concurrent repeated vortex shedding and flow reversal leads quickly to a very complex turbulent flow situation.

Some observations relevant to most of the records can be made with reference to the set of typical raw force data obtained during test SC17 ($H=0.679\text{m}$, $T=2.755\text{s}$, $\alpha=30^\circ$) presented in Figures 5.1 and 5.2. Force values presented in these figures have not been normalized with respect to variable segment length and it is useful to keep in mind when inspecting these raw force records that segments 5 through 9 have 29% of the surface area of segments 1 and 2. The temporal force variation measured at each segment results from the combined effects of variable hydrodynamic loading and the degree of submergence. Lower segments remain totally submerged at all times while upper segments may be fully or partially submerged only during the passage of each wave crest.

Consider first the in-line (x axis) force data depicted in Figure 5.1. The data from all segments are regular and consistent over the 20 second record length. The relative importance of drag and inertial forces on any particular segment is revealed through the form of the force time series and the timing of the local force maxima. Inertial forces are proportional to fluid acceleration while drag forces are proportional to the square of velocity (with sign retained). Because harmonic acceleration precedes velocity by 90° (or $\frac{1}{4}$ of a wave period) inertia dominated force will peak slightly ahead of drag dominated force. Lower segments which remain fully submerged throughout each wave cycle (numbers 1, 2 and sometimes 3 depending on the wave height) experience positive and negative forces of nearly equal magnitude

resulting primarily from inertial effects. Those segments located near the mean water level and partially exposed during each wave cycle, (numbers 4, 5, 6 and sometimes 3) generally exhibit greater positive than negative forces resulting from the combined effects of drag and inertia. Upper segments (numbers 7, 8 and 9) are submerged for short durations under a wave crest coincident with maximum positive fluid velocities and small decreasing accelerations. These segments experience only force in the positive x direction dominated by viscous effects and are free from hydrodynamic loading for much of each wave cycle. The forces experienced by upper segments can be increased by free surface effects such as wave impact loading and variable hydrostatic pressure across the column which act in a very dynamic manner.

The typical y axis transducer responses depicted in Figure 5.2 also reveal some very interesting behavior. Significant lift force oscillations resulting from vortex shedding occur on most segments at roughly twice the wave frequency. These oscillations are less consistent than those in the x direction and are indicative of a less stable phenomenon. Fully submerged lower segments exhibit continuous force oscillations of moderate amplitude while partially submerged upper segments exhibit intermittent force oscillations of large amplitude, particularly when their shorter length (and thus, smaller surface area) is taken into account. This observation gives support to the lift force model of equation 2.4 in which the magnitude of lift force is proportional to the square of in-line fluid velocity. Where the duration of submergence is sufficient to allow a full cycle of lift force oscillation, positive and negative forces of near equal magnitude are recorded. Lift forces are also well correlated over the height of the pile, enabling a significant contribution to the maximum total force.

5.2 COMPARISONS WITH THEORY

5.2.1 Water Surface Elevation Data

Simultaneous generation of two independent long-crested waves propagating across each other at a specific angle effectively formed short-crested waves at the test area and also enabled examination of wave superposition. A photograph of a simulated regular short-crested wave field looking (in roughly the negative x direction) towards the wave machine is shown in Photograph 5.1.

During phase 1 of the test program, the left and right component waves of 15 different short-crested flow conditions (5 @ 30°, 60° and 90° crossing angle) were generated and measured on their own. Comparison between the component waves and the short-crested resultant reveals information concerning the formation of short-crested waves through wave superposition. Results from these tests are presented in Table 5.1. Several observations can be made.

- (1) In most cases, the left and right component waves are virtually identical.
- (2) At 30° total crossing angle, the short-crested wave height is, on average, 20 % less than the sum of the component wave heights indicating nonlinear superposition.
- (3) In all cases, both steepness parameters of the resultant short-crested wave are less than double that of each long-crested component. As well, the short-crested celerity is greater than the long-crested celerity. These trends are indicative of increased short-crested wave length.

Linear theory predicts that the increase in short-crested wave length results from the simple geometric relation $L_{SC} = L_C \cos(\alpha/2)$. This influences steepness through $S_{SC} = 2S_C \cos(\alpha/2)$, and celerity through $c_{SC} = c_C / \cos(\alpha/2)$. Figure 5.3 depicts a graphical comparison between component wave celerity and short-crested wave celerity at

three crossing angles including estimates from the celerity equation defined above. From the results depicted in this figure it would appear that the linear model is only an approximation to the actual relationship between the celerity of the short-crested and component long-crested waves.

Consecutive snapshots of water surface elevation profile in the x direction give a clear visual image of the propagating wave-form in the spatial domain which can be analyzed to reveal wave characteristics such as crest-front-steepness and wave length. A typical series of such images from test M32 ($H=0.672\text{m}$, $T=1.717\text{s}$, $\alpha=60^\circ$) are presented in Figure 4.2. This technique is most useful in the study of episodic or breaking waves where wave characteristics change quickly with time and position, and visual inspection of wave profile lends some insight into the phenomenon.

5.2.2 Kinematics Data

The velocity transverse to the direction of wave propagation measured under short-crested anti-nodes was very near zero in all cases, confirming the predictions of linear and non-linear theory that particle orbits lie in the vertical plane at this location. At nodes, however, in-line velocities approached zero, indicating particle orbits transverse to the direction of propagation, again confirming theoretical predictions. In between these two limiting conditions, varying degrees of combined x and y velocity were measured verifying the existence of three dimensional elliptical orbits.

Results of velocity measurements under eight long-crested waves are summarized in Table 5.2. Measured average peak-to-trough velocity and the predictions of linear and non-linear theory do not always agree well, reinforcing the uncertainty associated with measured kinematics. The disagreement is not consistent, eliminating the possibility that it results from an erroneous calibration value. One possible reason for the inadequate performance of the current meters in the basin compared

with their performance during calibration in the flume could be the difference in their relative proximity and orientation. In the flume, the sensor heads were side by side, whereas in the basin, they were positioned one above the other. It is reasonable to assume that the magnetic fields generated by the two sensor heads interfere with one another depending on their relative location. A difference in the geometry or magnitude of this interference could detrimentally affect the performance of both instruments.

Measured kinematics were not relied upon in subsequent analyses; predictions from the stream function theory of Reinecker and Fenton (1981) were used to determine kinematics in long-crested flow conditions while linear theory was used to estimate short-crested kinematics.

5.2.3 Force Coefficient Data

Figure 5.4 contains a set of time series representing the measured and predicted in-line forces on 8 segments of the column during one test with long-crested waves (SN53, in which $H=0.572\text{m}$, $T=2.504\text{s}$). The predicted segmental forces shown in this figure are generated according to the Morison equation using force coefficients that minimize the least squares error formulation presented in equation 4.1. Theoretical non-linear velocities and accelerations based on the numerical stream function theory of Reinecker and Fenton are used to model the long-crested kinematics at each segment. The good agreement realized between measured and predicted segmental forces, quantified by the RMS error term written above the time series for each segment, confirms that long-crested hydrodynamic loading above and below the still water line can be well modelled by the Morison equation. However, the variability in optimum C_D and C_m values over the height of the column reinforces the fact that these force coefficients are dependent on local flow conditions. Figure 5.4 reveals the quality of the match typically achieved in the time domain between the measured segmental forces and the best efforts of the Morison equation.

The least squares error minimization procedure whereby 68 estimates of each force coefficient were extracted from the data collected during 8 long-crested flow conditions is described in section 4.3.1. Complete results from this analysis are listed in Table 5.3. Included in this table are C_d and C_m estimates made from poorly conditioned data. For example, forces experienced by upper segments, (numbers 6, 7, 8 and 9) are known a priori to be drag dominated. Little inertia dependent force response exists; thus, meaningful inertia coefficients cannot be expected. Conversely, forces on lower segments (numbers 1, 2, 3 and 4) are inertia dominated, and thus, poorly suited to the estimation of drag coefficient. In light of this knowledge, C_m values from segments 1 to 5 and C_d values from segments 6 to 9 only have been plotted in Figures 5.5 and 5.6. Data from individual segments tend to be consistently above or below the mean, possibly indicating that force calibration values for particular segments are not quite what they should be or that actual kinematics differ from those assumed. In particular, segments 1 and 2 consistently give low C_m values while analysis of data from segment 3 leads to large values. Selection and application of 'mean' or 'global' force coefficients average out these deviations between segments.

Figure 5.7 depicts results of 'U-tube' tests presented by Sarpkaya (1976) spanning a range of frequency parameter, $\beta = Re/KC$ up to 5260. If these values are extrapolated up to the range of β above 10000 explored in the current study, one would expect, over the range of KC from 4 to 14, fairly constant force coefficients near $C_m = 2.0$ and $C_d = 0.7$. These numbers concur fairly well with the results presented in Figures 5.5 and 5.6.

Results from the crude inertia coefficient analysis based on force maxima measured by segment 1 and velocity maxima recorded by the lower current meter are presented in Table 5.4. The wave period, in-line force maximum and measured in-line velocity maximum for each test are listed along with calculated values of inertia coefficient, Keulegan-

Carpenter number, Reynold's number and frequency parameter. Estimates of C_m range from 1.10 to 1.52 and span a range of KC between 1.8 and 8.3. The assumption of inertia dominated hydrodynamic loading inherent in this crude analysis should be valid within this domain. Also included in Table 5.4 are estimates of C_m from the more sophisticated least squares error minimization procedure. In all but one out of eight tests with long-crested waves, the estimates of inertia coefficient based measured kinematics are greater than those based on predicted kinematics. This is not surprising, considering that the current meter was found to generally under predict peak-to-peak fluid velocities.

From analysis of the long-crested force data, mean values of $C_d = 0.7$ and $C_m = 1.7$ have been identified. In subsequent analyses aimed at estimating total forces on the column under loading by short-crested waves using Morison's equation, these 'global' force coefficient values are assumed to apply to the entire column over the full range of flow conditions encountered during phase 2 testing.

5.2.4 Lift Forces

In most tests, particularly those involving larger wave heights and periods above 2 seconds, considerable transverse forces were recorded on all segments. For the 28 tests based on either long-crested waves or short-crested waves in phase at the segmented column in which transverse kinematics are negligible, these transverse forces are the result of lift generated through vortex shedding. Figure 5.2 depicts a set of transverse force measurements obtained during loading by regular short-crested waves with characteristics $H=0.679m$, $T=2.755s$ and $\alpha=30^\circ$. The magnitude of lift forces measured on upper segments is modulated due to the limited duration of submergence. Even though in-line fluid velocities are large at these elevations, they act for such a short time that only partial eddy shedding takes place, with the result that lift forces are significantly reduced. Maximum lift forces tend to occur at or just below the mean water level, corresponding to

segments 3, 4 and 5, where in-line fluid velocities are high and vortex shedding has time to fully develop during each wave cycle.

For comparison with published data, the amplitude and frequency of lift forces have been determined from the responses of the three lowermost segments to each test in which fluid kinematics flow in-line with the x axis. Values of maximum lift force amplitude, defined as the maximum positive force value measured transverse to the direction of fluid flow during a test, as well as average lift force period, defined as the average period of transverse force oscillations calculated by zero-crossing analysis, are presented in Table 5.5 along with Keulegan-Carpenter number for the flow conditions at each segment. Lift coefficients for each segment are formulated for each test from the maximum lift force amplitude, F_L , the segment length, l , the cylinder diameter, D , and the square of the maximum positive velocity, U^2 , as predicted by linear wave theory, according to:

$$C_L = \frac{F_L}{\rho l D U^2} \quad 5.7$$

The relative frequency of vortex shedding is computed according to:

$$f_r = \frac{T_w}{T_{F_L}} \quad 5.8$$

where T_w represents the period of oscillatory flow and T_{F_L} represents the average period of lift force oscillations. The lift coefficients and relative frequencies of vortex shedding computed from this data are plotted against KC in Figures 5.8 and 5.9 respectively. The values of frequency parameter for this data range between $\beta = 10200$ to 17000. The lift coefficient and frequency ratio data are in general agreement with those published by other researchers. Also, these results are not strongly dependent on the crossing angle (or degree of short-crestedness) of the flow. Only data from the third segment has been included in the figures.

A series of five tests were run in which the phase relationship at the segmented column between the two component waves varied from being in phase (anti-node of the flow) to being 180° out of phase (node of the short-crested flow). Force time series from the x and y axes of segment 3 during these five tests are presented in Figure 5.10. Under a short-crested node, fluid kinematics act transverse to the direction of wave propagation (or in the y direction). The forces measured at the segmented column in response to this unusual flow condition are characterized in the y direction by harmonic oscillations at the wave frequency resulting from drag and inertial forces as predicted by the Morison equation and in the x direction by higher frequency lift force oscillations. In between the node and anti-node, where fluid particles travel in elliptical orbits on inclined planes, forces measured in both directions can exhibit the combined effects of lift, drag and inertial loading.

A model to predict the magnitude of lift force on each axis in such three dimensional flow conditions can be developed, by calculating separate Keulegan-Carpenter numbers in the x and y directions based on fluid particle velocities in the horizontal plane (orthogonal to the segmented column). According to linear theory, the maximum velocity in the x direction under a short-crested anti-node at a particular depth equals $U_{SC} = 2U_C \cos(\alpha/2)$ and in the y direction under a short-crested node is $V_{SC} = 2U_C \sin(\alpha/2)$ where U_C is the maximum in-line velocity of a component wave at the elevation in question given by

$$U_C = \frac{\pi H_C}{T} \frac{\cosh[k(z+d)]}{\sinh(kd)} \quad 5.9$$

with $H_C = H_{SC}/2$. Moving from anti-node to node within the wave field, relative phase between the component waves increases from 0° to 180°, the in-line velocity maximum falls from U_{SC} to zero and the transverse velocity maximum increases from zero to V_{SC} . The x and y velocity maxima defined above can be generalized to

$$U_{sc} = 2U_c \cos(\alpha/2) \cos(\Delta\phi/2) \quad 5.10$$

$$V_{sc} = 2U_c \sin(\alpha/2) \sin(\Delta\phi/2)$$

Keulegan-Carpenter numbers can now be formed in each direction at any location in the short-crested flow specified by $\Delta\phi$:

$$KC_x = \frac{U_{sc} T}{D} \quad KC_y = \frac{V_{sc} T}{D} \quad 5.11$$

Bi-directional lift force amplitude can be estimated by

$$F_{Lx} = \frac{1}{2} \rho LDC_{Lx} V_{sc}^2$$

$$F_{Ly} = \frac{1}{2} \rho LDC_{Ly} U_{sc}^2$$

5.12

with lift coefficients in each direction given by Figure 5.8.

5.2.5. Total Forces

The total force exerted on a structure or structural member is often of particular interest to designers. The total force exerted on the instrumented 1.5 m length of the segmented column is easily obtained by adding up the forces measured by each segment. Also of interest is the vertical force profile at times corresponding to total force maxima and minima obtained by first normalizing the force measured on each segment by the segment height and then plotting these heights as functions of midpoint elevation.

Both the measured temporal variation of total force and the measured vertical force profiles have been compared to the estimates of Morison's equation using constant global force coefficients of $C_d = 0.7$ and $C_m = 1.7$ for all 32 tests. Kinematics are calculated according to the linear short-crested theory presented in section 2.1.

Above the mean water level, constant kinematics equal to the mean water level values are assumed up to the instantaneous short-crested free surface at $z = d + H_{SC}/2$. As before, kinematics are integrated over each segment to account for partial submergence. A typical result from the procedure developed to execute this comparison is presented in Figure 5.11. (The flow conditions for this test are $H=0.477\text{m}$, $T=2.071\text{s}$, $\alpha=60^\circ$.) The top window contains a water surface elevation time series obtained from a probe adjacent to the segmented column and serves to indicate the phase relationship between the total force (both measured and predicted total force are plotted in the central window) and the kinematics of the flow. Note that the total force maxima occur just after the zero-upcrossings of the free surface and well before the wave crest, indicating that the total force is inertia dominated. In this example, the total force prediction is very nearly identical to the measured total in-line force, indicating that Morison's equation (used with long-crested force coefficients and simplistic linear kinematics) has effectively estimated the force exerted by this short-crested flow.

Results from other tests are not always this good! In the lower half of the figure are two force profile plots; to the left is the profile of maximum negative in-line force while on the right is the positive equivalent. The measured and predicted profiles presented in each of these plots do not compare as well as the total force time series depicted above. The visible irregularities in the measured force profile have been 'smoothed out' or averaged for the total force through the selection of mean C_d and C_m values.

Table 5.6 contains a complete listing of predicted and measured total in-line force maxima and minima. These numbers indicate the ability of the wave force model based on the Morison equation to approximate in-line short-crested wave forces under ideal conditions; that is, when 'global' force coefficients are available directly from laboratory data. Figure 5.12 depicts a comparison between the measured and predicted total positive in-line force maxima based on the data in Table 5.6. Maximum errors in the order of 20% are realized between the

Morison equation/linear theory short-crested force estimates and the forces measured in the basin.

In a few tests, particularly those involving steep waves, the maximum measured force profile deviated significantly from the maximum predicted force profile due to free surface effects not included in the predictive model. The results of test SB15 ($H=0.655\text{m}$, $T=2.209\text{s}$ and $\alpha=30^\circ$), shown in Figure 5.13, are a good example of this behavior. Unfortunately, a matched water surface elevation time series is not available for this test, but from the magnitude of the forces measured on the upper segments at the time of the total force maximum (refer to the measured positive x profile in the lower right corner of Figure 5.13) it is apparent that the measured total force maximum must be coincident with the passage of a wave crest. The profile of the predicted force maximum again displays the shape characteristic of a total force maximum dominated by inertial loading prior to the arrival of the wave crest at the column.

Total force time series have also been summed in the transverse direction. In tests with waves at longer periods, considerable total transverse forces have been recorded, which, when combined with the total in-line force, contribute significantly to the total force resultant experienced by the column. Figure 4.9 depicts the in-line and transverse total force time series over one wave period as well as the magnitude and direction of the total force resultant for test SC17 ($H=0.679\text{m}$, $T=2.755\text{s}$ and $\alpha=30^\circ$). The indicated direction of force resultant is measured counter-clockwise positive from the x axis so that when both x and y forces are positive, the resultant direction is greater than zero.

It is significant to note that total lift forces half as large as the in-line force maxima were measured, leading to a maximum force resultant magnitude of 110 N compared to 98 N in the x direction. In all tests with large lift forces, the lift force maxima are nearly concurrent with the in-line force maxima, thus, resultant force maxima

are generally increased. Unfortunately, failure of 2 y direction load cells midway through the test program prevented the measurement and analysis of complete transverse force information.

5.3 COMPARISON BETWEEN TESTS

5.3.1 Repeatability

A set of 6 tests were conducted using the same driving signal to determine the combined repeatability of the wave generation system, the hydrodynamic loading phenomenon and the measurement systems. Results from these tests are presented in Table 5.7. Inspection of the measured force time series from any test indicate that the most variable measured quantity is the transverse force. This is not entirely unexpected because the vortex shedding phenomenon responsible for lift forces is, in itself, an unstable process. Lift forces often quickly build up and dissipate within a twenty second sample interval. In-line forces measured on upper segments can also be somewhat variable with time due to unstable free surface effects such as wave runup. In general, wave characteristics are very consistent throughout the sample interval.

5.3.2 Influence of Crossing Angle

In the present work, the influence of short-crestedness, characterized by the crossing angle between the two components comprising the flow, is of particular interest. A simple model describing the reduction in maximum in-line force at anti-nodes of the flow with increased crossing angle is proposed assuming that forces are adequately represented by the Morison equation and kinematics can be approximated by linear wave theory. The maximum force per unit length on the pile is given as the combination of drag and inertia forces by equation 2.3. Linear theory indicates that short-crested in-line kinematics are reduced with increasing crossing angle according to

$$u_{sc} = u_{lc} \cos(\alpha/2)$$

5.13

$$\dot{u}_{sc} = \dot{u}_{lc} \cos(\alpha/2)$$

Substitution of these expressions in equation 2.3 results in

$$F_{sc} = F_{lc} \frac{1}{2} [a \cos^2(\alpha/2) + b \cos(\alpha/2)] \quad 5.14$$

where $a+b = 2$. The ratio of a/b may be given by $a/b \approx KC/12.5$ with $KC = U_{sc}T/D$. This expression predicts how short-crestedness may reduce the force experienced by a pile as a function of crossing angle and the degree to which the force is dominated by drag and inertial effects (controlled by the relative magnitudes of a and b). The Keulegan-Carpenter parameter serves as an adequate measure of the relative importance of these forces. In inertia dominated flow, ($KC < 12.5$) the maximum in-line force experienced by a pile in short-crested waves will be $F_{sc} \approx F_{lc} \cos(\alpha/2)$ whereas in drag dominated flow ($KC > 12.5$), $F_{sc} \approx F_{lc} \cos^2(\alpha/2)$.

Results depicting maximum total in-line dimensionless force versus crossing angle are presented in Figure 5.14 in which the period of flow is printed next to each data point. Considerable scatter is evident between data at each crossing angle, but this is to be expected since the force is theoretically dependent on many parameters (equation 5.2) which have not all been held constant. Two significant trends are evident.

- (1) The total force decreases with crossing angle.
- (2) At larger crossing angles, the forces in high period flows are reduced more than those in low period flows.

These two observations concur with the simple theory outlined above, however, the proposed trend of force decay with crossing angle

cannot be verified by the present data. Those forces measured at $\alpha = 90^\circ$ are not reduced to the extent predicted by the theory. In all likelihood, significant higher order effects act to moderate the short-crested force reduction.

Data from segments 1 and 2 only are presented in a similar fashion in Figure 5.15. This data suggests that a linear decay of maximum in-line force with crossing angle equal to roughly 2.5% for every 10° could represent the phenomenon, as measured, reasonably well.

5.3.3 Influence of Location

The effect of location within the flow, characterized by the relative phase between the two wave components at the segmented column, on the maximum total in-line force can be discerned from inspection of Figure 5.16. In this case, the maximum total in-line force decreases dramatically with relative phase due to reductions in the magnitude of in-line kinematics and the fact that these reduced kinematics act over a smaller portion of the column. At $\Delta\phi = 180$ degrees, where in-line kinematics approach zero, the in-line force indicated in Figure 5.16 is entirely due to lift forces.

Figure 5.17 contains a similar plot depicting data from both the y and x axes of segments 1 and 2 only for the same test. As x direction forces decrease, y direction forces increase, reflecting the change in orientation of water particle orbits with relative phase. The y force maxima occur at $\Delta\phi = 180^\circ$ but remain less than the x force maxima recorded when $\Delta\phi = 0^\circ$ as expected given the 60 degree total crossing angle of this short-crested flow. The segmental in-line forces follow the same trend with $\Delta\phi$ as the total in-line forces, including the presence of lift force at $\Delta\phi = 180^\circ$, however, the rate of decay between $\Delta\phi = 0^\circ$ and $\Delta\phi = 90^\circ$ is less extreme. This reflects the fact that only reductions in kinematics play a role; since the portion over which viscous and inertial forces act remains constant equal to the segment

length. Note that lift forces are recorded in the x direction of segment 2 at $\Delta\phi = 0^\circ$ but not on segment 1.

Prediction of this decay in submerged segment force maxima with relative phase can be developed analogous to the theory presented in section 5.3.2 concerning the variation in force with crossing angle. The x and y components of kinematics vary with relative phase according to:

$$\begin{aligned} U(\Delta\phi) &= U(0) \left(\frac{1 + \cos(\Delta\phi)}{2} \right) \\ V(\Delta\phi) &= V(180) \left(\frac{1 - \cos(\Delta\phi)}{2} \right) \end{aligned} \quad 5.15$$

with:

$$\begin{aligned} U(0) &= 2U_C \cos(\alpha/2) \\ V(180) &= 2U_C \sin(\alpha/2) \end{aligned} \quad 5.16$$

where U_C equals the maximum fluid velocity of each long-crested component wave. As before, substitution of these expressions for kinematics into Morison's equation leads to

$$\begin{aligned} F_x(\Delta\phi) &= F_x(0) \frac{1}{2} \left(a \left[\frac{1 + \cos(\Delta\phi)}{2} \right]^2 + b \left[\frac{1 + \cos(\Delta\phi)}{2} \right] \right) \\ F_y(\Delta\phi) &= F_y(180) \frac{1}{2} \left(a \left[\frac{1 - \cos(\Delta\phi)}{2} \right]^2 + b \left[\frac{1 - \cos(\Delta\phi)}{2} \right] \right) \end{aligned} \quad 5.17$$

where $a+b = 2$ and $a/b = KC/12.5$ with $KC_x = U_x(\Delta\phi)T/D$ and $KC_y = V(\Delta\phi)T/D$.

Although tests were not conducted involving different relative phases at crossing angles other than $\alpha = 60^\circ$, some postulations can be made from consideration of the process and inspection of the results presented in Figures 5.18 and 5.19. Transverse forces could be greater than in-line forces in short-crested flows at crossing angles greater than 90° . In this case, the largest transverse force will occur at the node of the short-crested flow. For flows with $\alpha < 90^\circ$, the largest

forces will occur at short-crested anti-nodes and will act in the direction of wave propagation. Although in-line and transverse forces at locations between these two extremes (ie. $0 > \Delta\phi < 180$) are considerable, their resultant remains less than the force maximum experienced at either $\Delta\phi = 0^\circ$ or 180° .

5.3.4 Importance of Lift Forces

Segmental lift force maxima greater than half the in-line force maxima were recorded in several tests. Plotted in Figure 5.18 are the ratios of transverse to in-line force maxima measured on segment 2 versus wave period for 8 long-crested and 15 unique in-phase short-crested flow conditions. The crossing angle of the flow is included adjacent to each data point. Up to a period of 2 seconds, lift forces hover below 20% of the in-line force, but above this, they increase with increasing period to greater than 50% of the in-line force at $T = 2.8$ seconds. Wave periods near 2 seconds correspond to Keulegan-Carpenter numbers approximately equal to 6.5 for flow conditions at the third segment. With reference to Figure 5.9 it is apparent that the lift force frequency ratio, f_R , is less than 2 for $KC < 6.5$ and equal to 2 for all $KC > 6.5$. This indicates that (for segment three) harmonic asymmetry in the shedding of vortices leading to substantial lift forces becomes developed only at wave periods above roughly 2 seconds. Below this limit, partial vortex shedding gives rise to smaller lift forces. Also significant is the result that crossing angle (ie short-crestedness) has no obvious influence on this phenomenon.

6.0 CONCLUSIONS AND RECOMMENDATIONS

6.1 CONCLUSIONS

Regular short-crested waves generated through the superposition of two long-crested waves crossing at various angles have been studied. In particular, the hydrodynamic forces exerted by these waves on a rigid surface piercing cylinder have been determined through a series of laboratory tests.

The cylinder is partitioned into nine independent sensing segments of varying length which each measure two perpendicular components of wave force. Segmental forces enable the vertical profile of wave force to be examined while the responses of each segment are easily summed to yield the total in-line and transverse force experienced by the column.

Only non-breaking waves have been considered. Short-crested waves ranging in steepness from 0.061 to 0.118 have been generated through the interaction of regular long-crested components crossing at angles of 30 60 and 90 degrees. These flow conditions resulted in Keulegan-Carpenter numbers at the mean water level between 4 and 14.

Force coefficients have been determined from the data collected on both submerged and partially exposed segments during tests with eight different long-crested waves by means of least squares analysis. Non-linear wave theory has been used to evaluate the kinematics at each segment in these long-crested flows. Good agreement is achieved between current estimates of C_d and C_m and those previously published by other researchers. Data from lower segments are found to be best suited to the estimation of inertia coefficient while data from upper segments are well conditioned for the resolution of drag coefficient. This observation reinforces the conclusion that inertia forces are dominant on lower segments while drag forces become increasingly more important higher up the column.

The force coefficients discerned from data collected in long-crested waves have been found to be directly applicable to short-crested waves with similar characteristics (ie period, height). The Morison equation model is found to be an adequate predictor of in-line short-crested wave forces when used with appropriate 'global' force coefficients and linear short-crested kinematics. The success of a pair of constant force coefficients applied to the entire column over a range of flow conditions is significant, particularly in light of the fact that local C_d and C_m values were found to be highly variable. Linear kinematics have been successfully extrapolated above the mean water level by assuming mean water level values to apply within the crest of the short-crested wave.

The Morison equation force model is not a good predictor of total maximum wave force in situations where free surface effects are large. Some evidence exists to indicate that free surface effects such as runup and wave impact loading are more likely to dominate the forces exerted by short-crested waves because they rise higher and steeper before breaking and travel faster than do their long-crested counterparts. Since these effects can lead to total force maxima an order of magnitude greater than predicted by the Morison equation, a designer must ensure that they will not occur before ignoring them in analysis.

Both segmental and total lift forces equal to half the in-line force have been measured in both long-crested and short-crested waves. These large forces acting transverse to the direction of fluid flow are concurrent with in-line force maxima and effect an increase in total force greater than ten percent above the in-line maximum. The largest lift forces occur in flow conditions where the Keulegan-Carpenter number is close to 12, confirming the findings of previous researchers that the lift coefficient reaches a maximum in this range of KC. The frequency of lift force oscillations measured in both long- and short-

crested flows becomes established at twice the wave frequency above $KC = 6$.

Simple theoretically based expressions are proposed to describe the influence of crossing angle and location within the short-crested wave field on the maximum total in-line force experienced by a column. The form of these expressions is confirmed by the test results obtained by this study. The maximum force is found to decrease with increasing crossing angle. A rule of thumb would give the force reduction as roughly 2.5 percent of the long-crested force maximum for every 10 degrees of total crossing angle.

Force maxima have been found to be largest at the anti-node of a short-crested flow and aligned in the direction of wave propagation. Surprisingly large forces transverse to the direction of wave propagation are exerted on a pile located at the node of a short-crested flow, particularly when one is used to associating large wave force with large wave heights. These transversely directed forces are the result of fluid kinematics perpendicular to the direction of wave propagation.

Some specific conclusions concerning experiment methodology have emerged from this work:

- Short-crested waves can be effectively created through the superposition of two long-crested components. A segmented wave machine can be programed to generate such waves through partitioning of the machine into two halves. Wave generation in short bursts is desireable when regular waves oblique to the machine are required.
- Reliable current measurement is extremely difficult in the laboratory when using electromagnetic current meters.
- A linear array of probes in the direction of wave propagation is useful to study the evolution of wave form over distance.

- The segmented column is a useful research tool with characteristics suitable for the measurement of dynamic wave loading.

6.2 RECOMMENDATIONS FOR FURTHER STUDY

The segmented column is a valuable research tool which can be used to study details of hydrodynamic loading, such as vertical force distribution, local contact pressures and transverse forces, in almost any flow condition. Coupled with the superior wave generation capabilities of the Offshore Wave Basin, the forces exerted by regular and random short- and long-crested seas as well as breaking wave transients, both with and without the presence of currents, can be studied.

The nonlinear free surface effects associated with breaking waves are of particular interest to the designers of coastal and offshore structures since they have been found to exert forces an order of magnitude above those predicted by the Morison equation. The segmented column is well suited to the study of these dynamic impact events because of the stiff characteristics of its force sensing transducers. It is recommended that long-crested, short-crested and episodic breaking wave forces on the segmented column be examined.

Another domain of concern on the forefront of research is the influence of structure compliancy on hydrodynamic loading. The segmented column could be easily modified to investigate this issue through model tests by fabricating a support structure with the desired bending stiffness. A ball and socket joint at the base with restraint provided through springs of known stiffness attached to the top of the column would serve well.

These two recommendations for further study are just the tip of the iceberg when the myriad of useful potential studies are considered. However, they are believed to be the most significant since they would probe topics of considerable interest to industry at this time.

BIBLIOGRAPHY

1. Chakrabarti, S. K. (1980), "Inline Forces on Fixed Vertical Cylinder in Waves", *J. Waterway, Port, Coastal and Ocean Engineering ASCE*, Vol 106, No. 3, pp. 145-155.
2. Chan, E. S., and Melville, W. K. (1987), "Plunging Wave Forces on Surface Piercing Structures", *Proc. 6th, Offshore Mechanics and Arctic Engineering Symp.*, Houston, Vol. 2, pp. 61-72.
3. Chappellear, J. E. (1961), "On the Description of Short-Crested Waves", *Beach Erosion Board. T. M.*, Vol. 125, pp. 1-26.
4. Cointe, R. (1987), "Two Dimensional Water-Solid Impact", *Proc. 6th Offshore Mechanics and Arctic Engineering Symp.*, Houston, Vol. 2, pp. 97-104.
5. Cotter, D. C., and Chakrabarti, S. K. (1984), "Wave Force Tests on Vertical and Inclined Cylinders", *J. Waterway, Port, Coastal and Ocean Engineering ASCE*, Vol. 110, pp. 1-14.
6. Danel, P. (1952), "On the Limiting Clapotis", *Gravity Waves, US. Nat. Bureau of Standards, Circular 521*, pp. 35-38.
7. Dean, R. G. (1968), "Breaking Wave Criteria: A Study Employing A Numerical Wave Theory", *Proc. 11th. Coastal Engineering Conference*, pp. 108-123.
8. Dean, R. G., Dalrymple, R. A., and Hudspeth, R. T. (1981), "Force Coefficients from Wave Project 1 and 2 Data Including Free Surface Effects", *Journal Society of Petroleum Engineers*, pp. 779-786.
9. Dean, R. G., Tørum, A., and Kjeldsen, S. P. (1985), "Wave Forces on a Pile in the Surface Zone from the Wave Crest to the Wave Trough", *Proc. International Symposium on Separated Flow Around Marine Structures, Trondheim*, pp. 75-89.
10. Dummer, J., Hudspeth, R., and Nath, J. (1986), "High Reynolds Number Wave Force Investigation in a Wave Flume", *Proc. 5th Offshore Mechanics and Arctic Engineering Symp.*, Tokyo, Vol. 1, pp. 113-122.
11. Fenton, J. D. (1985), "Wave Forces On Vertical Walls", *J. Waterway, Port, Coastal and Ocean Engineering, ASCE*, Vol. 111, No. 4., pp. 693-718.
12. Fougere, G., Crookshank, N. L., and Pelletier, D. (1984), "NRC Hydraulics Laboratory General Plotting Package User Guide", *NRCC Division of Mechanical Engineering Report LM-HY-001*.

13. Fuchs, R. A. (1951), "On the Theory of Short-Crested Oscillatory Waves", *Gravity Waves*, U.S. Nat. Bureau of Standards, Circular 521, pp. 187-200.
14. Funke, E. R., and Mansard, E. P. D. (1984), "The NRCC 'Random' Wave Generation Package", NRCC Division of Mechanical Engineering Report TR-HY-002.
15. Halliwell, A. R., and Machen, P. C. (1981), "Short-Crested Breaking Waves in Water of Limited Depth", *Proc. Instn. Civ. Engrs., Part 2*, No. 71, pp. 663-674.
16. Hsu, J. R. C. (1977), "Kinematics of Short-Crested Water Waves", *Proc. 6th Australasian Hydraulics and Fluid Mechanics Conference*, Adelaide, pp. 56-59.
17. Hsu, J. R. C., Tsuchiya, Y., and Silvester, R. (1979), "Third Order Approximation to Short-Crested Waves", *Journal of Fluid Mechanics*, Vol. 90, pp. 179-196.
18. Hsu, J. R. C., Silvester, R., and Tsuchiya, Y. (1980), "Boundary-Layer Velocities and Mass Transport in Short-Crested Waves", *Journal of Fluid Mechanics*, Vol. 99, pp. 321-342.
19. Hsu, J. R. C., (1983), "On the Limiting Conditions for Short-Crested Waves", *Proc. Xth Australasian Conf. on Coastal and Ocean Engineering*, Gold Coast, pp. 42-46.
20. Isaacson, M. (1984), "Theoretical Analysis of Directional Sea State Synthesis", *Seaconsult Marine Research Ltd. Report*, DSS File No. 07SQ.31945-4-0014.
21. Iwagaki, Y., and Toshiyuki, A. (1984), "Hydrodynamic Forces on a Circular Cylinder due to Combined Wave and Current Loading", *Proc. 19th. Coastal Engineering Conference*, Houston, Vol. 3, pp. 2857-2874.
22. Jamieson, W. W., and Mansard, E. P. D. (1987), "An Efficient Upright Wave Absorber", *Proc. ASCE Specialty Conference on Coastal Hydrodynamics*, Newark, Delaware.
23. Kjeldsen, S. P. (1982), "2- and 3-Dimensional Deterministic Freak Waves", *Proc. 18th. Coastal Engineering Conference*, Vol. 1, pp. 677-694.
24. Kjeldsen, S. P., and Akre (1985), "Wave Forces on Vertical Piles Near the Free Surface Caused by 2-Dimensional and 3-Dimensional Breaking Waves", *NTNF Research Project Report No. 1.10*.
25. Kjeldsen, S. P., Tørum, A., and Dean, R. G. (1986), "Wave Forces on Vertical Piles caused by 2- and 3-Dimensional Breaking Waves",

- Proc. 20th. International Conference on Coastal Engineering, Taipei.
26. Kjeldsen, S. P., and Myrhaug, D. (1979), "Breaking Waves in Deep Water and Resulting Wave Forces", Proc. 11th. Offshore Technology Conference, Houston, Paper No. OTC 3646.
 27. Le Mehaute, B. (1986), "On the Highest Periodic Short-Crested Wave", J. of Waterway, Port, Coastal and Ocean Engineering, Vol 112, No. 2., pp. 320-330.
 28. Machen, P. C. (1984), "Short-Crested Breaking Waves", Proc. 19th. Coastal Engineering Conference, Vol. 1, pp. 912-928.
 29. Miche, R., (1944), "Mouvements Ondulatoires des Mers en Profondeur Constante et Decroissante", Annales des Pontes et Chaussées, pp. 27-78, 131-164, 270-282, 369-406.
 30. Miles, J. W. (1977), "Obliquely Interacting Solitary Waves", Journal of Fluid Mechanics, Vol. 79, pp. 157-169.
 31. Miles, M. D., Laurich, P. H., and Funke, E. R. (1986), "A Multi Mode Segmented Wave Generator for the NRC Hydraulics Laboratory", Proc. 21st American Towing Tank Conference, Washington, D.C., USA.
 32. Mogridge, G. R. (1985), "Hydrodynamic Model Tests of the Semi-Submersible 'Ocean Ranger'", NRCC Hydraulics Laboratory Technical Report TR-HY-0007.
 33. Newman, J. N. (1977), "Marine Hydrodynamics", The MIT Press, Cambridge Mass., pp. 39-42.
 34. Penny, W. G., and Price, A. T. (1952), "Finite Periodic Stationary Gravity Waves in a Perfect Liquid", Phil. Trans. Roy. Soc., Ser. A, No. 242, 882, pp. 254-284.
 35. Reinecker, M. M., and Fenton, J. D. (1981), "A Fourier Approximation for Steady Water Waves", Journal Fluid Mechanics, Vol. 104, pp. 119-137.
 36. Rodenbusch, G., and Forristall, G. Z. (1986), "An Empirical Model for Random Directional Wave Kinematics Near the Free Surface", Proc. Offshore Technology Conference, Houston, Paper No. OTC 5097, pp. 137-146.
 37. Roberts, A. J. (1983), "Highly Nonlinear Short-Crested Water Waves", Journal of Fluid Mechanics, Vol. 135, pp. 301-321.
 38. Sarpkaya, T., and Isaacson, M. (1981), "Mechanics of Wave Forces on Offshore Structures", Van Nostrand Reinhold, New York.

39. Sawaragi, T., and Nochino, M. (1984), "Impact Forces of Nearly Breaking Waves on a Vertical Circular Cylinder", *Coastal Engineering in Japan*, Vol. 27, pp. 249-263.
40. Sparboom, U., Efthimiou, N., and Voigt, A. (1984), "Full Scale Wave Forces on Piles in Shallow Water", *Proc. 19th. Coastal Engineering Conference*, Vol. 3, pp. 2892-2908.
41. Stansby, P. K., Bullock, G. N., and Short, I. (1983), "Quasi-2-D Forces on a Vertical Cylinder in Waves", *J. Waterways, Port, Coastal and Ocean Engineering ASCE*, No. 1, Vol. 109, pp. 128-132.
42. Stokes, G. G. (1847), "On the Theory of Oscillatory Waves", *Trans. Camb. Phil. Soc.*, Vol. 8, pp 441-455.
43. Stokes, G. G. (1880), "Math Phys. Papers", Vol. 1, *Camb. Univ. Press*.
44. Watanabe, A., Hara, T., and Horikawa, K. (1984), "Study on Breaking Condition for Compound Wave Trains", *Coastal Engineering in Japan*, Vol. 27, pp. 71-82.
45. Wiegel, R. L. (1964), "Oceanographical Engineering", *Prentice-Hall, Englewood Cliffs, N.J.*
47. Yamada, H. (1957) "On the Highest solitary Wave" *Rep. Res. Inst. of Appl. Mech., Kyushu Univ.*, Vol. 5, pp. 53-67.

APPENDIX A

DYNAMIC RESPONSE OF THE SEGMENTED COLUMN

Assembly and calibration of the segmented column was a delicate and time consuming task. On two separate occasions, failure of a 73N load cell during calibration necessitated partial disassembly of the column, replacement of the faulty transducer, followed by re-calibration of each segment. These failures served to foreshadow two other breakdowns which occurred during the active testing phase of the study.

Each force transducer can be schematically represented as a single degree of freedom spring-mass-dashpot system. The equation of motion for such a system is given by:

$$F(t) = m_t \ddot{s}(t) + c_t \dot{s}(t) + k_t s(t) \quad A.1$$

where $s(t)$ is the time dependent horizontal displacement of the lumped mass and \dot{s} and \ddot{s} are its velocity and displacement respectively. $F(t)$ is the exciting force and k_t , c_t and m_t are the stiffness, damping and mass respectively of the transducer. The natural frequency of free vibrations for this system (with no exciting force) is given by:

$$f_N = \frac{1}{2\pi} \left(\frac{k_t}{m_t} \right) \quad A.2$$

The rate at which damping reduces the amplitude of vibrations for an under-damped system is proportional to the damping ratio, ζ , equal to:

$$\zeta = \frac{c_t}{2(m_t k_t)} \quad A.3$$

An ideal force transducer has a very high natural frequency, combined with a high damping ratio so that free vibrations do not corrupt the physical process under measurement.

The measured free vibration response of each transducer varies throughout the column, reflecting the difference in the mass of the external shell between segments. The larger size of the lower segments (refer to Figure 3.4) require that their shells contain more mass, therefore, as predicted by equations A.2 and A.3, free vibrations occur at lower natural frequencies and take a bit longer to dissipate.

The shell of each segment is potentially able to vibrate in 6 degrees of freedom. Even though each shell is instrumented to directly sense only translational vibrations in the x and y directions, energy transfer through non-linear coupling between all six vibrational modes can give rise to a system of oscillations that is very complex.

The degree of coupling between axes within a segment and between adjacent segments was determined from the response to initial condition tests. Figure A.1 contains a set of responses from one test in which loading was abruptly removed from the x axis of the fourth segment. The top two time series in the figure depict the response from the y and x axes of the adjacent third segment. Each response is shown at a different scale so that vibration details can be observed. A sudden 17N reduction in loading on the x axis of segment 4 results in some coupled free vibration and a very small 0.1N permanent offset in the y direction. Some free vibrations are also transferred to both axes of segment 3, more so to the x direction than to the y, however, no permanent offset is registered. Thus, high frequency free vibrations are transferred between segments but external forces are not.

Also of interest is the response to dynamic loading obliquely to both the x and y axes. Figure A.2 contains a set of responses, similar to those in Figure A.1, obtained from an initial condition test in which segment 4 was loaded between each axis. The response in the x and y transducers is virtually identical. Again, vibrations are registered in segment three but the change in external loading has not been transferred. There is some evidence of beating in the free vibration responses depicted in Figure A.2, suggesting that the shells

of both segments have been excited in additional modes of vibration which are contributing to the forces measured in the x and y direction through non-linear coupling.

Rotational vibration around the longitudinal axis was found to be the most significant undesirable mode for all segments because of the low frequency and potentially large amplitude of oscillations. Fortunately, this mode of vibration only reached unacceptable levels when loading was applied with a component tangential to the surface of the segment. No significant hydrodynamic loading acts in this manner.

During static and dynamic calibration of each transducer, a rigid lightweight aluminum frame was used to suspend a known mass, ensuring single point loading normal to the surface of the segment. The response of a transducer was not affected by the elevation along the segment at which the load was applied. As expected, loading at 45 degrees to both axes yielded response in both transducers equal to $\cos(45)$ or 0.707 times the total load; thus proving the segment capable of accurately resolving an oblique loading into two orthogonal components.

APPENDIX B**DETAILS CONCERNING WAVE SYNTHESIS**

Program RODSD (Regular Oblique Driving Signal Definition) accepts as input the height, period, and propagation direction of the desired wave as well as parameters defining the portion of the wave machine to participate in its generation. Output is a file containing an array defining the amplitude, frequency, and phase of the sinusoidal motions for each paddle in the wave machine. Computation of the amplitude of board motion required to generate a particular wave height is based on the transfer function theory introduced in section 2.3 as reviewed by Isaacson (1984). One definition file is created for each long-crested wave to be generated.

Program DSGEN (Driving Signal GENERation) is designed to accept as input a number of definition files output from RODSD. Driving signals for each segment of the wave machine are formulated by superimposing the amplitude, frequency, phase and partitioning information from all definition files. Other input parameters control the relative phase of each long-crested component wave. Thus, a set of driving signals can be generated which, when run in the basin, produce several oblique long-crested waves that interact with any predetermined phase at a particular location. RODSD and DSGEN can also be used to generate the driving signals required for long-crested waves parallel to the wave machine by setting the propagation direction for a component wave to zero.

The wave synthesis software developed for this project incorporated other features designed to improve the quality of the waves generated in the basin. One such innovation was the calculation of a unique start-up time for each segment in a particular partition. Programs RODSD and DSGEN lag the start-up time of each successive segment along the wave machine in the direction of propagation according to

$$\Delta t_i = \frac{iB}{C_g} \cos(90 - \alpha/2) \quad ; \quad i = 1, 2, \dots, N \quad B.1$$

where

$$C_g = \frac{1}{2} \left(1 + \frac{2kd}{\sinh(2kd)} \right) \quad B.2$$

represents the group velocity of the wave. At the start-up of every test different segments 'kick in' at different times so that one continuous leading wave is created.

Table 4.1: Phase 2 Wave Characteristics Data

| TEST | H (m) | T (s) | H/L | L (m) | ALPHA | PHASE | d/g*T*T |
|------|-------|-------|-------|--------|-------|-------|---------|
| SN11 | 0.393 | 1.693 | 0.088 | 4.466 | 0 | 0 | 0.071 |
| SN22 | 0.479 | 1.850 | 0.091 | 5.264 | 0 | 0 | 0.060 |
| SN33 | 0.581 | 2.048 | 0.092 | 6.315 | 0 | 0 | 0.049 |
| SN44 | 0.684 | 2.253 | 0.092 | 7.435 | 0 | 0 | 0.040 |
| SN31 | 0.397 | 2.039 | 0.063 | 6.302 | 0 | 0 | 0.049 |
| SU42 | 0.479 | 2.250 | 0.065 | 7.369 | 0 | 0 | 0.040 |
| SN53 | 0.572 | 2.504 | 0.065 | 8.800 | 0 | 0 | 0.033 |
| SN64 | 0.654 | 2.829 | 0.063 | 10.381 | 0 | 0 | 0.025 |
| SB11 | 0.463 | 1.819 | 0.086 | 5.384 | 30 | 0 | 0.062 |
| SC12 | 0.655 | 1.823 | 0.118 | 5.551 | 30 | 0 | 0.061 |
| SB14 | 0.460 | 2.207 | 0.056 | 8.214 | 30 | 0 | 0.042 |
| SB15 | 0.655 | 2.209 | 0.079 | 8.291 | 30 | 0 | 0.042 |
| SC17 | 0.679 | 2.755 | 0.061 | 11.131 | 30 | 0 | 0.027 |
| SB31 | 0.485 | 1.717 | 0.083 | 5.843 | 60 | 0 | 0.069 |
| SB32 | 0.672 | 1.717 | 0.112 | 6.000 | 60 | 0 | 0.069 |
| SC34 | 0.477 | 2.071 | 0.062 | 7.694 | 60 | 0 | 0.048 |
| SC35 | 0.657 | 2.071 | 0.086 | 7.640 | 60 | 0 | 0.048 |
| SB37 | 0.680 | 2.561 | 0.064 | 10.625 | 60 | 0 | 0.031 |
| SC41 | 0.498 | 1.550 | 0.087 | 5.724 | 90 | 0 | 0.085 |
| SC42 | 0.657 | 1.549 | 0.115 | 5.713 | 90 | 0 | 0.085 |
| SC44 | 0.493 | 1.850 | 0.066 | 7.470 | 90 | 0 | 0.060 |
| SC45 | 0.674 | 1.851 | 0.090 | 7.489 | 90 | 0 | 0.060 |
| SC47 | 0.690 | 2.249 | 0.069 | 10.000 | 90 | 0 | 0.040 |
| SRE4 | 0.675 | 2.072 | 0.088 | 7.670 | 60 | 0 | 0.048 |
| SRE3 | 0.676 | 2.071 | 0.086 | 7.860 | 60 | 0 | 0.048 |
| SRE2 | 0.673 | 2.072 | 0.087 | 7.736 | 60 | 0 | 0.048 |
| SRE1 | 0.684 | 2.073 | 0.088 | 7.773 | 60 | 0 | 0.047 |
| SCP1 | 0.675 | 2.072 | 0.088 | 7.670 | 60 | 0 | 0.048 |
| SCP2 | 0.675 | 2.072 | 0.088 | 7.670 | 60 | 45 | 0.048 |
| SCP3 | 0.675 | 2.072 | 0.088 | 7.670 | 60 | 90 | 0.048 |
| SCP4 | 0.675 | 2.072 | 0.088 | 7.670 | 60 | 135 | 0.048 |
| SCP5 | 0.675 | 2.072 | 0.088 | 7.670 | 60 | 180 | 0.048 |

Table 5.1: Crossing Wave Superposition Characteristics Data

| TEST | ALPHA COMPONENT | T (s) | H (m) | SAVE | CFSAVE | Hc+Hc/Hsc |
|------|-----------------|-------|-------|-------|--------|-----------|
| ML11 | 30 LEFT | 1.818 | 0.249 | 0.049 | 0.101 | |
| MR11 | 30 RIGHT | 1.819 | 0.250 | 0.049 | 0.100 | |
| MB11 | 30 BOTH | 1.819 | 0.463 | 0.086 | 0.216 | 1.078 |
| ML12 | 30 LEFT | 1.817 | 0.339 | 0.067 | 0.140 | |
| MR12 | 30 RIGHT | 1.819 | 0.351 | 0.069 | 0.146 | |
| MB12 | 30 BOTH | 1.822 | 0.567 | 0.103 | 0.223 | 1.217 |
| ML14 | 30 LEFT | 2.209 | 0.238 | 0.033 | 0.073 | |
| MR14 | 30 RIGHT | 2.209 | 0.234 | 0.033 | 0.070 | |
| MB14 | 30 BOTH | 2.207 | 0.460 | 0.056 | 0.123 | 1.026 |
| ML15 | 30 LEFT | 2.208 | 0.340 | 0.048 | 0.098 | |
| MR15 | 30 RIGHT | 2.208 | 0.334 | 0.047 | 0.095 | |
| MB15 | 30 BOTH | 2.209 | 0.655 | 0.079 | 0.193 | 1.029 |
| ML17 | 30 LEFT | 2.754 | 0.386 | 0.038 | 0.089 | |
| MR17 | 30 RIGHT | 2.754 | 0.375 | 0.037 | 0.086 | |
| MB17 | 30 BOTH | 2.761 | 0.714 | 0.061 | 0.177 | 1.066 |
| ML31 | 60 LEFT | 1.716 | 0.254 | 0.056 | 0.124 | |
| MR31 | 60 RIGHT | 1.717 | 0.244 | 0.053 | 0.115 | |
| MB31 | 60 BOTH | 1.717 | 0.485 | 0.083 | 0.203 | 1.027 |
| ML32 | 60 LEFT | 1.715 | 0.352 | 0.077 | 0.193 | |
| MR32 | 60 RIGHT | 1.717 | 0.346 | 0.076 | 0.191 | |
| MB32 | 60 BOTH | 1.717 | 0.672 | 0.112 | 0.280 | 1.039 |
| ML34 | 60 LEFT | 2.071 | 0.205 | 0.032 | 0.074 | |
| MR34 | 60 RIGHT | 2.068 | 0.207 | 0.032 | 0.074 | |
| MB34 | 60 BOTH | 2.071 | 0.420 | 0.055 | 0.128 | 0.981 |
| ML35 | 60 LEFT | 2.071 | 0.294 | 0.046 | 0.116 | |
| MR35 | 60 RIGHT | 2.069 | 0.284 | 0.044 | 0.115 | |
| MB35 | 60 BOTH | 2.070 | 0.584 | 0.077 | 0.182 | 0.990 |
| ML37 | 60 LEFT | 2.563 | 0.352 | 0.039 | 0.095 | |
| MR37 | 60 RIGHT | 2.563 | 0.346 | 0.038 | 0.094 | |
| MB37 | 60 BOTH | 2.561 | 0.680 | 0.064 | 0.158 | 1.026 |
| ML41 | 90 LEFT | 1.543 | 0.201 | 0.054 | 0.112 | |
| MR41 | 90 RIGHT | 1.545 | 0.195 | 0.052 | 0.107 | |
| MB41 | 90 BOTH | 1.544 | 0.390 | 0.087 | 0.127 | 1.015 |
| ML42 | 90 LEFT | 1.542 | 0.273 | 0.074 | 0.128 | |
| MR42 | 90 RIGHT | 1.546 | 0.268 | 0.072 | 0.132 | |
| MB42 | 90 BOTH | 1.548 | 0.519 | 0.085 | 0.180 | 1.042 |
| ML44 | 90 LEFT | 1.847 | 0.205 | 0.039 | 0.085 | |
| MR44 | 90 RIGHT | 1.847 | 0.204 | 0.039 | 0.084 | |
| MB44 | 90 BOTH | 1.845 | 0.424 | 0.055 | 0.138 | 0.965 |
| ML45 | 90 LEFT | 1.847 | 0.286 | 0.056 | 0.135 | |
| MR45 | 90 RIGHT | 1.847 | 0.286 | 0.055 | 0.134 | |
| MB45 | 90 BOTH | 1.847 | 0.562 | 0.073 | 0.138 | 1.018 |
| ML47 | 90 LEFT | 2.258 | 0.241 | 0.032 | 0.086 | |
| MR47 | 90 RIGHT | 2.252 | 0.208 | 0.028 | 0.077 | |
| MB47 | 90 BOTH | 2.260 | 0.455 | 0.046 | 0.127 | 0.987 |

Table 5.2: Measured and Predicted Velocities Under Long-Crested Waves

| TEST | T (s) | H (m) | ELEV (m) | Up-p (m/s) | | |
|------|-------|-------|----------|------------|--------|---------|
| | | | | MEASURED | LINEAR | NON-LIN |
| N11 | 1.69 | 0.393 | 1.08 | 0.360 | 0.417 | 0.422 |
| N11 | 1.69 | 0.393 | 1.68 | 0.717 | 0.937 | 0.896 |
| N22 | 1.85 | 0.479 | 1.08 | 0.539 | 0.586 | 0.588 |
| N22 | 1.85 | 0.479 | 1.68 | 0.930 | 1.138 | 1.080 |
| N33 | 2.05 | 0.581 | 1.08 | 0.770 | 0.810 | 0.793 |
| N33 | 2.05 | 0.581 | 1.68 | ???? | 1.366 | 1.278 |
| N44 | 2.25 | 0.684 | 1.08 | 0.769 | 1.048 | 1.000 |
| N44 | 2.25 | 0.684 | 1.68 | 1.105 | 1.591 | 1.457 |
| N31 | 2.04 | 0.397 | 1.08 | 0.581 | 0.551 | 0.548 |
| N31 | 2.04 | 0.397 | 1.68 | 0.912 | 0.933 | 0.906 |
| U42 | 2.25 | 0.479 | 1.08 | 0.640 | 0.734 | 0.721 |
| U42 | 2.25 | 0.479 | 1.68 | 0.932 | 1.112 | 1.070 |
| N53 | 2.5 | 0.572 | 1.08 | 0.710 | 0.952 | 0.918 |
| N53 | 2.5 | 0.572 | 1.68 | 0.928 | 1.317 | 1.247 |
| N64 | 2.83 | 0.654 | 1.08 | 0.959 | 1.167 | 1.105 |
| N64 | 2.83 | 0.654 | 1.68 | 1.143 | 1.491 | 1.390 |

Table 5.3: Force Coefficient Estimates from Predicted Kinematics in Long-Crested Waves.

| TEST | SEGMENT | KC(SEG) | Re/1000 | β /10000 | CD | CM |
|-------|---------|---------|---------|----------------|-------|------|
| SN112 | 1 | 2.077 | 35.45 | 1.71 | -0.71 | 1.17 |
| SN222 | 1 | 3.194 | 49.90 | 1.56 | 0.19 | 1.10 |
| SN312 | 1 | 3.306 | 46.86 | 1.42 | 0.06 | 1.24 |
| SU422 | 1 | 4.857 | 62.39 | 1.28 | 0.19 | 0.98 |
| SN332 | 1 | 4.884 | 68.92 | 1.41 | -0.15 | 1.12 |
| SN442 | 1 | 6.953 | 89.19 | 1.28 | 0.50 | 0.94 |
| SN532 | 1 | 7.006 | 80.86 | 1.15 | 0.17 | 0.85 |
| SN642 | 1 | 9.706 | 99.15 | 1.02 | 0.38 | 0.95 |
| SN112 | 2 | 3.311 | 56.52 | 1.71 | -0.54 | 1.24 |
| SN312 | 2 | 4.455 | 69.59 | 1.56 | 0.10 | 1.44 |
| SN222 | 2 | 4.662 | 66.08 | 1.42 | 0.20 | 1.23 |
| SU422 | 2 | 6.196 | 78.81 | 1.28 | 0.07 | 1.17 |
| SN332 | 2 | 6.559 | 92.56 | 1.41 | -0.10 | 1.32 |
| SN532 | 2 | 8.388 | 107.60 | 1.28 | 0.16 | 1.05 |
| SN442 | 2 | 8.778 | 101.31 | 1.15 | 0.40 | 1.05 |
| SN642 | 2 | 11.102 | 113.41 | 1.02 | 0.43 | 1.19 |
| SN112 | 3 | 4.675 | 79.80 | 1.71 | 0.50 | 2.32 |
| SN312 | 3 | 5.604 | 87.54 | 1.56 | 1.21 | 2.64 |
| SN222 | 3 | 6.197 | 87.83 | 1.42 | 1.17 | 2.18 |
| SU422 | 3 | 7.377 | 94.75 | 1.28 | 1.07 | 2.17 |
| SN332 | 3 | 8.234 | 116.19 | 1.41 | 0.54 | 2.33 |
| SN532 | 3 | 9.696 | 124.37 | 1.28 | 0.81 | 1.90 |
| SN442 | 3 | 10.547 | 121.73 | 1.15 | 1.05 | 1.76 |
| SN642 | 3 | 12.398 | 126.65 | 1.02 | 1.52 | 1.80 |
| SN112 | 4 | 5.763 | 98.38 | 1.71 | 0.43 | 1.69 |
| SN312 | 4 | 6.459 | 100.90 | 1.56 | 0.75 | 1.97 |
| SN222 | 4 | 7.375 | 104.53 | 1.42 | 0.72 | 1.62 |
| SU422 | 4 | 8.278 | 106.33 | 1.28 | 0.90 | 1.65 |
| SN332 | 4 | 9.477 | 133.73 | 1.41 | 0.13 | 1.76 |
| SN532 | 4 | 10.628 | 136.33 | 1.28 | 0.60 | 1.50 |
| SN442 | 4 | 11.831 | 136.55 | 1.15 | 0.69 | 1.38 |
| SN642 | 4 | 13.309 | 135.96 | 1.02 | 0.81 | 1.42 |
| SN112 | 5 | 6.818 | 116.39 | 1.71 | 0.41 | 1.69 |
| SN312 | 5 | 7.247 | 113.21 | 1.56 | 0.60 | 2.32 |
| SN222 | 5 | 8.488 | 120.31 | 1.42 | 0.57 | 1.79 |
| SU422 | 5 | 9.095 | 116.82 | 1.28 | 0.74 | 1.83 |
| SN332 | 5 | 10.623 | 149.90 | 1.41 | 0.24 | 2.08 |
| SN532 | 5 | 11.462 | 147.03 | 1.28 | 0.52 | 1.83 |
| SN442 | 5 | 12.995 | 149.98 | 1.15 | 0.56 | 1.68 |
| SN642 | 5 | 14.115 | 144.19 | 1.02 | 0.83 | 1.61 |
| SN112 | 6 | 7.3 | 124.61 | 1.71 | 0.66 | 1.05 |
| SN312 | 6 | 7.6 | 118.72 | 1.56 | 1.07 | 1.68 |
| SN222 | 6 | 9 | 127.56 | 1.42 | 0.70 | 1.29 |
| SU422 | 6 | 9.5 | 122.02 | 1.28 | 1.09 | 1.18 |
| SN332 | 6 | 11.1 | 156.64 | 1.41 | 0.60 | 1.80 |
| SN532 | 6 | 11.8 | 151.36 | 1.28 | 0.81 | 1.36 |
| SN442 | 6 | 13.5 | 155.81 | 1.15 | 0.78 | 1.39 |
| SN642 | 6 | 14.5 | 148.13 | 1.02 | 0.96 | 1.09 |
| SN112 | 7 | 7.3 | 124.61 | 1.71 | 0.54 | 0.71 |
| SN312 | 7 | 7.6 | 118.72 | 1.56 | 0.74 | 1.24 |
| SN222 | 7 | 9 | 127.56 | 1.42 | 0.49 | 1.14 |
| SU442 | 7 | 9.5 | 122.02 | 1.28 | 1.00 | 0.84 |
| SN332 | 7 | 11.1 | 156.64 | 1.41 | 0.66 | 1.89 |
| SN532 | 7 | 11.8 | 151.36 | 1.28 | 0.71 | 1.48 |
| SN442 | 7 | 13.5 | 155.81 | 1.15 | 0.66 | 1.53 |
| SN642 | 7 | 14.5 | 148.13 | 1.02 | 0.87 | 1.17 |
| SN112 | 8 | 7.3 | 124.61 | 1.71 | 0.64 | 0.85 |
| SN312 | 8 | 7.6 | 118.72 | 1.56 | 0.60 | 2.23 |
| SN222 | 8 | 9 | 127.56 | 1.42 | 0.40 | 0.99 |
| SU422 | 8 | 9.5 | 122.02 | 1.28 | 0.73 | 0.18 |
| SN332 | 8 | 11.1 | 156.64 | 1.41 | 0.69 | 1.98 |
| SN532 | 8 | 11.8 | 151.36 | 1.28 | 0.80 | 1.26 |
| SN442 | 8 | 13.5 | 155.81 | 1.15 | 0.80 | 1.31 |
| SN642 | 8 | 14.5 | 148.13 | 1.02 | 0.98 | 0.94 |
| SN222 | 9 | | ERR | ERR | | |
| SN312 | 9 | | ERR | ERR | | |
| SU422 | 9 | | ERR | ERR | | |
| SN112 | 9 | | ERR | ERR | | |
| SN332 | 9 | 11.1 | 156.64 | 1.41 | 0.78 | 5.49 |
| SN532 | 9 | 11.8 | 151.36 | 1.28 | 0.88 | 2.72 |
| SN442 | 9 | 13.5 | 155.81 | 1.15 | 0.47 | 1.75 |
| SN642 | 9 | 14.5 | 148.13 | 1.02 | 0.60 | 0.87 |

Table 5.4: Inertia Coefficient Estimates from Measured Kinematics.

| TEST | T (s) | F-X (N/m) | U (cm/s) | Cm | KC | Re | BETA | *Cm |
|------|----------|--------------|-------------|------|------|-------|-------|------|
| SN11 | 1.69 | 20.48 | 18 | 1.35 | 1.79 | 30600 | 17070 | 1.17 |
| SN22 | 1.85 | 25.92 | 26 | 1.29 | 2.83 | 44200 | 15622 | 1.10 |
| SN33 | 2.05 | 34.28 | 40 | 1.23 | 4.82 | 68000 | 14111 | 1.12 |
| SN44 | 2.25 | 35.65 | 40 | 1.41 | 5.30 | 68000 | 12827 | 0.94 |
| SN31 | 2.04 | 25.40 | 30 | 1.21 | 3.60 | 51000 | 14174 | 1.24 |
| SU42 | 2.25 | 22.43 | 32 | 1.10 | 4.24 | 54400 | 12844 | 0.98 |
| SN53 | 2.50 | 26.45 | 36 | 1.29 | 5.30 | 61200 | 11542 | 0.85 |
| SN64 | 2.83 | 34.76 | 50 | 1.38 | 8.32 | 85000 | 10216 | 0.95 |
| SB11 | 1.82 | 22.81 | 22 | 1.32 | 2.35 | 37400 | 15888 | |
| SC12 | 1.82 | 33.73 | 31 | 1.39 | 3.32 | 52700 | 15853 | |
| SB14 | 2.21 | 23.15 | 31 | 1.15 | 4.02 | 52700 | 13095 | |
| SB15 | 2.21 | 32.44 | 45 | 1.11 | 5.85 | 76500 | 13083 | |
| SC17 | 2.76 | 33.48 | 49 | 1.32 | 7.94 | 83300 | 10490 | |
| SB31 | 1.72 | 22.10 | 20 | 1.33 | 2.02 | 34000 | 16832 | |
| SB32 | 1.72 | 30.75 | 27 | 1.37 | 2.73 | 45900 | 16832 | |
| SC34 | 2.07 | 22.00 | 23 | 1.39 | 2.80 | 39100 | 13955 | |
| SC35 | 2.07 | 31.32 | 31 | 1.46 | 3.78 | 52700 | 13955 | |
| SB37 | 2.56 | 27.84 | 38 | 1.31 | 5.72 | 64600 | 11285 | |
| SC41 | 1.55 | 19.96 | 17 | 1.27 | 1.55 | 28900 | 18645 | |
| SC42 | 1.55 | 26.29 | 20 | 1.43 | 1.82 | 34000 | 18657 | |
| SC44 | 1.85 | 20.54 | 21 | 1.27 | 2.29 | 35700 | 15622 | |
| SC45 | 1.85 | 28.42 | 28 | 1.32 | 3.05 | 47600 | 15613 | |
| SC47 | 2.25 | 29.27 | 36 | 1.28 | 4.76 | 61200 | 12850 | |
| SRE4 | 2.07 | 29.40 | 30 | 1.42 | 3.66 | 51000 | 13948 | |
| SRE3 | 2.07 | 30.58 | 30 | 1.48 | 3.65 | 51000 | 13955 | |
| SRE2 | 2.07 | 30.31 | 30 | 1.47 | 3.66 | 51000 | 13948 | |
| SRE1 | 2.07 | 31.33 | 30 | 1.52 | 3.66 | 51000 | 13941 | |
| SCP1 | 2.07 | 31.95 | 33 | 1.40 | 4.02 | 56100 | 13948 | |

* - Results from analysis using predicted velocities

Table 5.5: Lift Force Data.

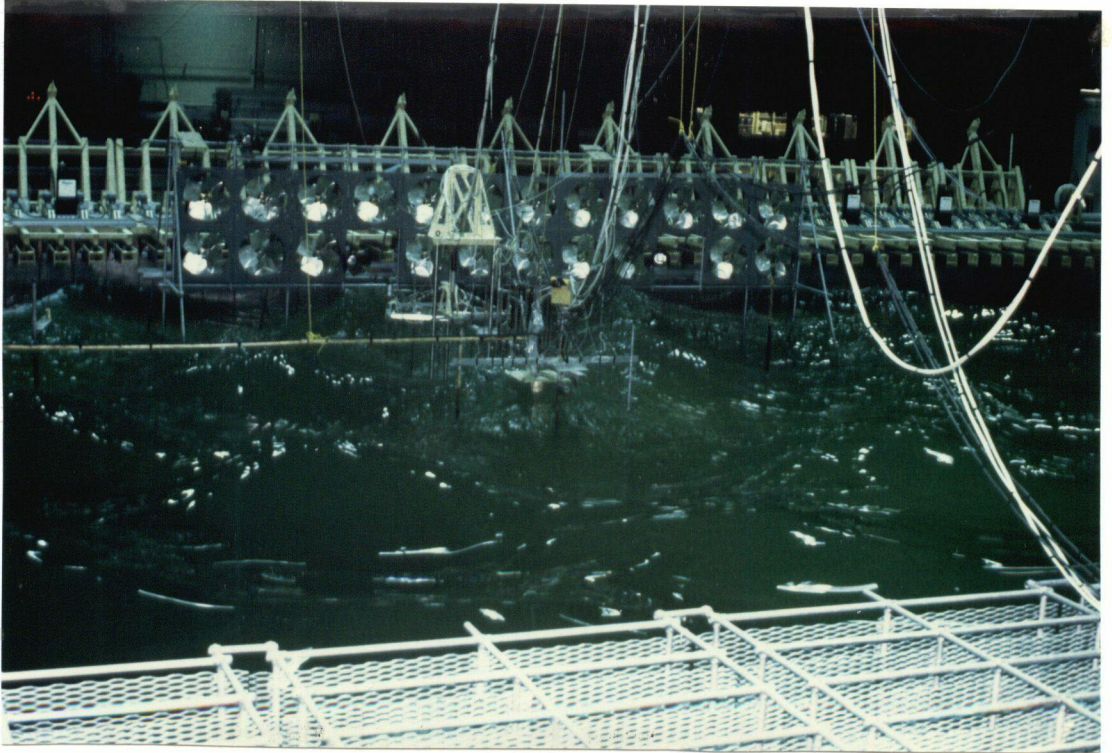
| TEST | MAX. LIFT FORCE AMPL. | | | AVE. LIFT FORCE PERIOD | | | KEULEGAN-CARPENTER NO. | | |
|------|-----------------------|-------|-------|------------------------|-------|-------|------------------------|-------|-------|
| | SEG 1 | SEG 2 | SEG 3 | SEG 1 | SEG 2 | SEG 3 | SEG 1 | SEG 2 | SEG 3 |
| SN11 | 0.85 | 0.52 | 0.51 | 1.47 | 1.46 | 1.66 | 4.65 | 3.33 | 2.08 |
| SN22 | 1.27 | 0.96 | 0.73 | 1.20 | 1.49 | 1.86 | 6.17 | 4.67 | 3.20 |
| SN33 | 5.06 | 4.30 | 1.87 | 1.01 | 1.13 | 1.47 | 8.20 | 6.57 | 4.89 |
| SN44 | 8.92 | 6.21 | 2.95 | 1.13 | 1.13 | 1.14 | 10.51 | 8.77 | 6.96 |
| SN31 | 2.24 | 1.14 | 0.70 | 1.09 | 1.03 | 1.54 | 5.59 | 4.46 | 3.31 |
| SU42 | 3.11 | 2.36 | 1.04 | 1.13 | 1.09 | 1.16 | 7.36 | 6.14 | 4.86 |
| SN53 | 4.81 | 3.92 | 1.86 | 1.24 | 1.24 | 1.35 | 9.68 | 8.38 | 7.01 |
| SN64 | 8.89 | 7.68 | 3.96 | 1.39 | 1.36 | 1.42 | 12.38 | 11.10 | 9.70 |
| SB11 | 1.45 | 0.82 | 0.49 | 1.40 | 1.33 | 1.65 | 5.67 | 4.25 | 2.87 |
| SC12 | 4.75 | 3.22 | 1.42 | 0.95 | 0.97 | 1.36 | 8.04 | 6.03 | 4.07 |
| SB14 | 3.72 | 2.59 | 1.08 | 1.15 | 1.06 | 1.66 | 6.71 | 5.56 | 4.35 |
| SB15 | 7.21 | 4.72 | 2.19 | 1.11 | 1.09 | 1.37 | 9.55 | 7.91 | 6.20 |
| SB17 | 11.74 | 9.68 | 4.80 | 1.58 | 1.58 | 1.39 | 12.11 | 10.79 | 9.35 |
| SB31 | 0.92 | 0.60 | 0.49 | 1.34 | 1.46 | 1.68 | 5.04 | 3.64 | 2.31 |
| SB32 | 3.15 | 2.24 | 1.08 | 1.17 | 1.40 | 1.65 | 6.99 | 5.04 | 3.21 |
| SC34 | 1.84 | 1.27 | 0.72 | 1.16 | 1.09 | 1.63 | 5.90 | 4.74 | 3.56 |
| SC35 | 4.51 | 4.44 | 1.78 | 1.04 | 1.04 | 1.42 | 8.11 | 6.53 | 4.90 |
| SB37 | 5.42 | 4.10 | 1.85 | 1.27 | 1.26 | 1.31 | 10.17 | 8.87 | 7.49 |
| SC41 | 0.89 | 0.54 | 0.37 | 1.39 | 0.93 | 1.25 | 3.80 | 2.54 | 1.44 |
| SC42 | 1.49 | 1.02 | 1.09 | 1.26 | 1.36 | 1.56 | 5.01 | 3.35 | 1.90 |
| SC44 | 0.96 | 0.72 | 0.48 | 1.18 | 1.62 | 1.77 | 4.49 | 3.40 | 2.33 |
| SC45 | 2.64 | 2.30 | 1.11 | 0.98 | 1.27 | 1.67 | 6.14 | 4.65 | 3.19 |
| SC47 | 4.75 | 4.71 | 2.01 | 1.13 | 1.13 | 1.26 | 7.49 | 6.24 | 4.95 |
| SRE4 | 3.64 | 9.32 | 1.19 | 1.09 | 1.22 | 1.51 | 8.12 | 6.53 | 4.90 |
| SRE3 | 3.97 | 4.53 | 1.61 | 1.04 | 1.14 | 1.29 | 8.11 | 6.53 | 4.90 |
| SRE2 | 4.39 | 3.84 | 1.61 | 1.03 | 1.11 | 1.24 | 8.12 | 6.53 | 4.90 |
| SRE1 | 4.30 | 3.79 | 1.66 | 1.03 | 1.03 | 1.14 | 8.12 | 6.54 | 4.90 |
| SCP1 | 4.17 | 4.04 | 1.74 | 1.03 | 1.02 | 1.36 | 8.12 | 6.53 | 4.90 |
| SCP2 | 6.48 | 4.77 | 1.92 | 1.01 | 1.00 | 1.37 | | | |
| SCP3 | 8.49 | 7.61 | 3.66 | 2.06 | 2.06 | 2.06 | | | |
| SCP4 | 13.33 | 11.15 | 5.66 | 2.07 | 2.07 | 2.07 | | | |
| SCP5 | 17.88 | 14.99 | 7.54 | 2.07 | 1.95 | 1.95 | | | |

Table 5.6: Predicted and Measured Total In-Line Force Maxima.

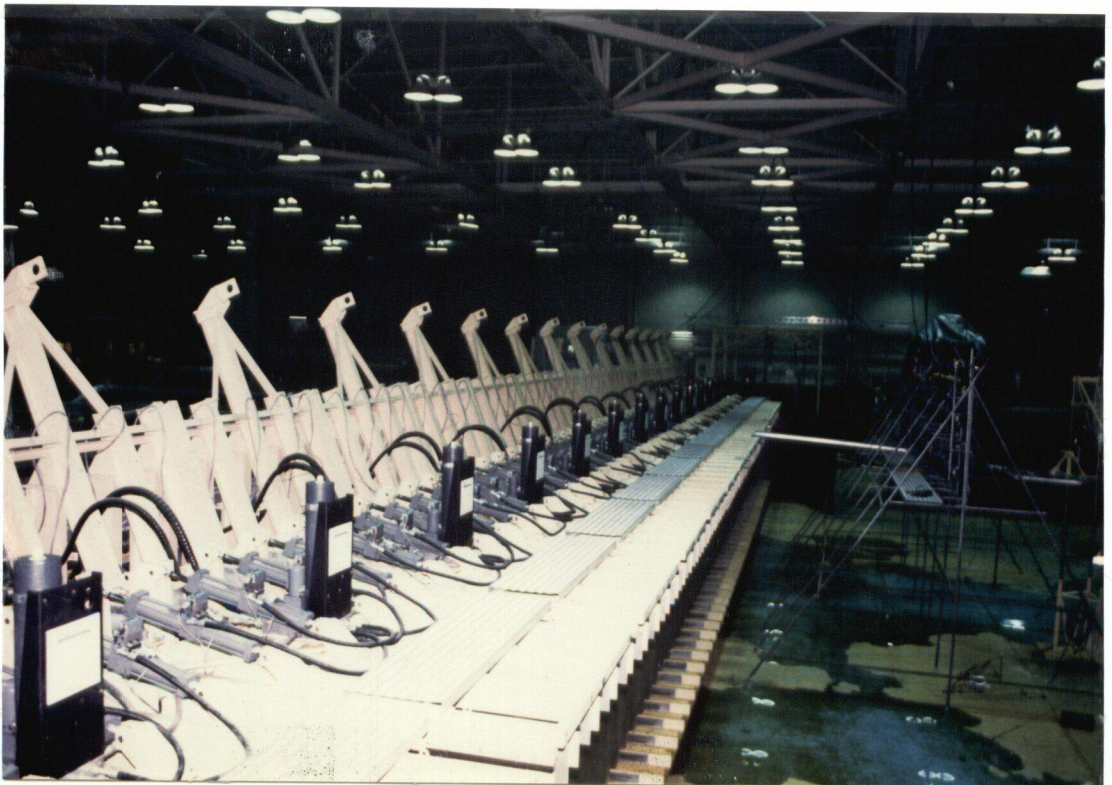
| TEST | H (m) | T (s) | ALPHA (DEG) | PHASE (DEG) | MEASURED FORCE (N) | | | PREDICTED FORCE (N) | | |
|------|-------|-------|----------------|----------------|--------------------|--------|--------|---------------------|--------|--------|
| | | | | | POS | NEG | DIFF | POS | NEG | DIFF |
| SN11 | 0.393 | 1.693 | 0 | 0 | 58.85 | -61.99 | 120.84 | 64.52 | -62.28 | 126.80 |
| SN22 | 0.479 | 1.850 | 0 | 0 | 83.99 | -61.62 | 145.61 | 75.41 | -70.84 | 146.25 |
| SN33 | 0.581 | 2.048 | 0 | 0 | 102.78 | -68.94 | 171.72 | 87.87 | -79.93 | 167.80 |
| SN44 | 0.684 | 2.253 | 0 | 0 | 128.60 | -61.00 | 189.60 | 100.95 | -87.12 | 188.07 |
| SN31 | 0.397 | 2.039 | 0 | 0 | 69.37 | -59.83 | 129.20 | 55.55 | -53.79 | 109.34 |
| SU42 | 0.479 | 2.250 | 0 | 0 | 60.92 | -59.86 | 120.78 | 63.29 | -59.60 | 122.89 |
| SN53 | 0.572 | 2.504 | 0 | 0 | 78.40 | -55.91 | 134.31 | 72.00 | -65.33 | 137.33 |
| SN64 | 0.654 | 2.829 | 0 | 0 | 97.41 | -60.19 | 157.60 | 78.46 | -67.09 | 145.55 |
| SB11 | 0.463 | 1.819 | 30 | 0 | 70.43 | -56.80 | 127.23 | 70.98 | -67.51 | 138.49 |
| SC12 | 0.655 | 1.823 | 30 | 0 | 111.84 | -76.73 | 188.57 | 111.48 | -97.89 | 209.37 |
| SB14 | 0.460 | 2.207 | 30 | 0 | 62.47 | -59.48 | 121.95 | 59.18 | -56.41 | 115.59 |
| SB15 | 0.655 | 2.209 | 30 | 0 | 104.64 | -58.39 | 163.03 | 93.02 | -81.97 | 174.99 |
| SC17 | 0.679 | 2.755 | 30 | 0 | 98.00 | -59.08 | 157.08 | 81.06 | -69.06 | 150.12 |
| SB31 | 0.485 | 1.717 | 60 | 0 | 71.63 | -59.26 | 130.89 | 70.53 | -66.87 | 137.40 |
| SB32 | 0.672 | 1.717 | 60 | 0 | 96.01 | -68.89 | 164.90 | 108.31 | -95.32 | 203.63 |
| SC34 | 0.477 | 2.071 | 60 | 0 | 59.46 | -52.34 | 111.80 | 58.32 | -55.76 | 114.08 |
| SC35 | 0.657 | 2.071 | 60 | 0 | 90.74 | -67.03 | 157.77 | 87.35 | -78.41 | 165.76 |
| SB37 | 0.680 | 2.561 | 60 | 0 | 76.58 | -56.76 | 133.34 | 75.66 | -66.58 | 142.24 |
| SC41 | 0.498 | 1.550 | 90 | 0 | 69.84 | -64.41 | 134.25 | 64.16 | -61.16 | 125.32 |
| SC42 | 0.657 | 1.549 | 90 | 0 | 93.15 | -70.45 | 163.60 | 92.72 | -84.04 | 176.76 |
| SC44 | 0.493 | 1.850 | 90 | 0 | 62.94 | -50.92 | 113.86 | 53.99 | -51.70 | 105.69 |
| SC45 | 0.674 | 1.851 | 90 | 0 | 80.45 | -78.90 | 159.35 | 80.54 | -73.34 | 153.88 |
| SC47 | 0.690 | 2.249 | 90 | 0 | 82.01 | -63.89 | 145.90 | 68.95 | -62.68 | 131.63 |
| SRE4 | 0.675 | 2.072 | 60 | 0 | 86.45 | -62.76 | 149.21 | 90.62 | -80.75 | 171.37 |
| SRE3 | 0.676 | 2.071 | 60 | 0 | 88.63 | -66.78 | 155.41 | 90.83 | -80.82 | 171.65 |
| SRE2 | 0.673 | 2.072 | 60 | 0 | 90.27 | -64.88 | 155.15 | 90.32 | -80.42 | 170.74 |
| SRE1 | 0.684 | 2.073 | 60 | 0 | 90.54 | -68.99 | 159.53 | 92.24 | -81.85 | 174.09 |
| SCP1 | 0.675 | 2.072 | 60 | 0 | 97.37 | -67.03 | 164.40 | 90.62 | -80.75 | 171.37 |
| SCP2 | 0.675 | 2.072 | 60 | 45 | 69.32 | -67.07 | 136.39 | 81.48 | -74.11 | 155.59 |
| SCP3 | 0.675 | 2.072 | 60 | 90 | 43.80 | -53.77 | 97.57 | 58.28 | -55.70 | 113.98 |
| SCP4 | 0.675 | 2.072 | 60 | 135 | 27.40 | -31.61 | 59.01 | 29.69 | -29.50 | 59.19 |
| SCP5 | 0.675 | 2.072 | 60 | 180 | 35.12 | -29.50 | 64.62 | 0.00 | 0.00 | 0.00 |

Table 5.7: Repeatability Data.

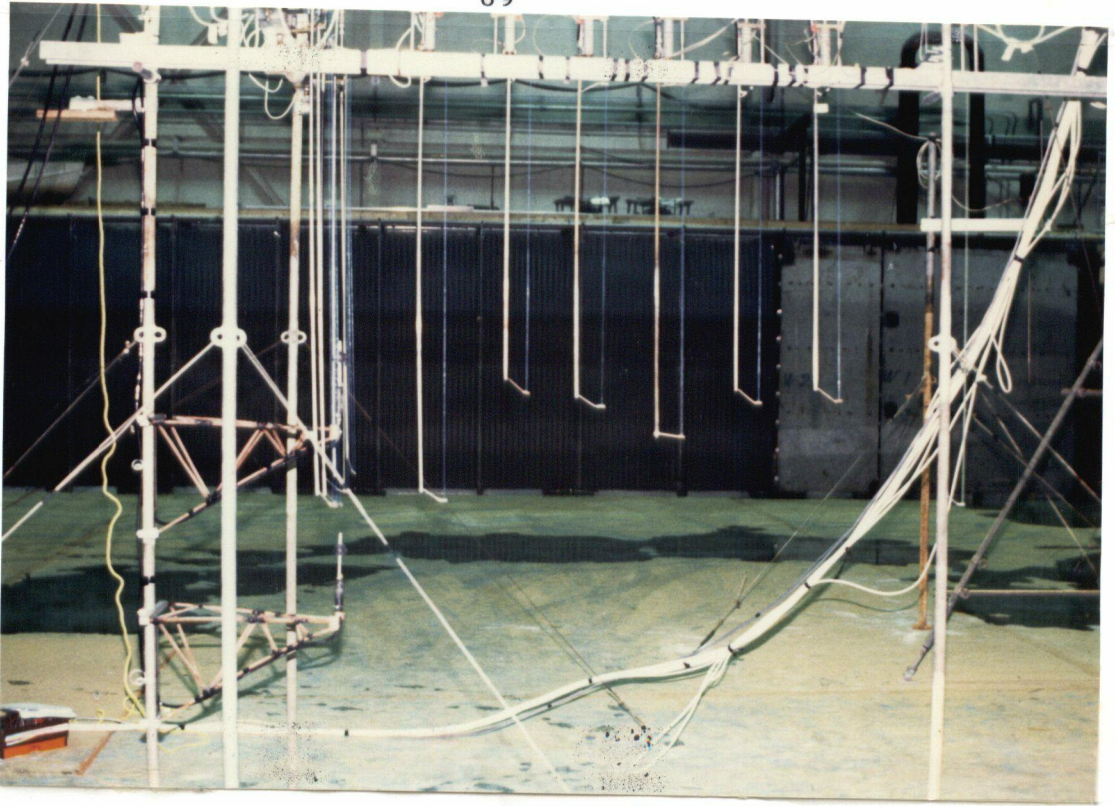
| TEST: PARAMETER: | REP 0 | REP 1 | REP 2 | REP 3 | REP 4 | C35 | AVERAGE | STD DEV |
|---------------------|--------|--------|--------|--------|--------|--------|---------|---------|
| HZAVE (m) | 0.675 | 0.684 | 0.673 | 0.676 | 0.675 | 0.657 | 0.673 | 0.008 |
| TZAVE (s) | 2.072 | 2.073 | 2.072 | 2.071 | 2.072 | 2.071 | 2.072 | 0.001 |
| SAVE | 0.088 | 0.088 | 0.087 | 0.086 | 0.088 | 0.086 | 0.087 | 0.001 |
| CFSAVE | 0.209 | 0.207 | 0.208 | 0.201 | 0.209 | 0.199 | 0.206 | 0.004 |
| SEGMENT 1 | | | | | | | | |
| Fx max (N) | 31.951 | 31.325 | 30.312 | 30.575 | 29.401 | 31.316 | 30.813 | 0.828 |
| Fy max (N) | 6.660 | 6.122 | 5.700 | 5.525 | 4.595 | 5.797 | 5.733 | 0.626 |
| Fr max (N) | 31.953 | 31.343 | 31.657 | 31.208 | 29.600 | 31.559 | 31.220 | 0.762 |
| SEGMENT 2 | | | | | | | | |
| Fx max (N) | 51.605 | 49.978 | 48.072 | 48.681 | 46.452 | 49.000 | 48.965 | 1.591 |
| Fy max (N) | 14.485 | 14.185 | 15.380 | 13.292 | 24.701 | 13.472 | 15.919 | 3.987 |
| Fr max (N) | 51.768 | 50.686 | 50.713 | 50.535 | 49.893 | 50.330 | 50.654 | 0.569 |
| COLUMN | | | | | | | | |
| Fx max (N) | 97.370 | 90.540 | 90.270 | 88.630 | 86.450 | 90.740 | 90.667 | 3.343 |



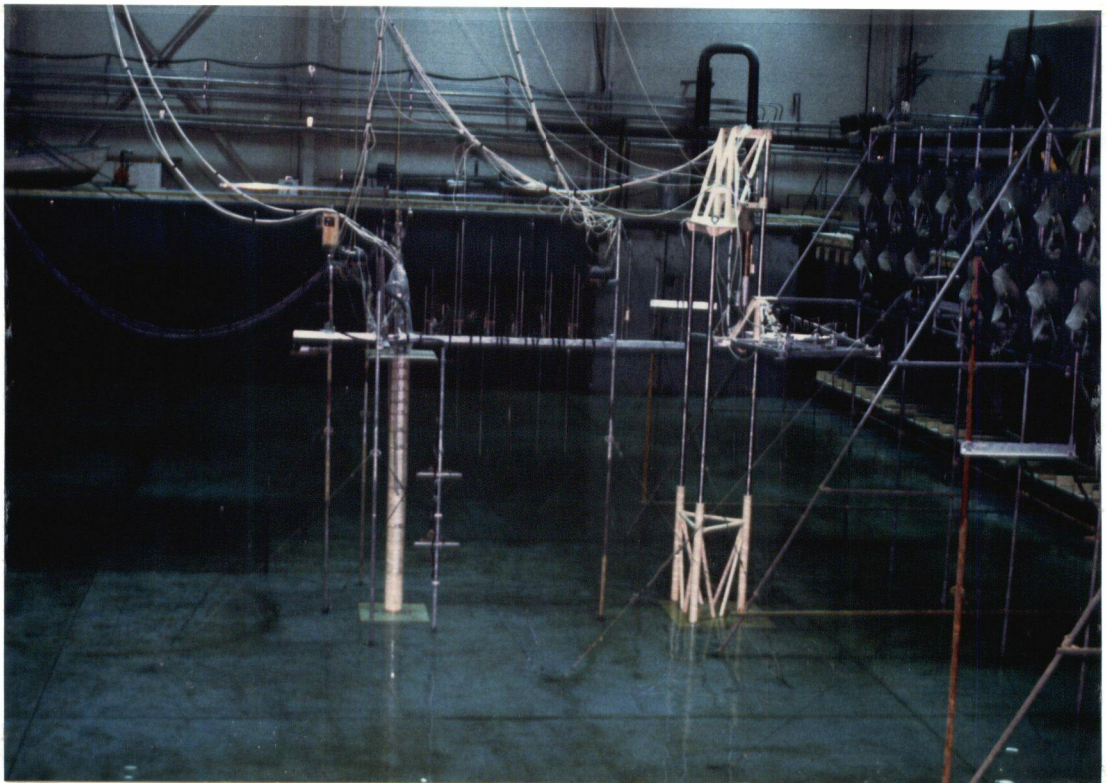
Photograph 1.1: General View of the Offshore Wave Basin and A Regular Short-Crested Wave Field.



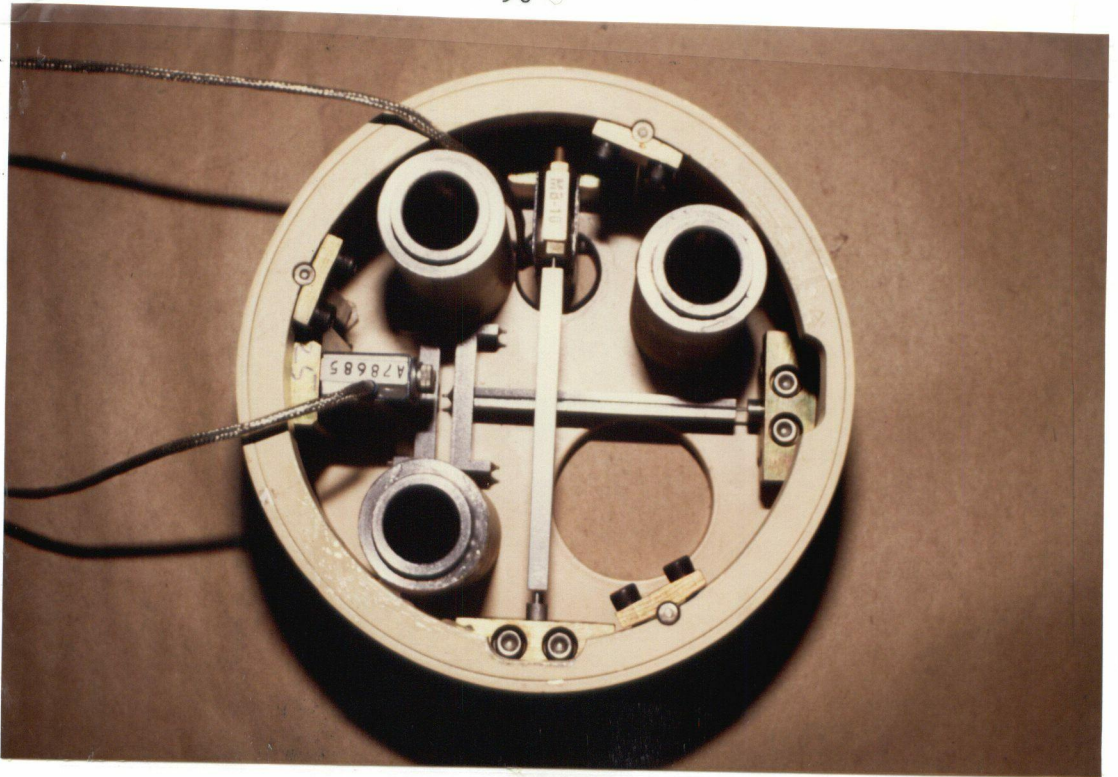
Photograph 3.1: View Along the Top of the Segmented Wave Machine.



Photograph 3.2: Close-Up View of the Phase 1 Test Apparatus.



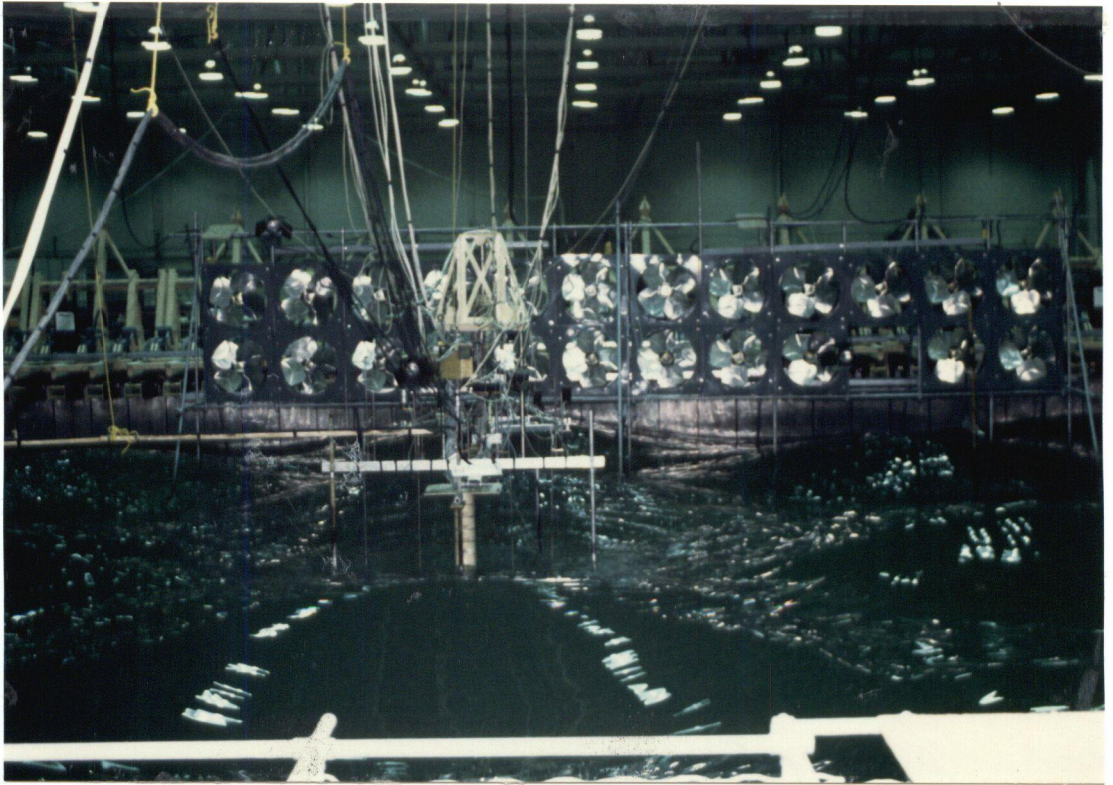
Photograph 3.3: View of the Phase 2 Test Apparatus.



Photograph 3.4: Close-Up View Down Into One Segment.



Photograph 3.5: The Author Conducting an Initial Condition Calibration Test.



Photograph 5.1: View of Short-Crested Waves and the Segmented Column.

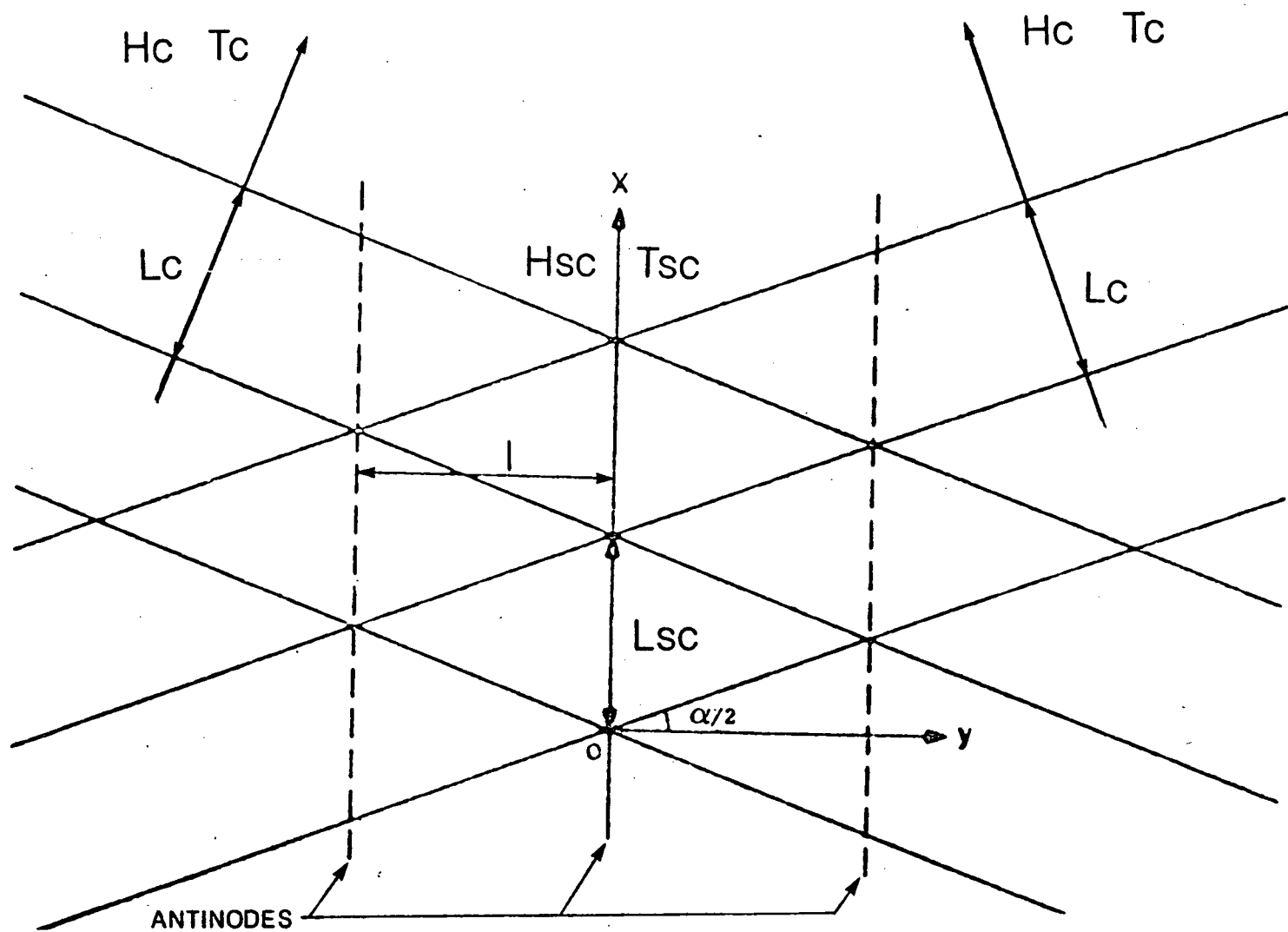


Figure 2.1: Definition sketch of crossing wave flow.

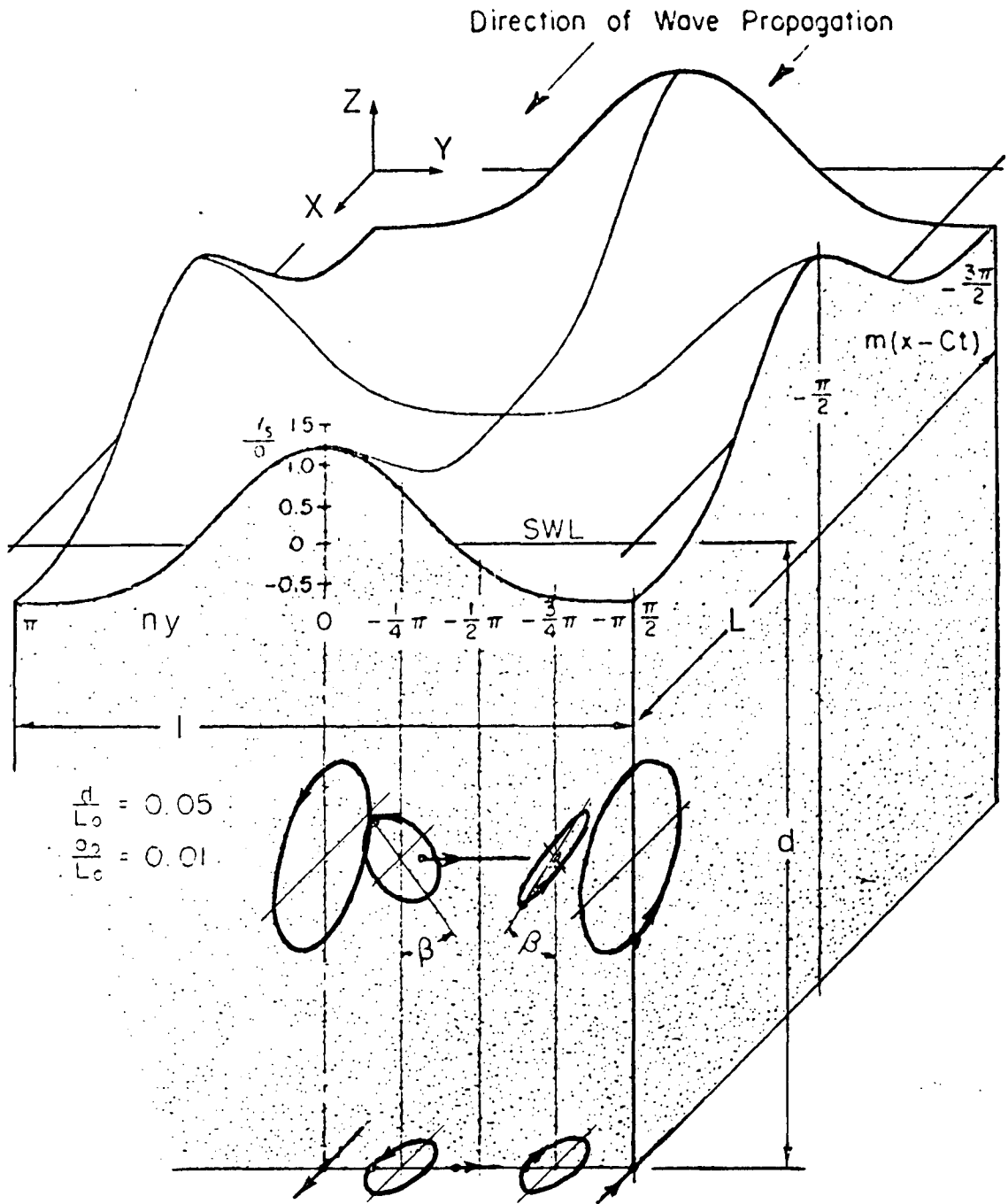


Figure 2.2: Water particle orbits under crossing waves (from Fuchs, 1951).

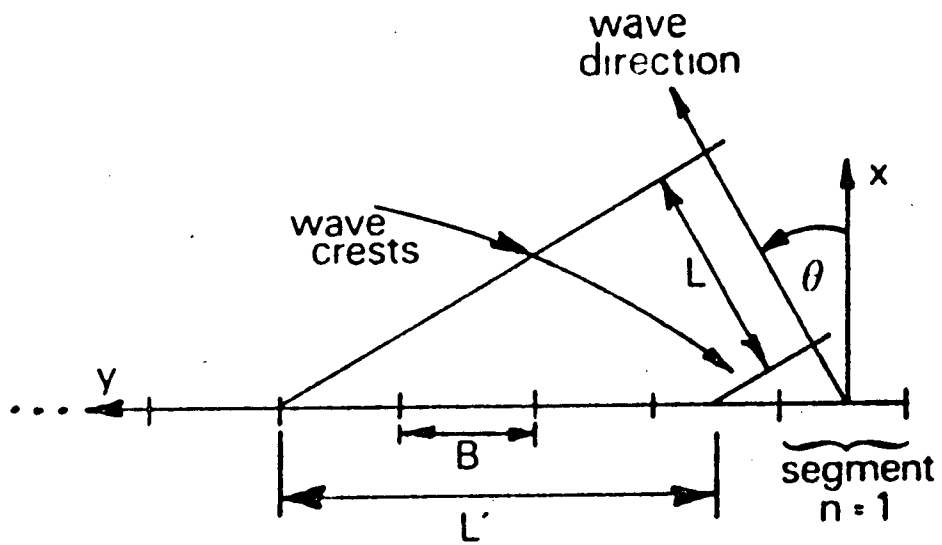


Figure 2.3: Definition sketch of oblique wave generation.

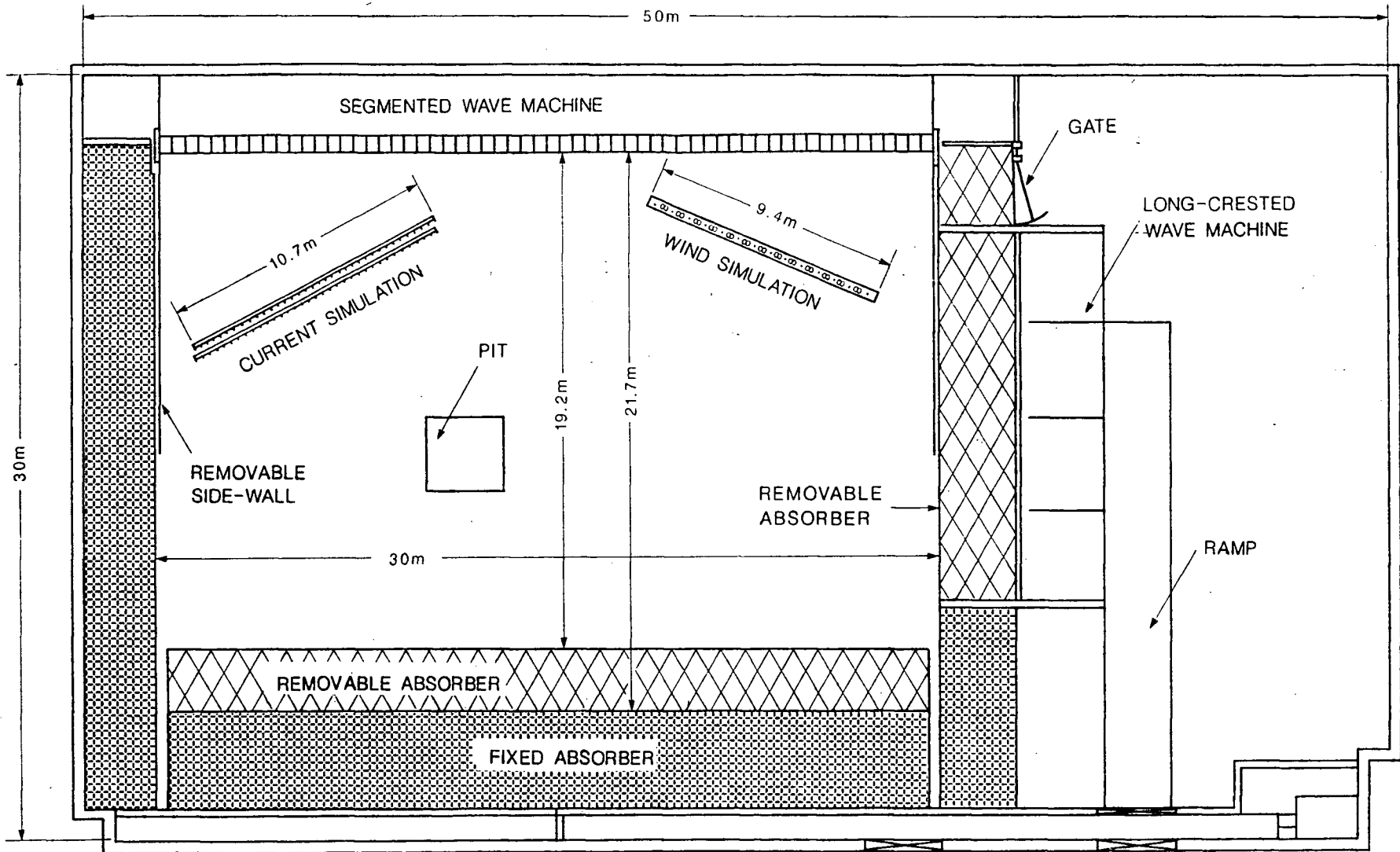


Figure 3.1: Plan of the Offshore Wave Basin.

SEGMENTED WAVE MACHINE

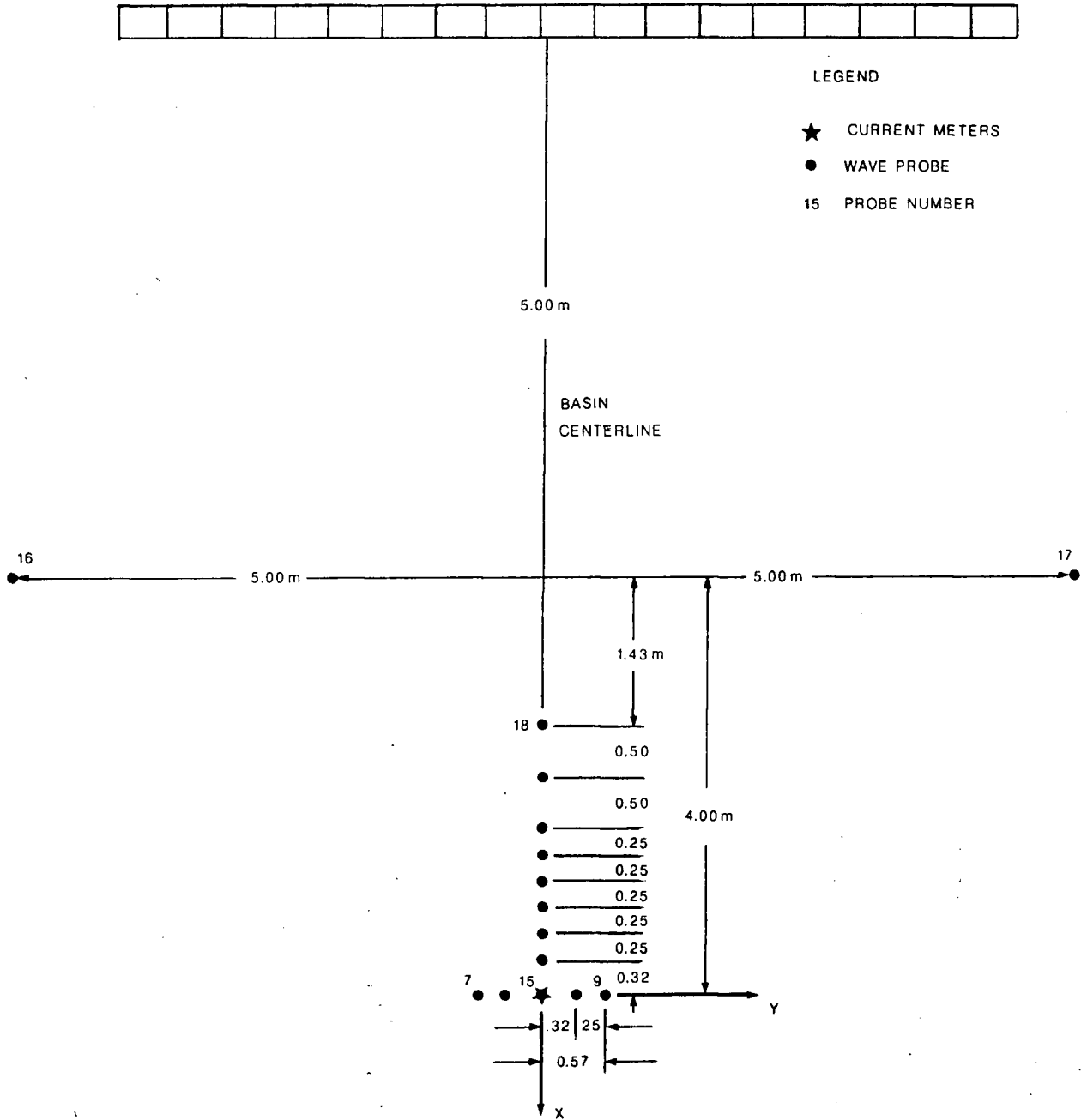


Figure 3.2: Plan of instrumentation during phase 1.

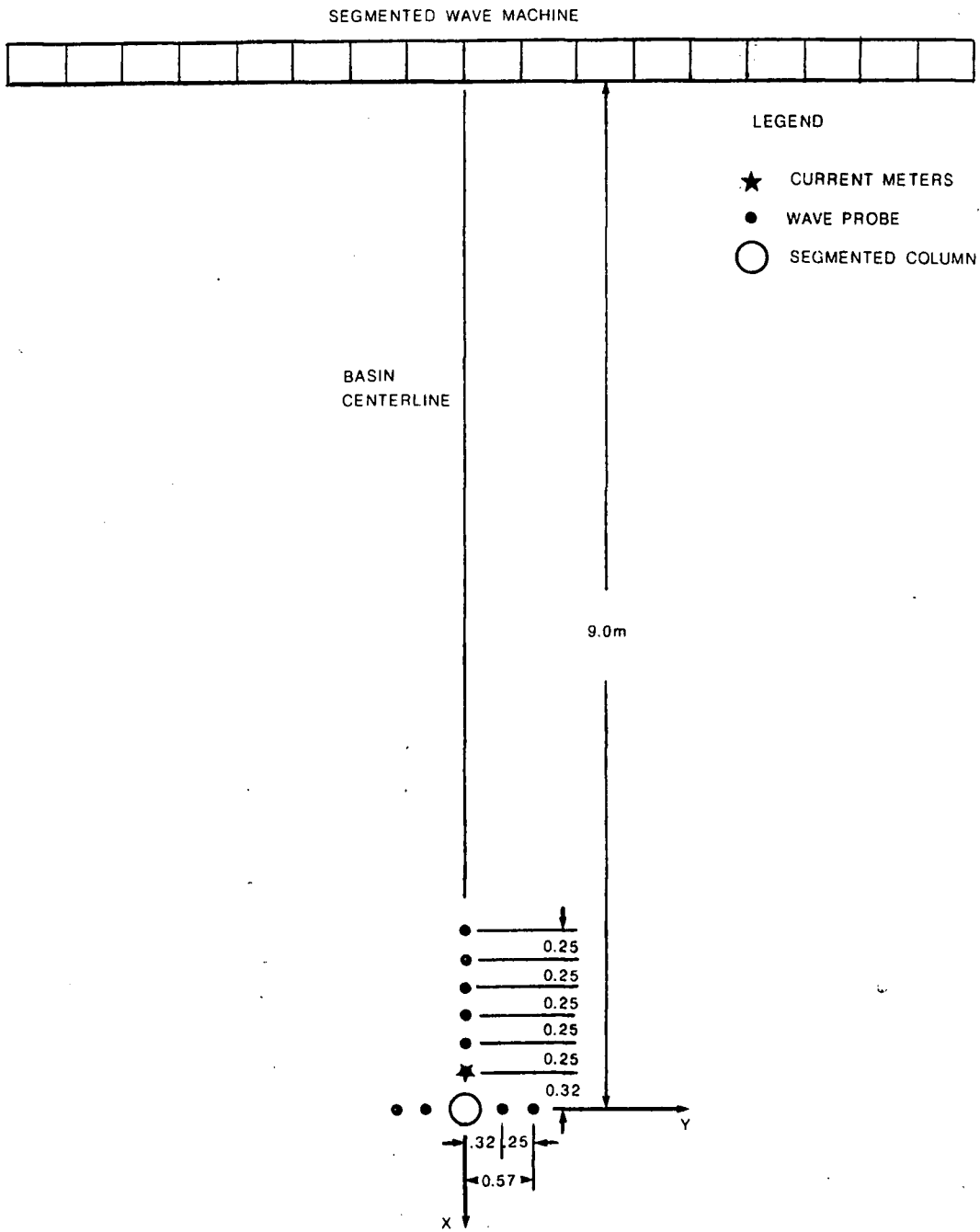


Figure 3.3: Plan of instrumentation during phase 2.

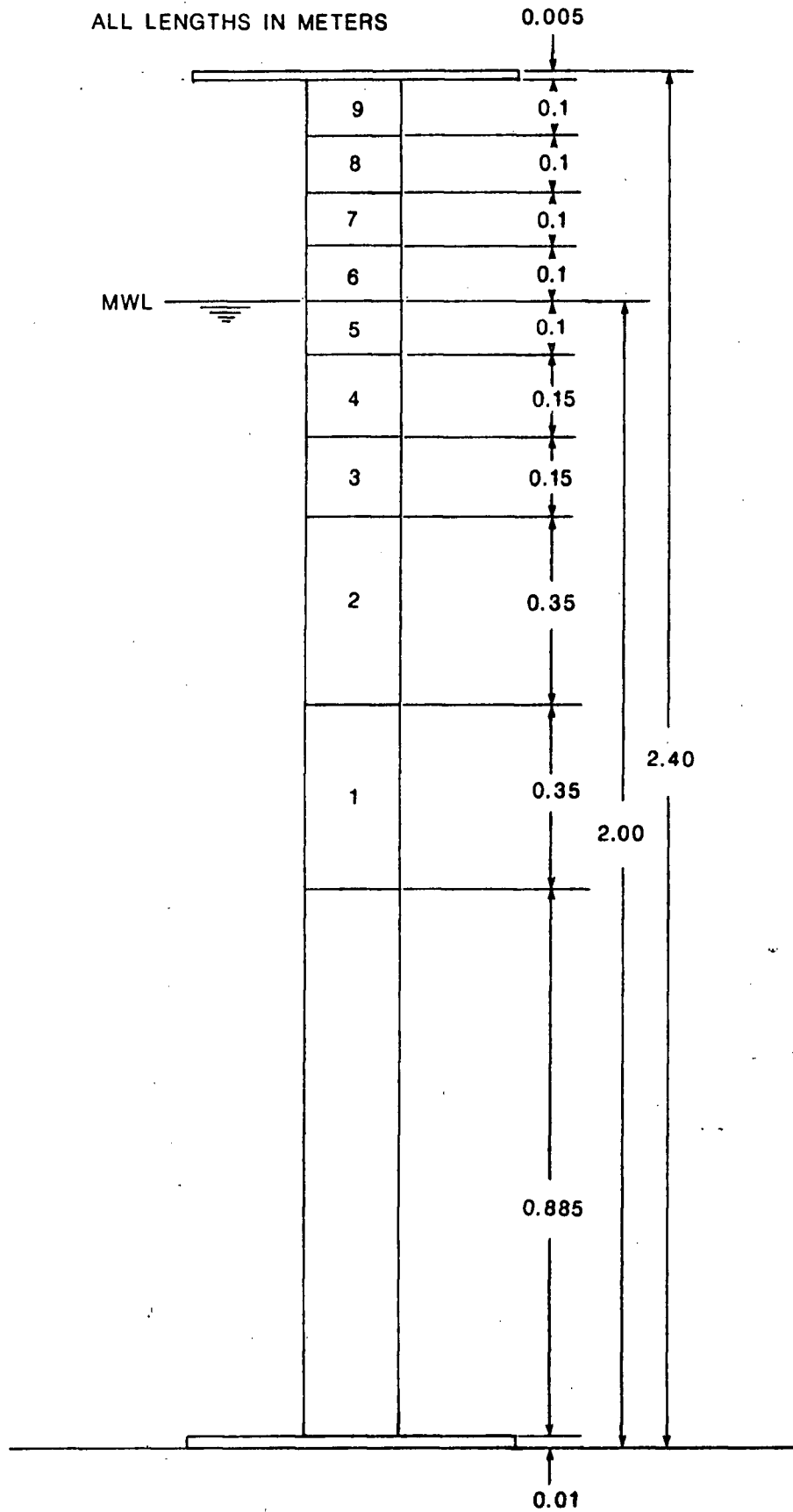


Figure 3.4: Sketch of the segmented column.

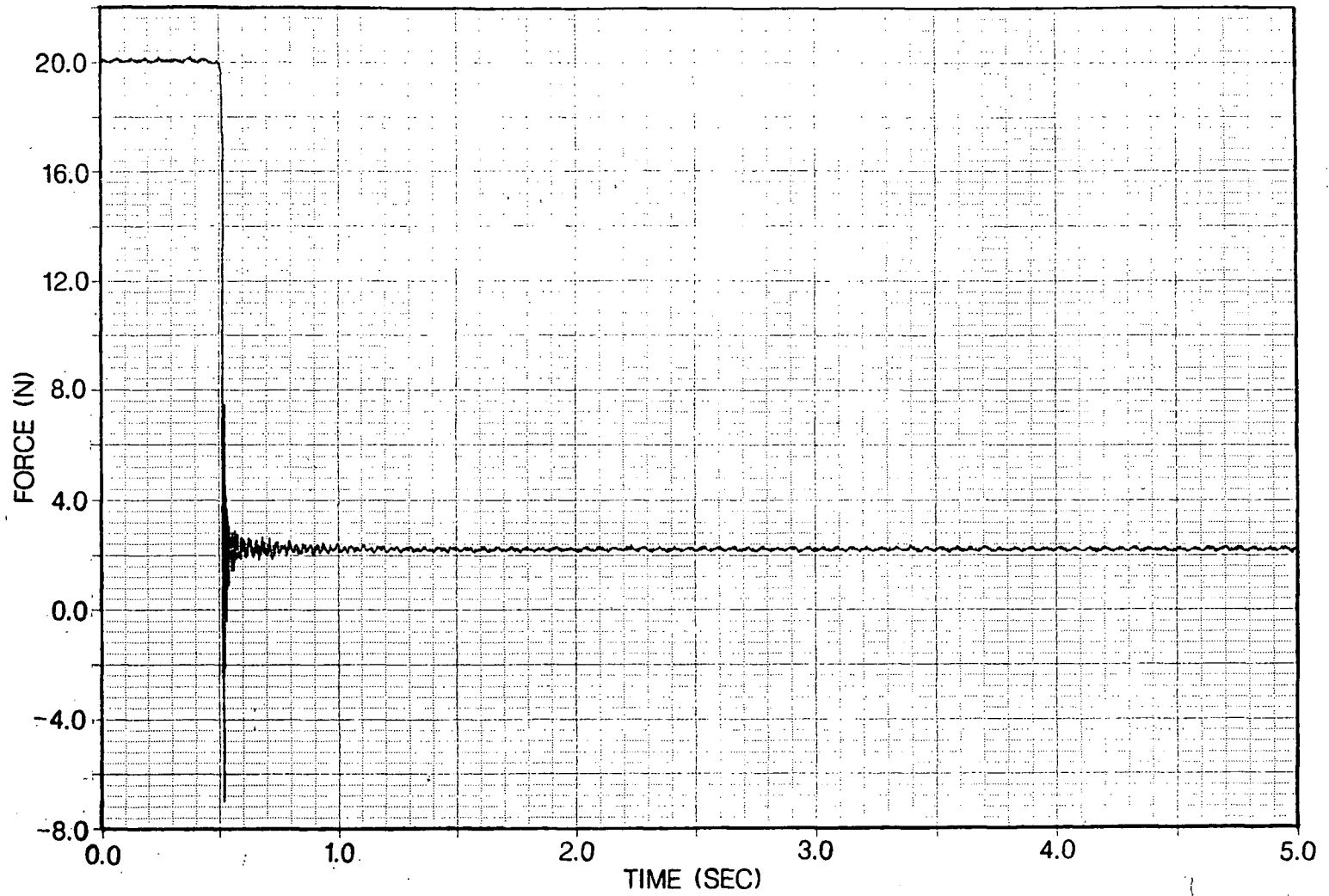


Figure 3.5: Initial condition test response of transducer 4-X.

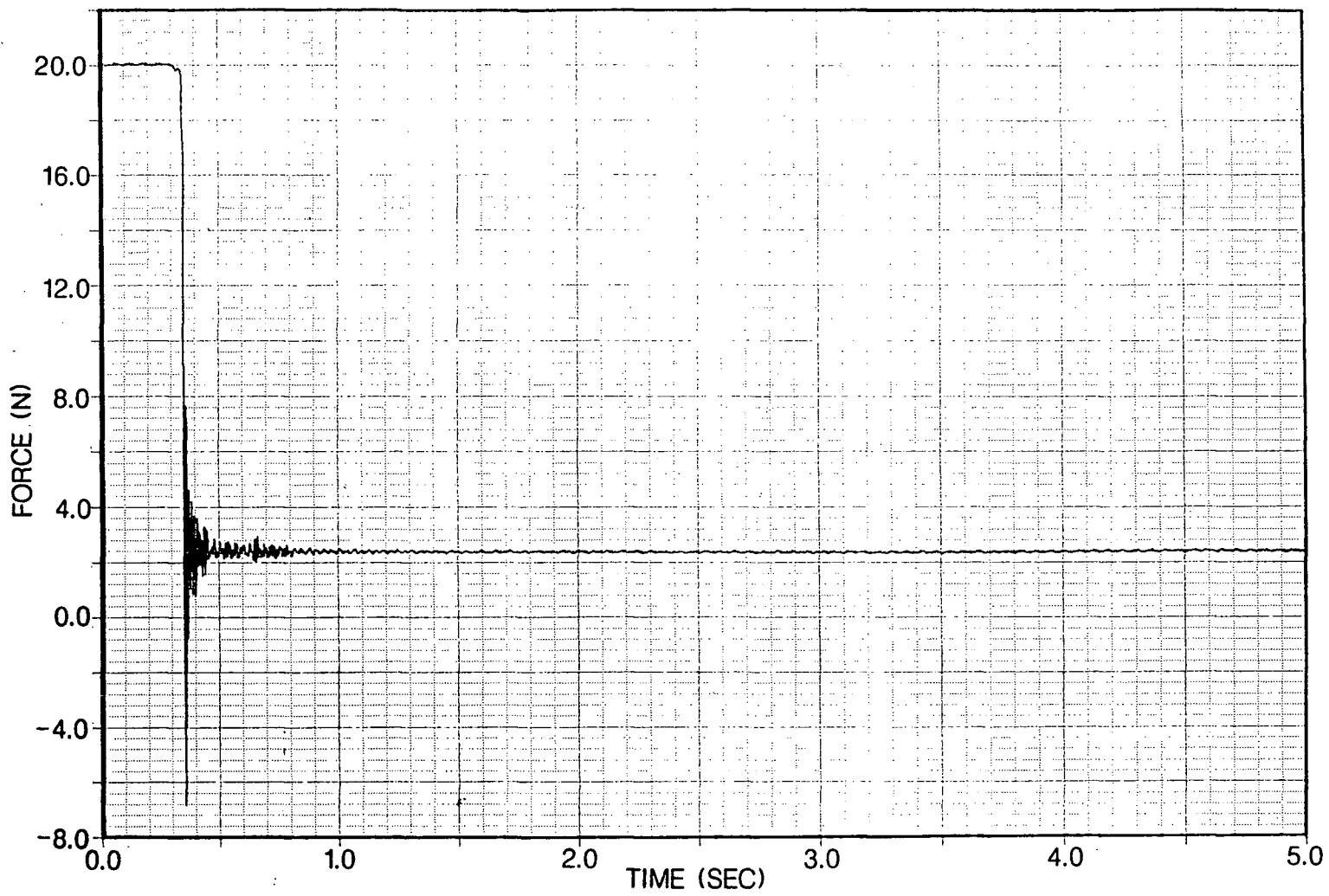


Figure 3.6: Initial condition test response of transducer 4-Y.

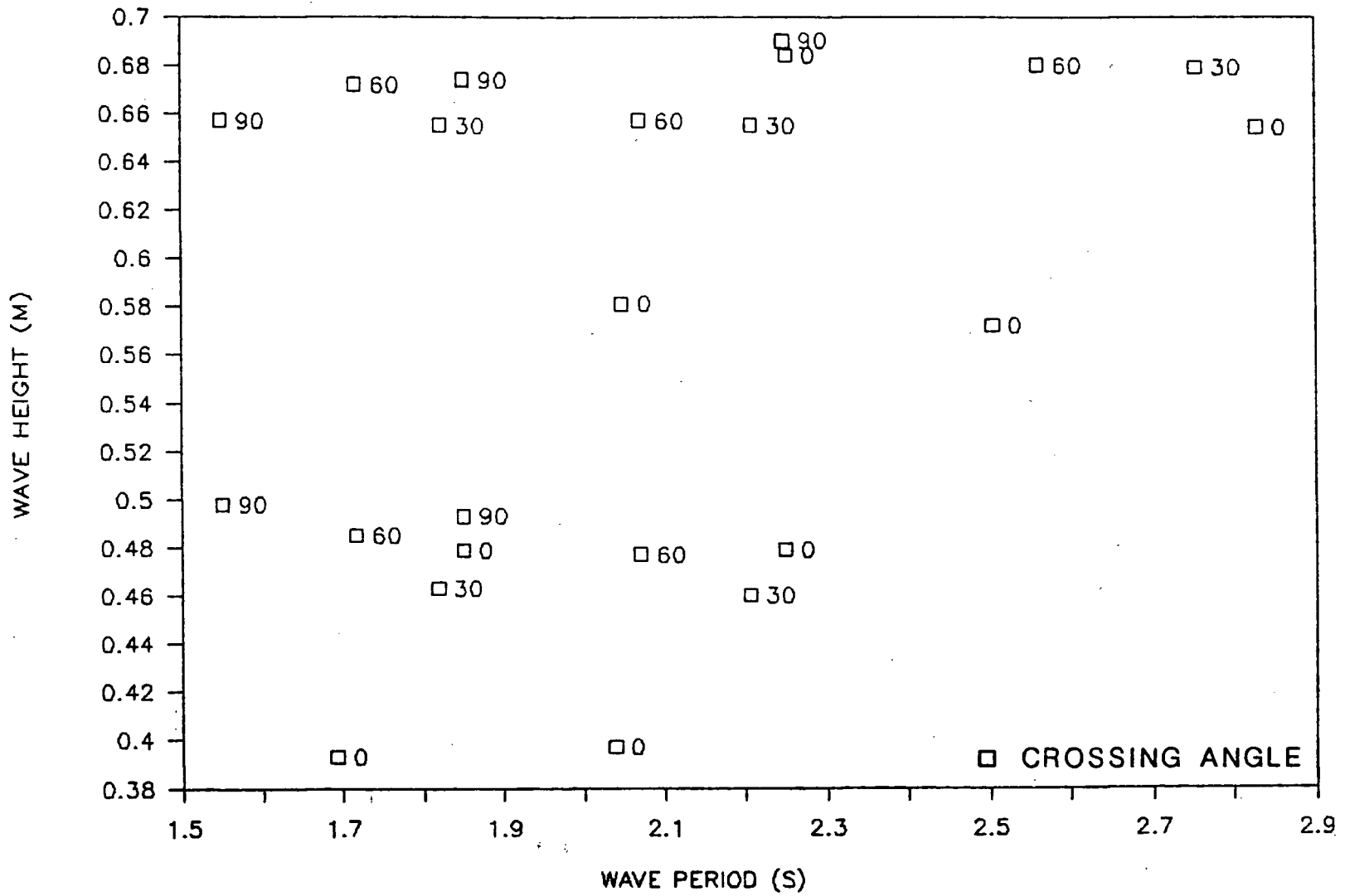
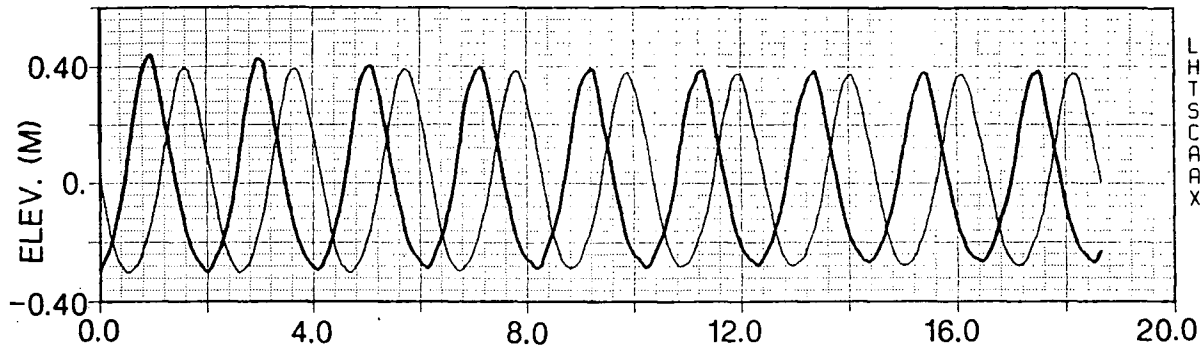
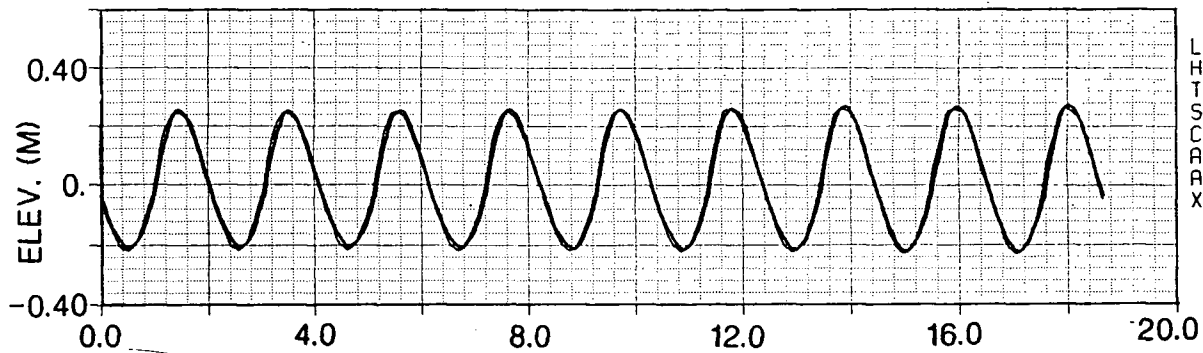


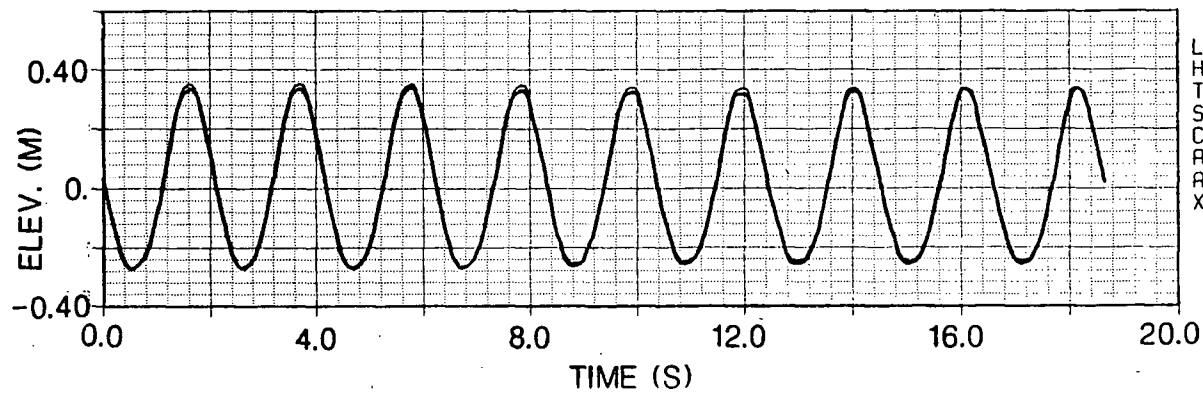
Figure 3.7: Plot of wave characteristics used during phase 2.



| | PROBE 15 | PROBE 18 |
|-------|----------|----------|
| LINE | | |
| HZAVE | = .6727 | = .6820 |
| TZAVE | = 2.0717 | = 2.0635 |
| SAVE | = .0871 | = .0889 |
| CFSAV | = .2079 | = .2077 |
| AHAV | = .6071 | = .5491 |
| AVAV | = .5074 | = .5410 |
| X-COR | = | = .9619 |



| | PROBE 16 | PROBE 17 |
|-------|----------|----------|
| LINE | | |
| HZAVE | = .4749 | = .4713 |
| TZAVE | = 2.0711 | = 2.0728 |
| SAVE | = .0615 | = .0609 |
| CFSAV | = .1659 | = .1637 |
| AHAV | = .5690 | = .5887 |
| AVAV | = .4103 | = .4359 |
| X-COR | = | = .9973 |



| | PROBE 7 | PROBE 9 |
|-------|----------|----------|
| LINE | | |
| HZAVE | = .6016 | = .5927 |
| TZAVE | = 2.0709 | = 2.0709 |
| SAVE | = .0779 | = .0768 |
| CFSAV | = .1792 | = .1716 |
| AHAV | = .5960 | = .5877 |
| AVAV | = .5177 | = .5183 |
| X-COR | = | = .9993 |

Figure 4.1: Wave time series and characteristics measured during test MRE2.

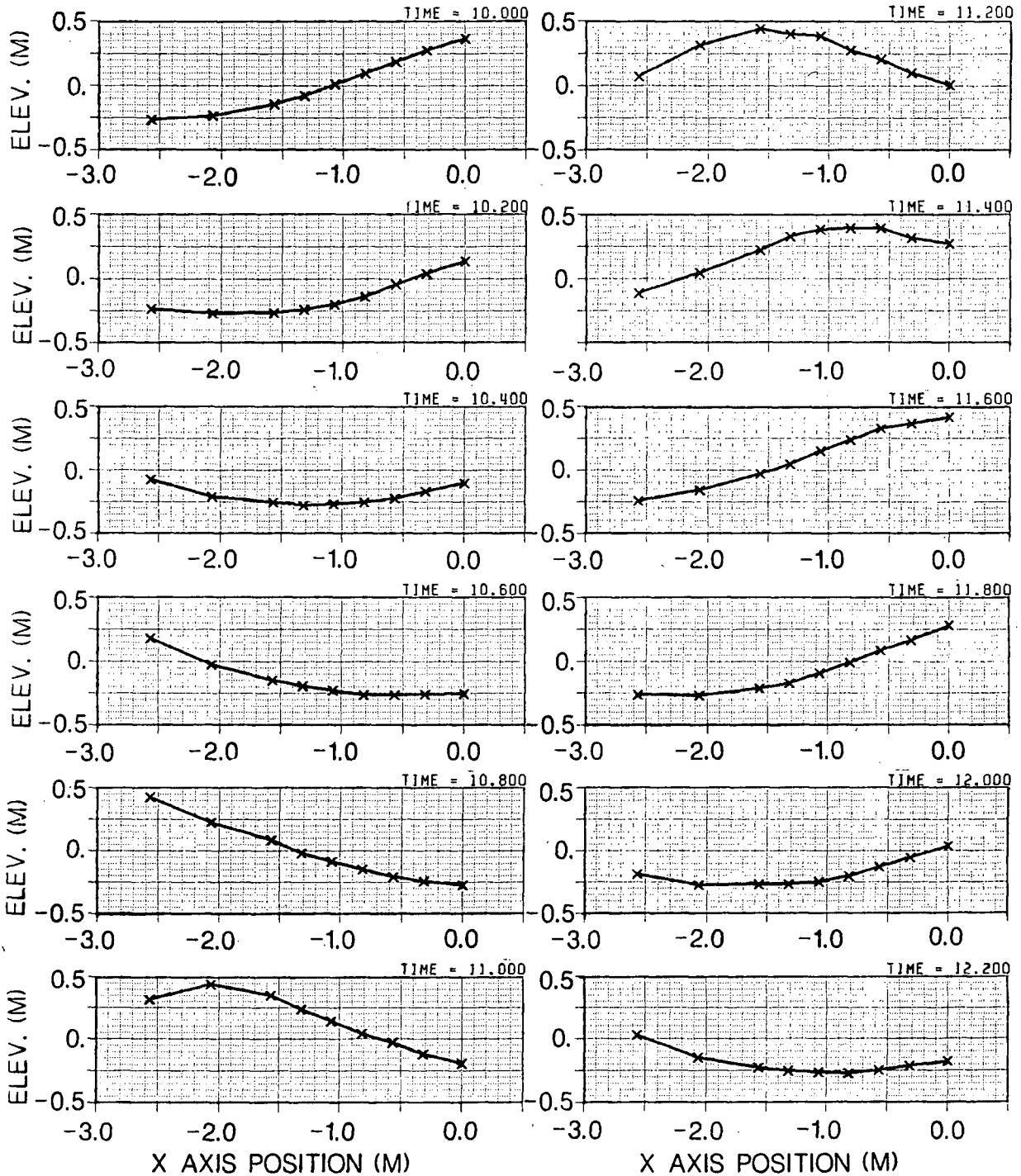


Figure 4.2: In-line wave profile snapshots from test MB32.

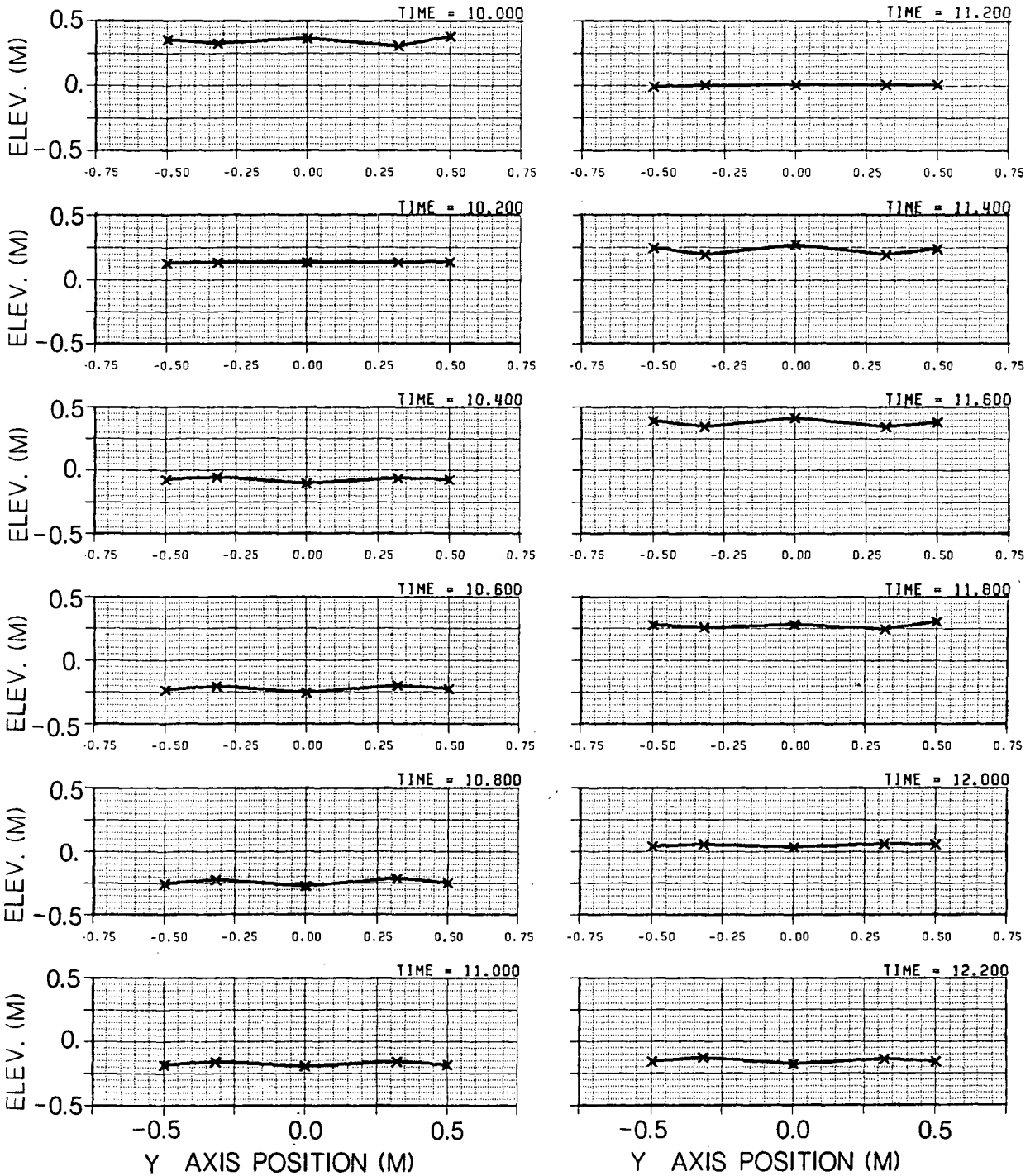


Figure 4.3: Transverse wave profile snapshots from test MB32.

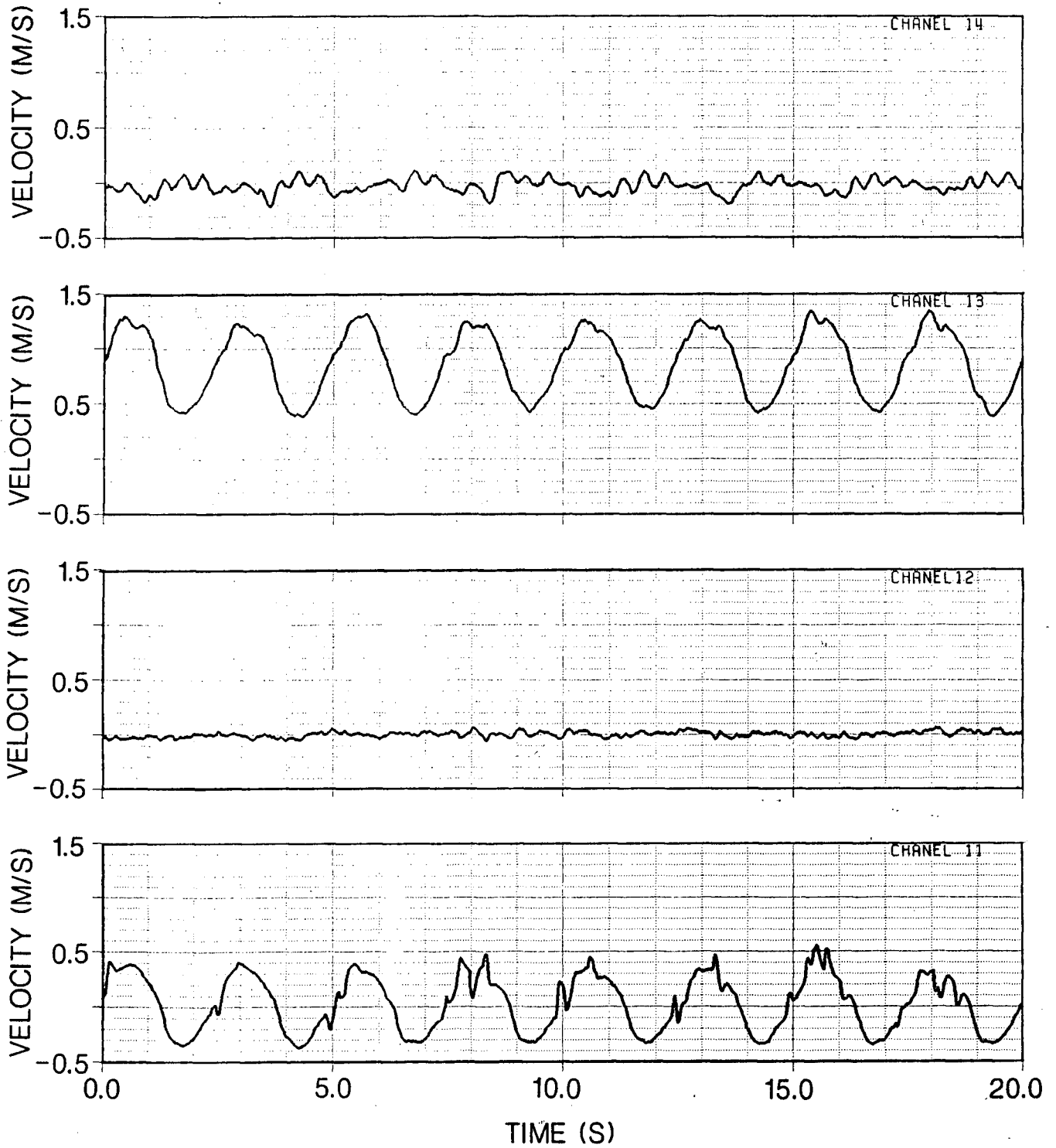


Figure 4.4: Raw current meter data from test SN53.

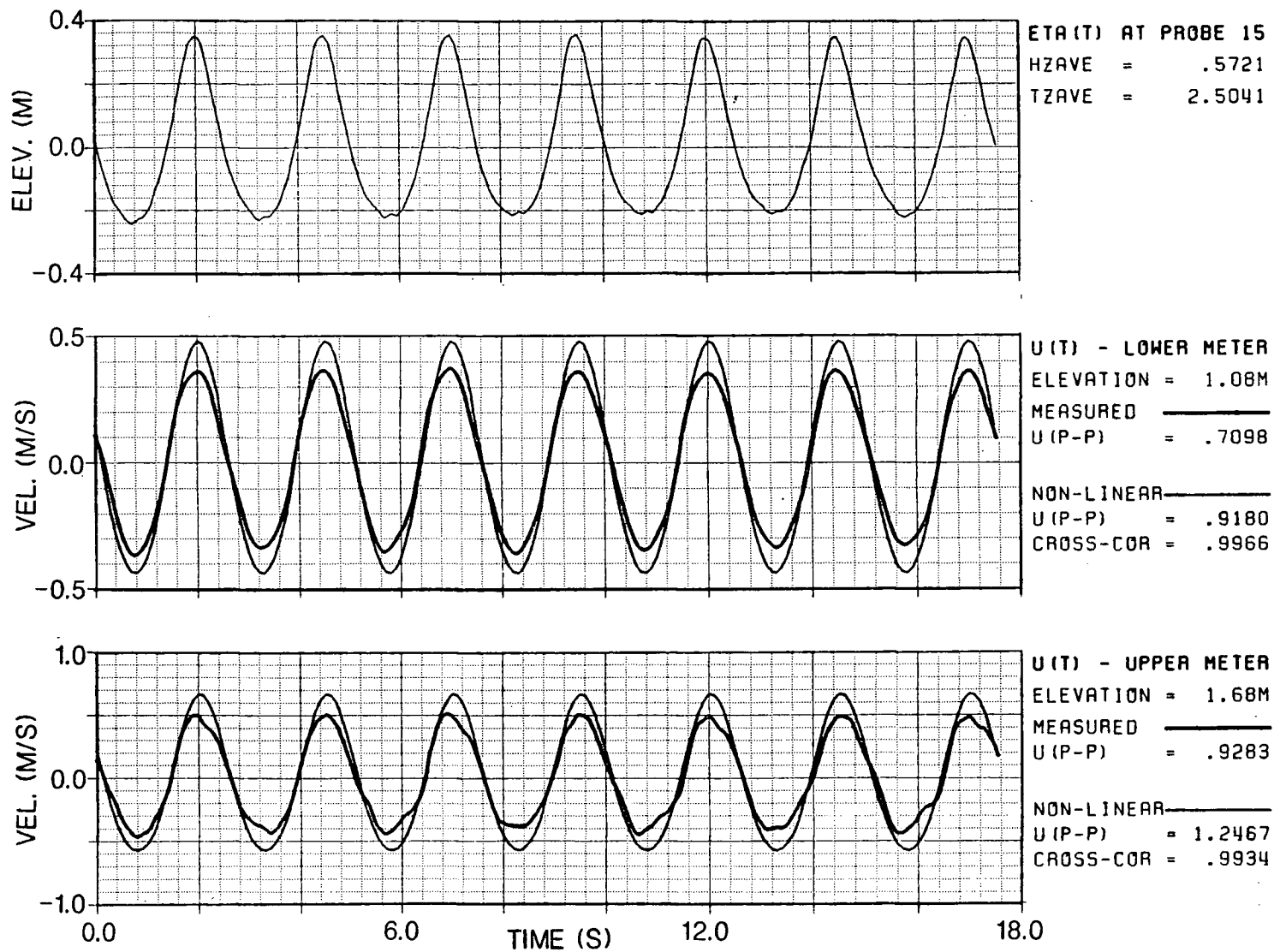


Figure 4.5: Measured and predicted current characteristics and time series from test MN53.

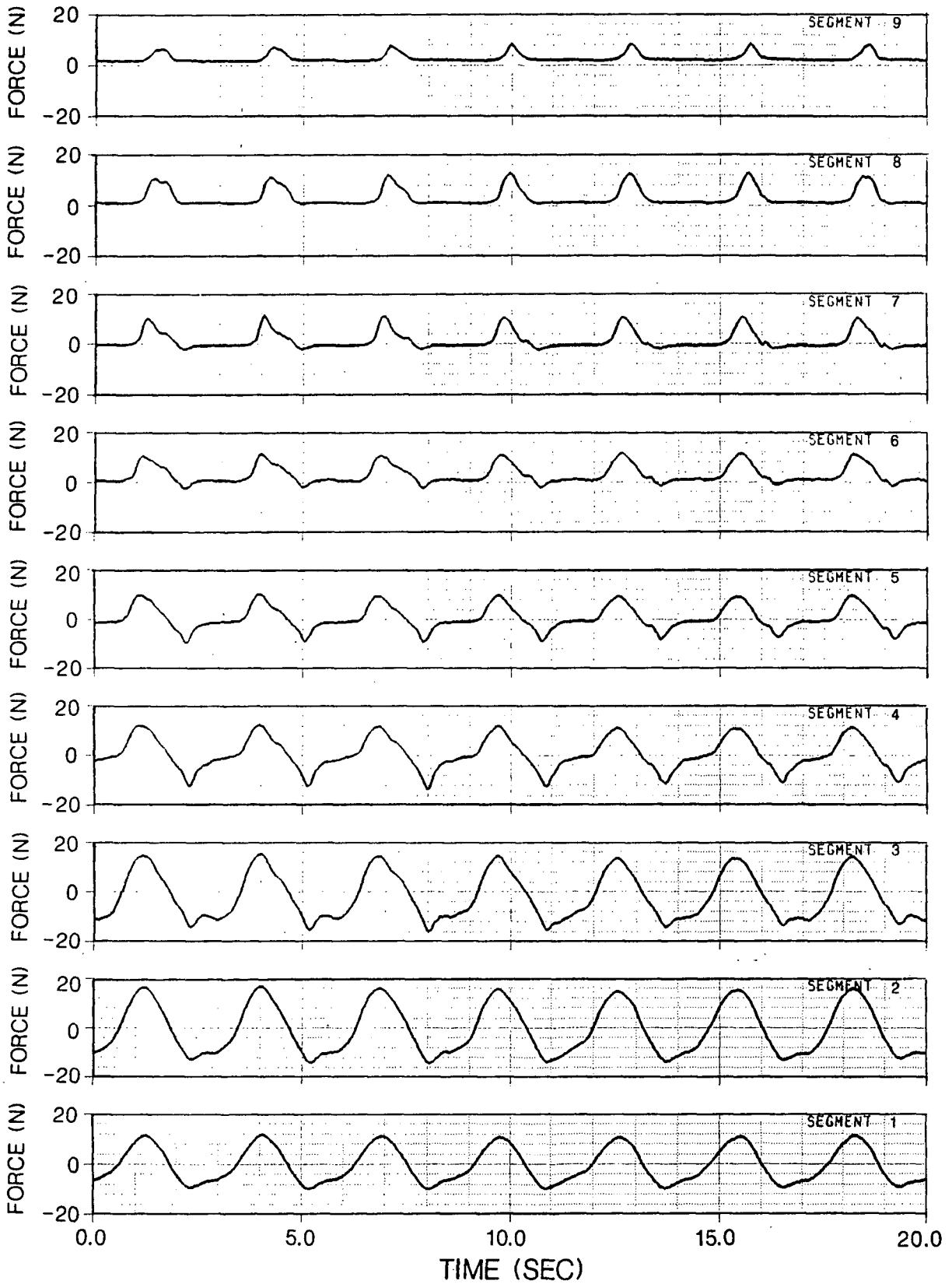


Figure 4.6: Raw X axis force data from test SN64.

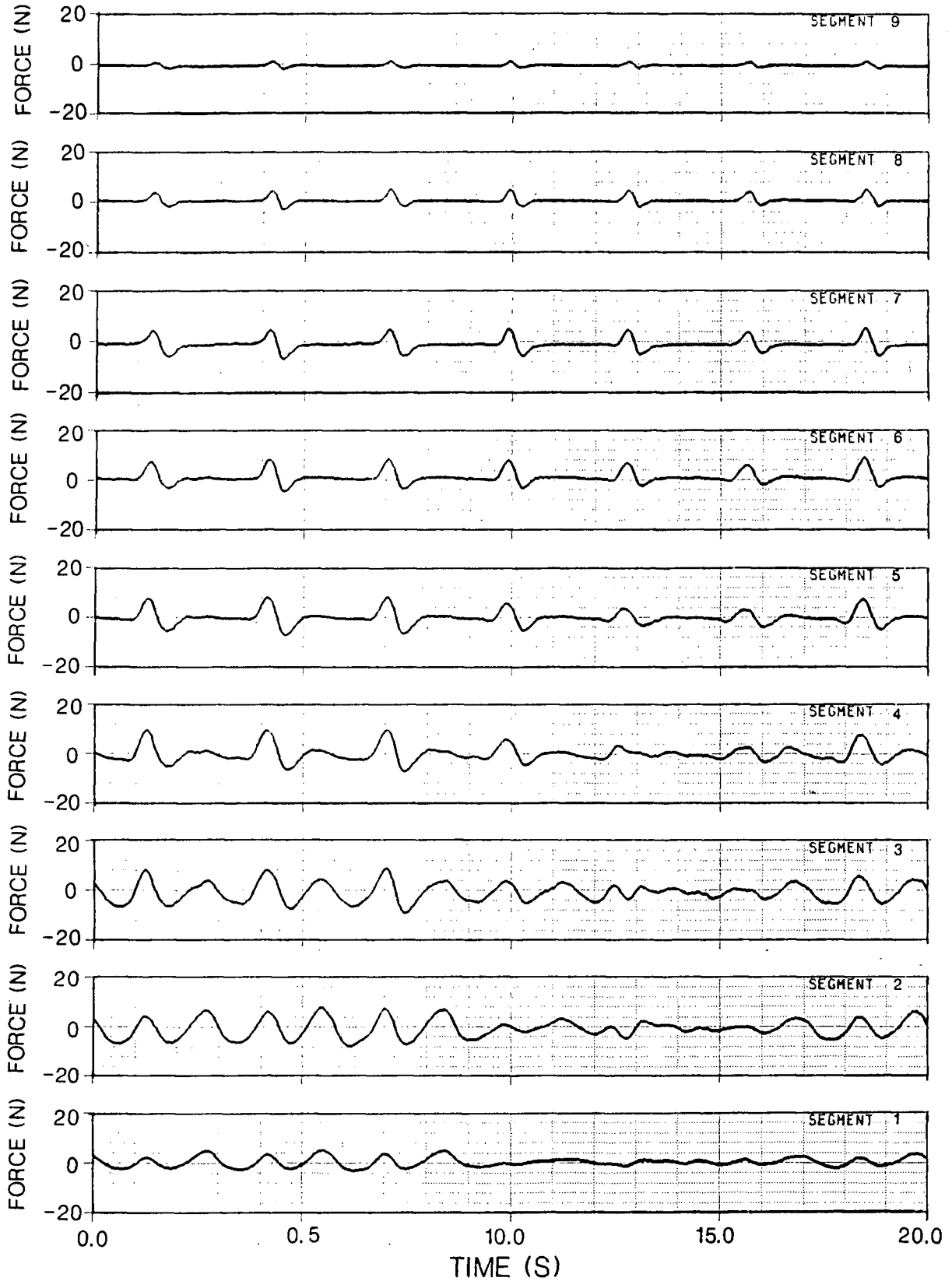


Figure 4.7: Raw Y axis force data from test SN64.

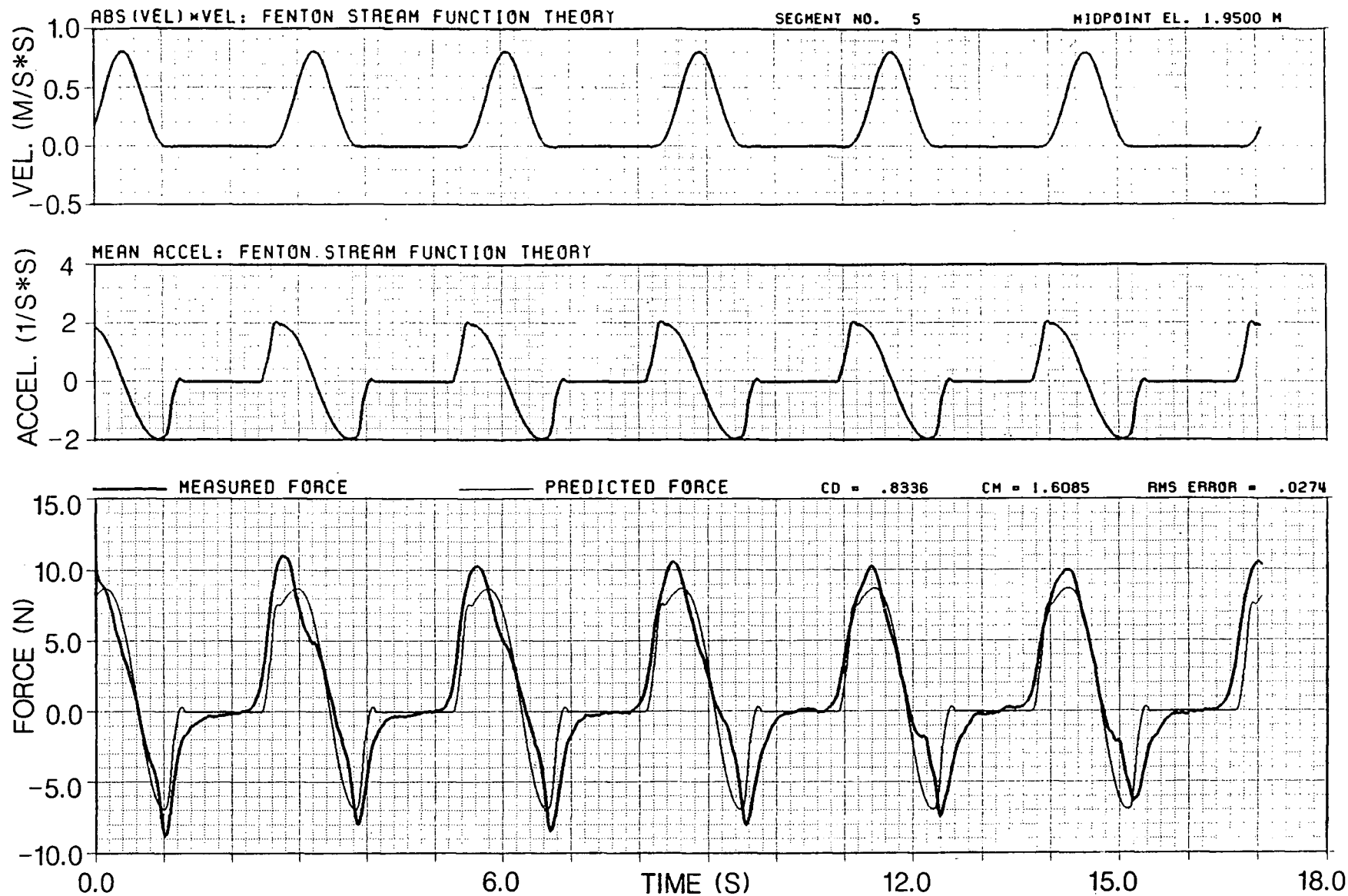


Figure 4.8: Kinematic and force time series used to obtain force coefficients from segment 5 during test SN64.

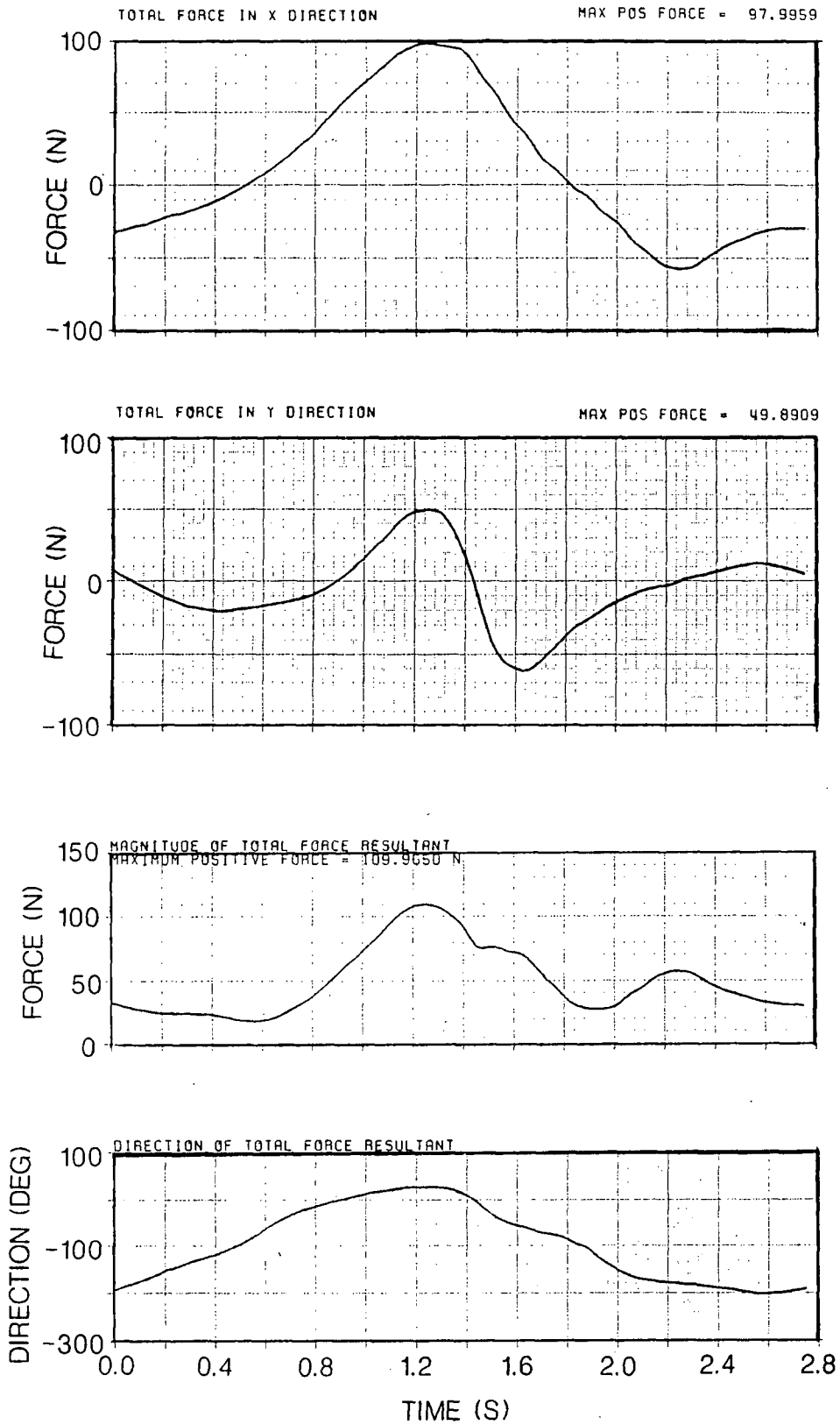


Figure 4.9: Total X, Y and resultant force time series from test SC17.

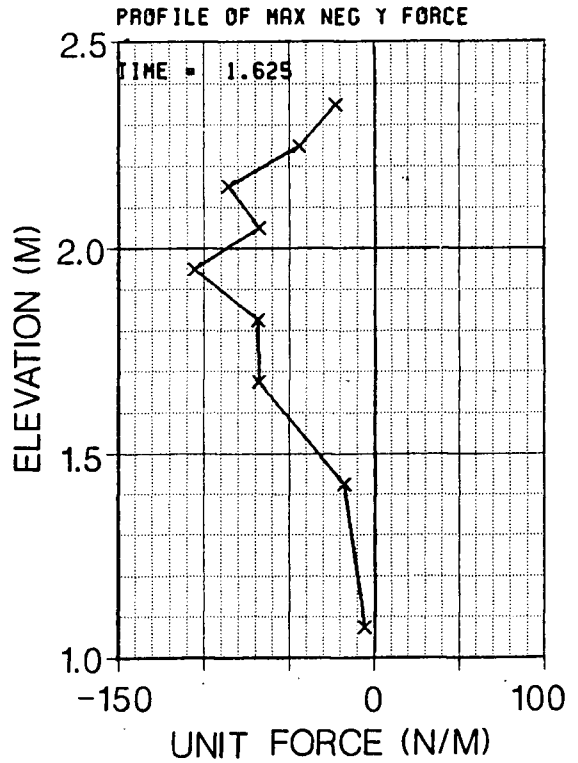
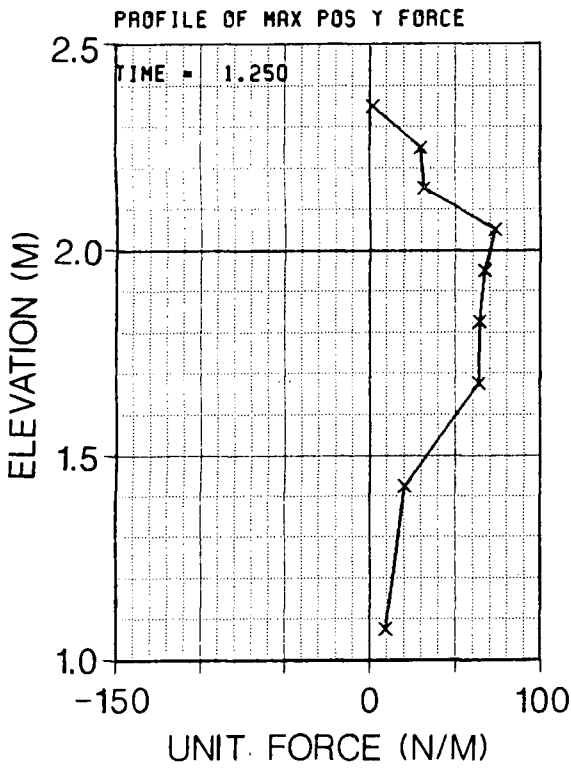
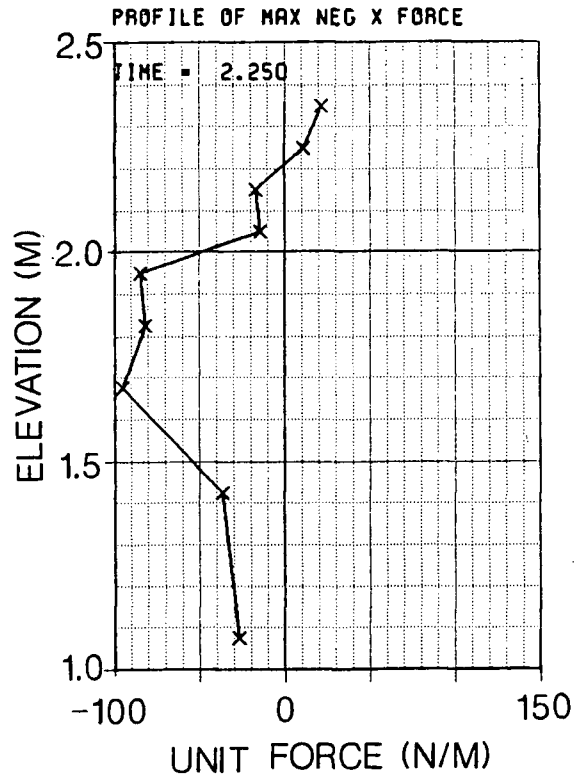
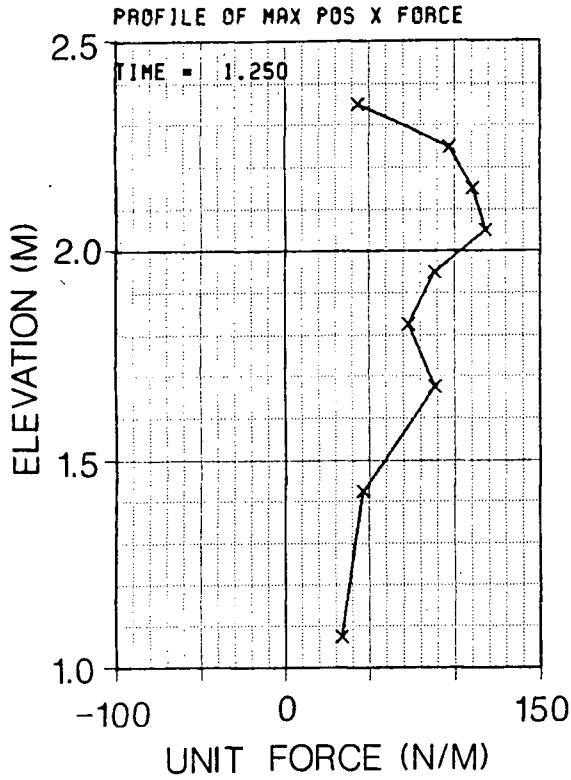


Figure 4.10: In-line and transverse force profiles from test SC17.

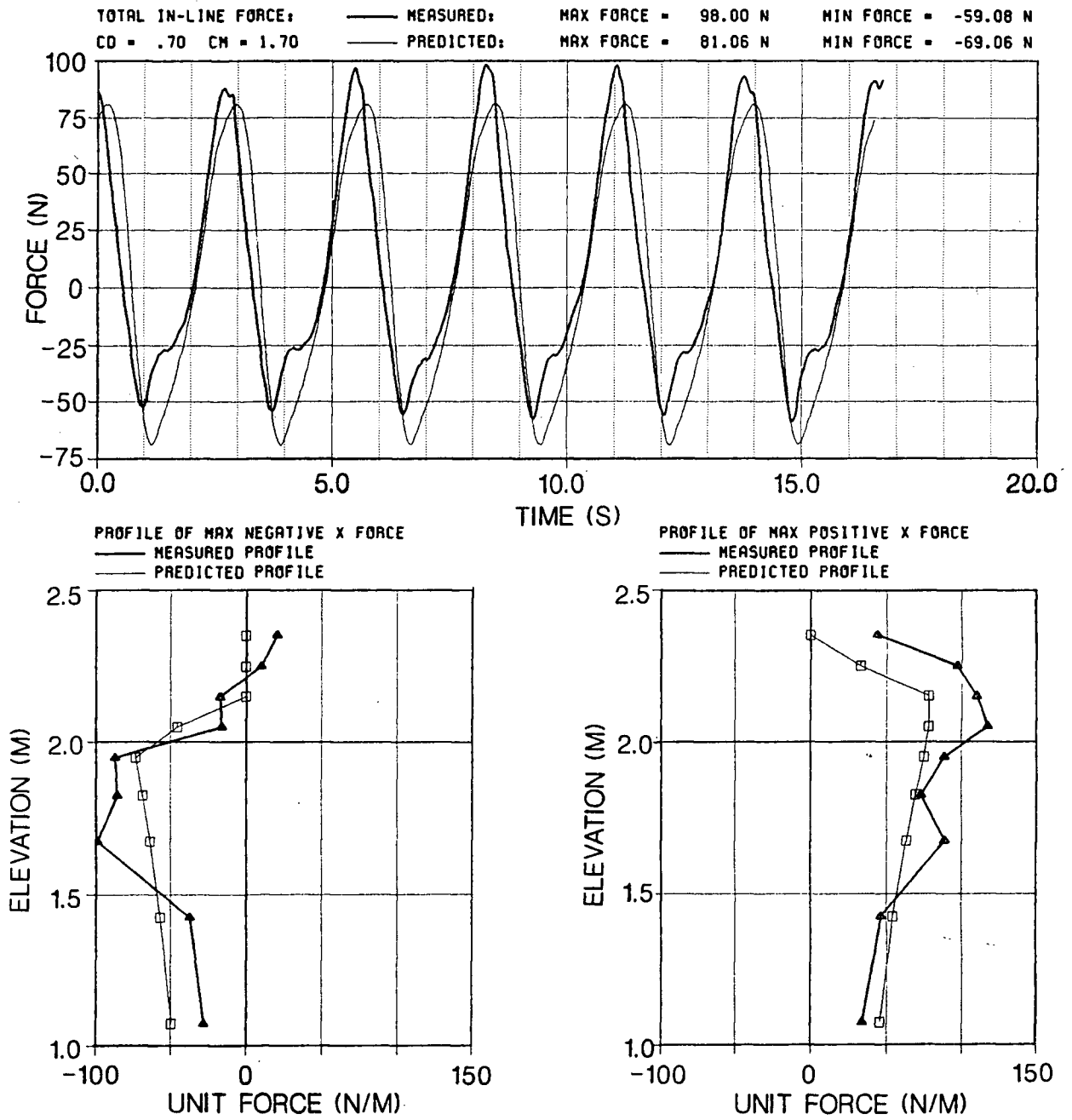


Figure 4.11: Comparison plot of total force and force profiles from test SC17.

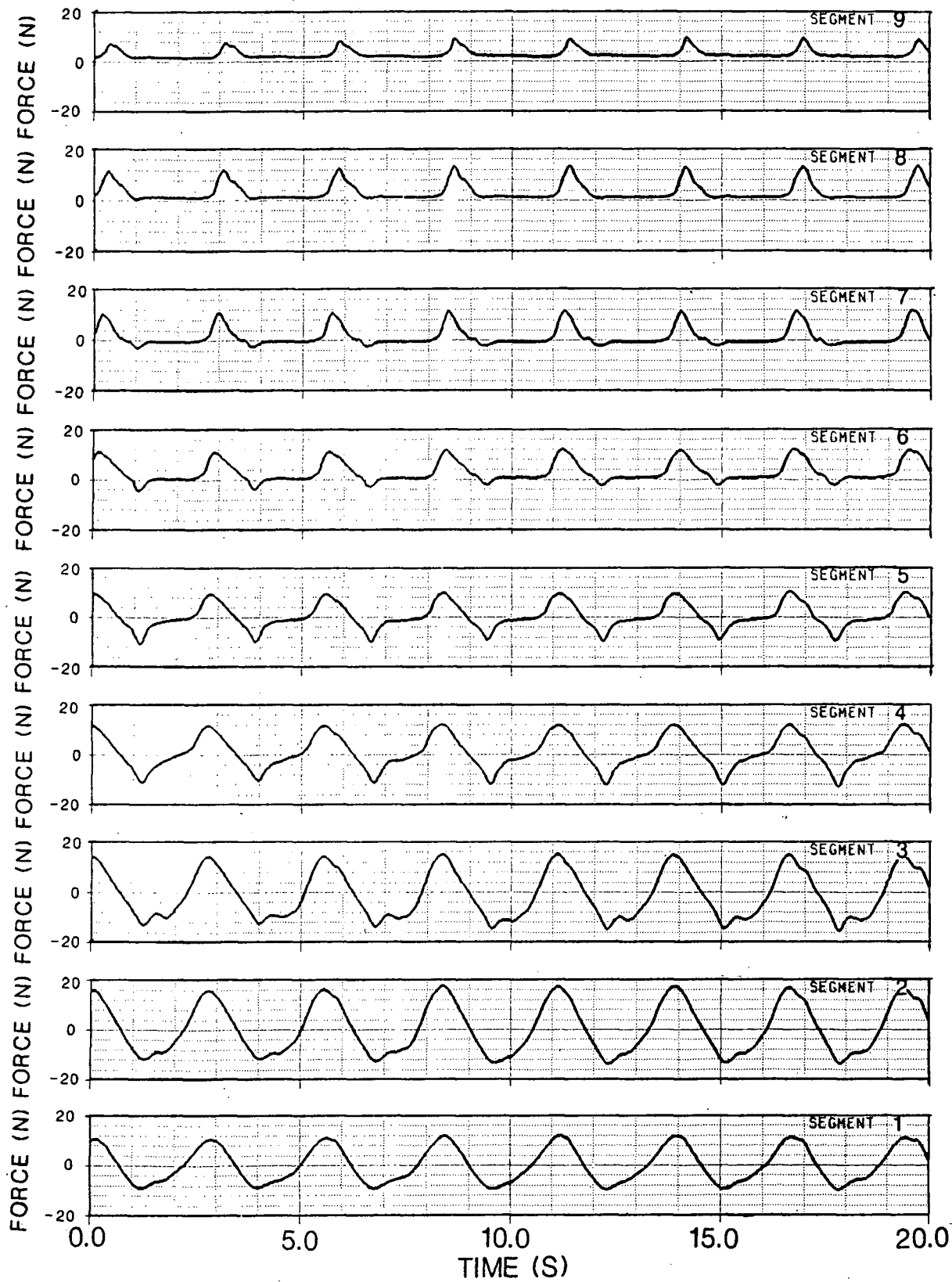


Figure 5.1: Raw X axis force data from test SC17.

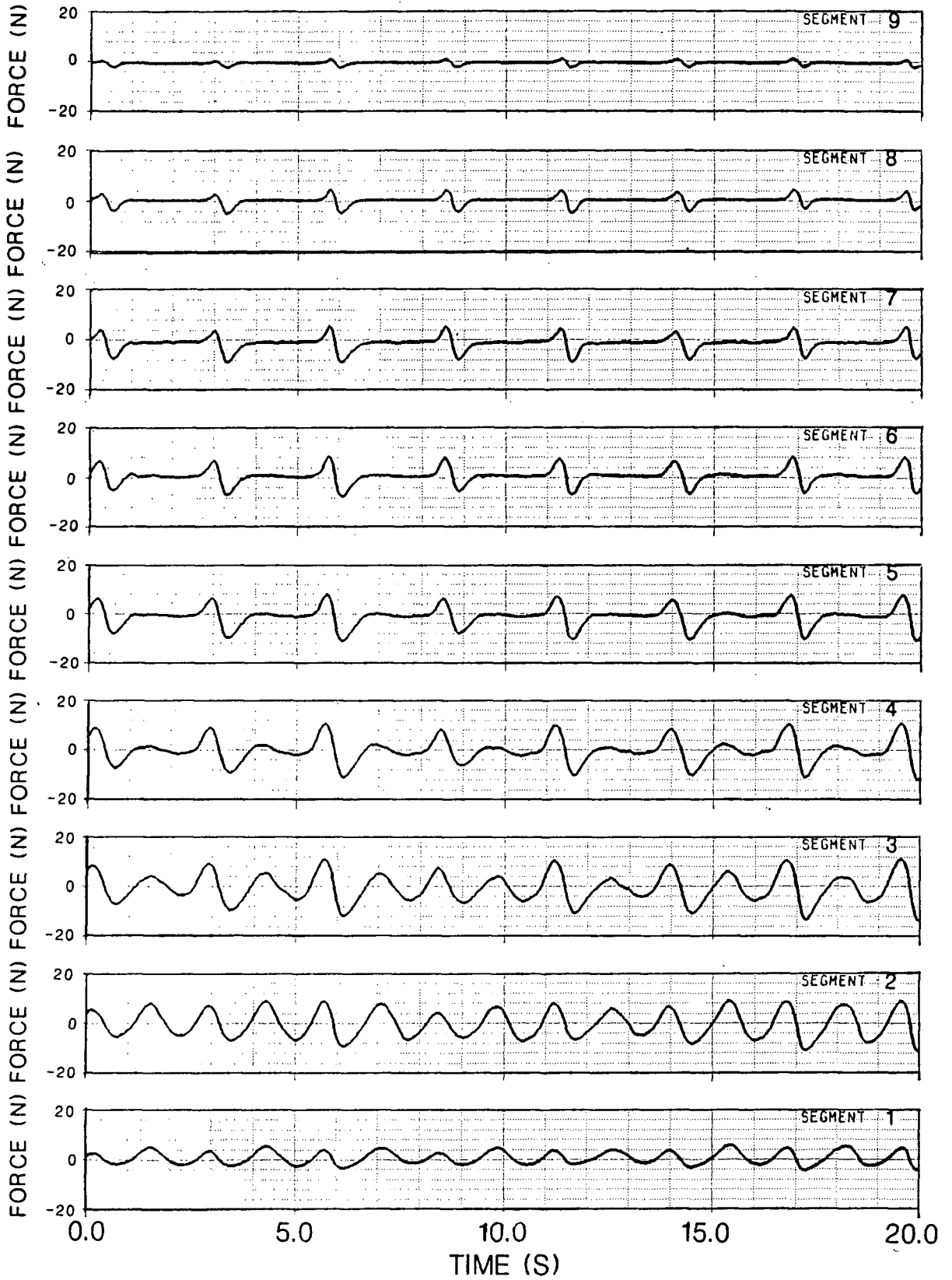


Figure 5.2: Raw Y axis force data from test SC17.

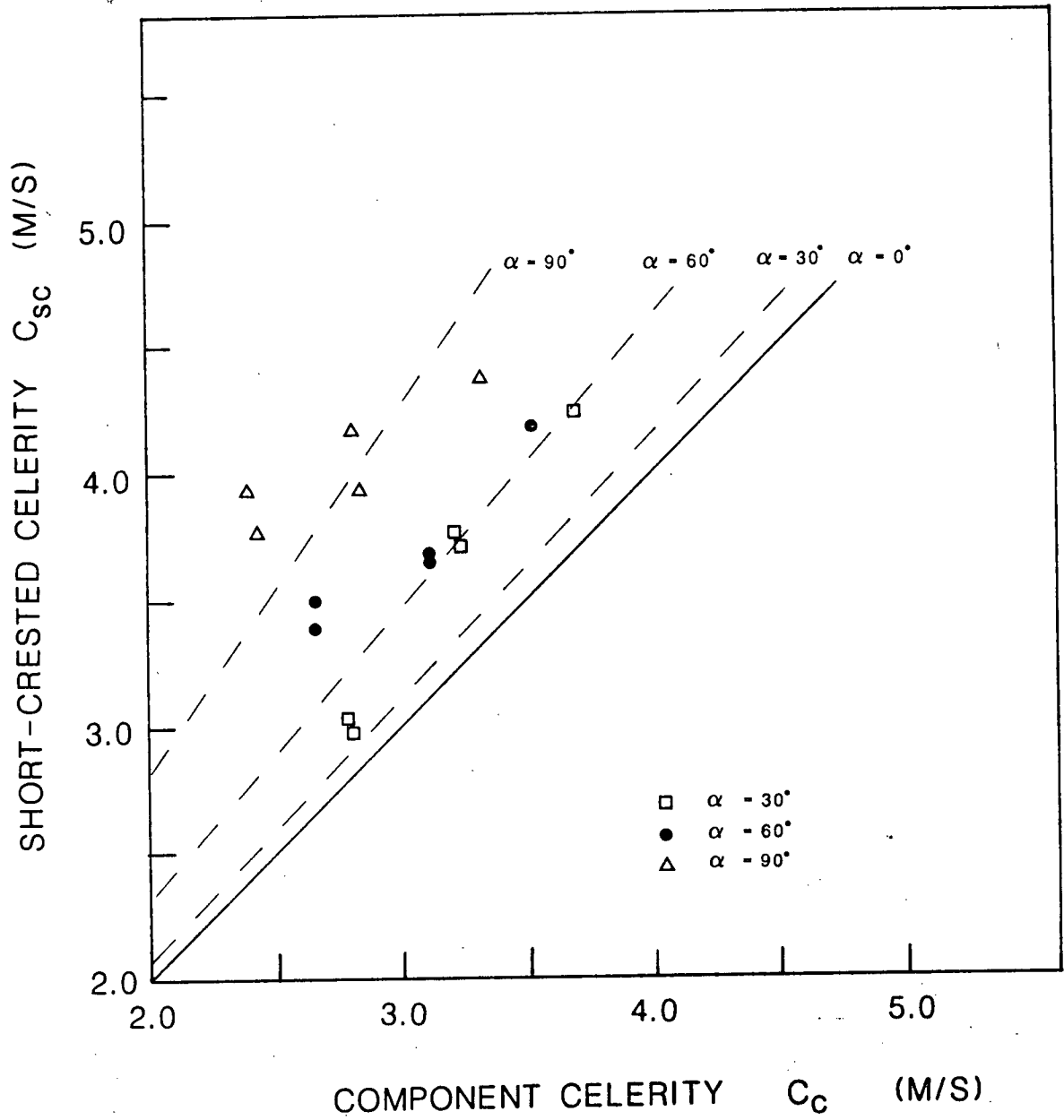


Figure 5.3: Plot of short-crested wave celerity versus component wave celerity.

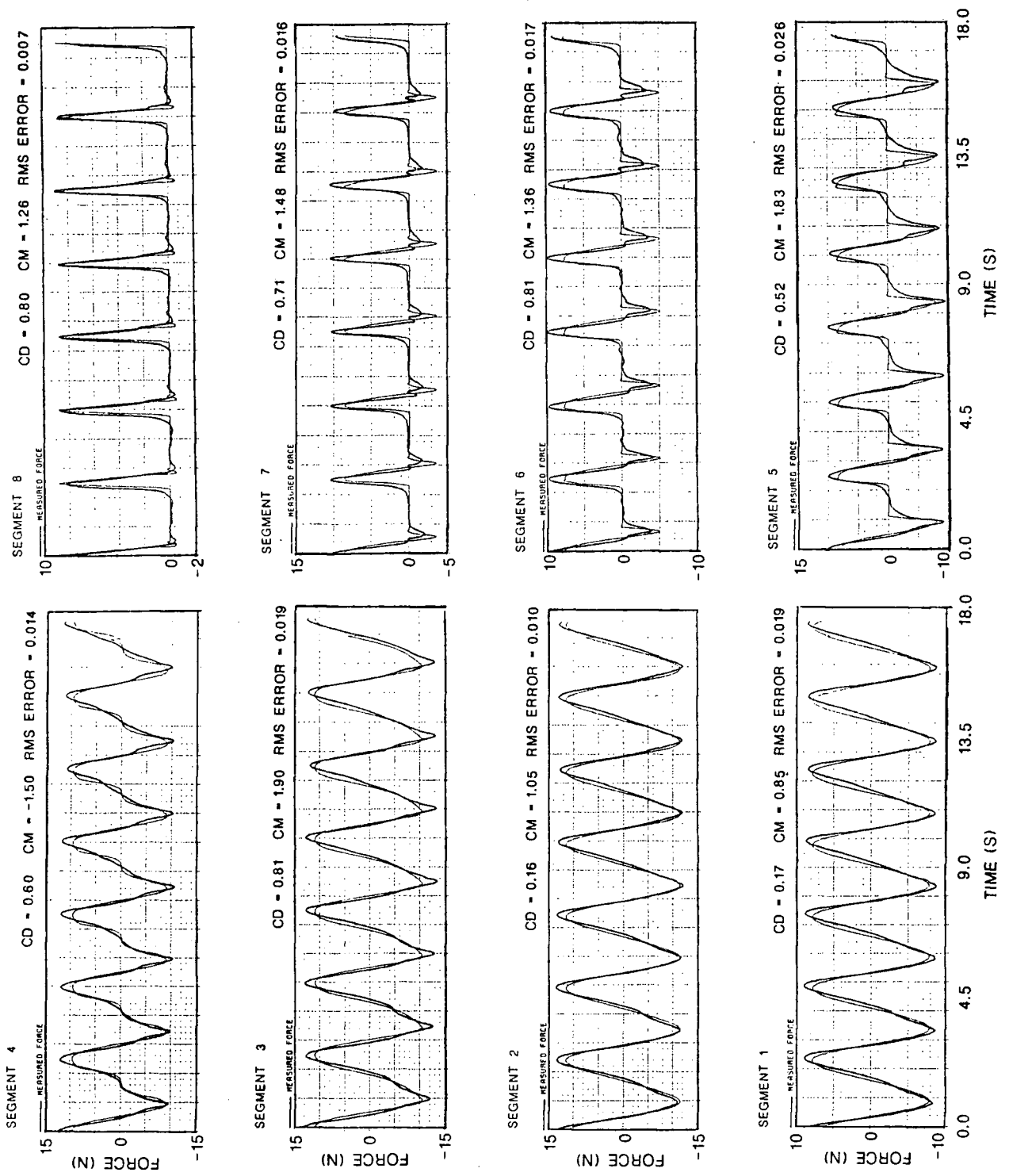


Figure 5.4: Measured and predicted forces for segments 1-8 from test SN53.

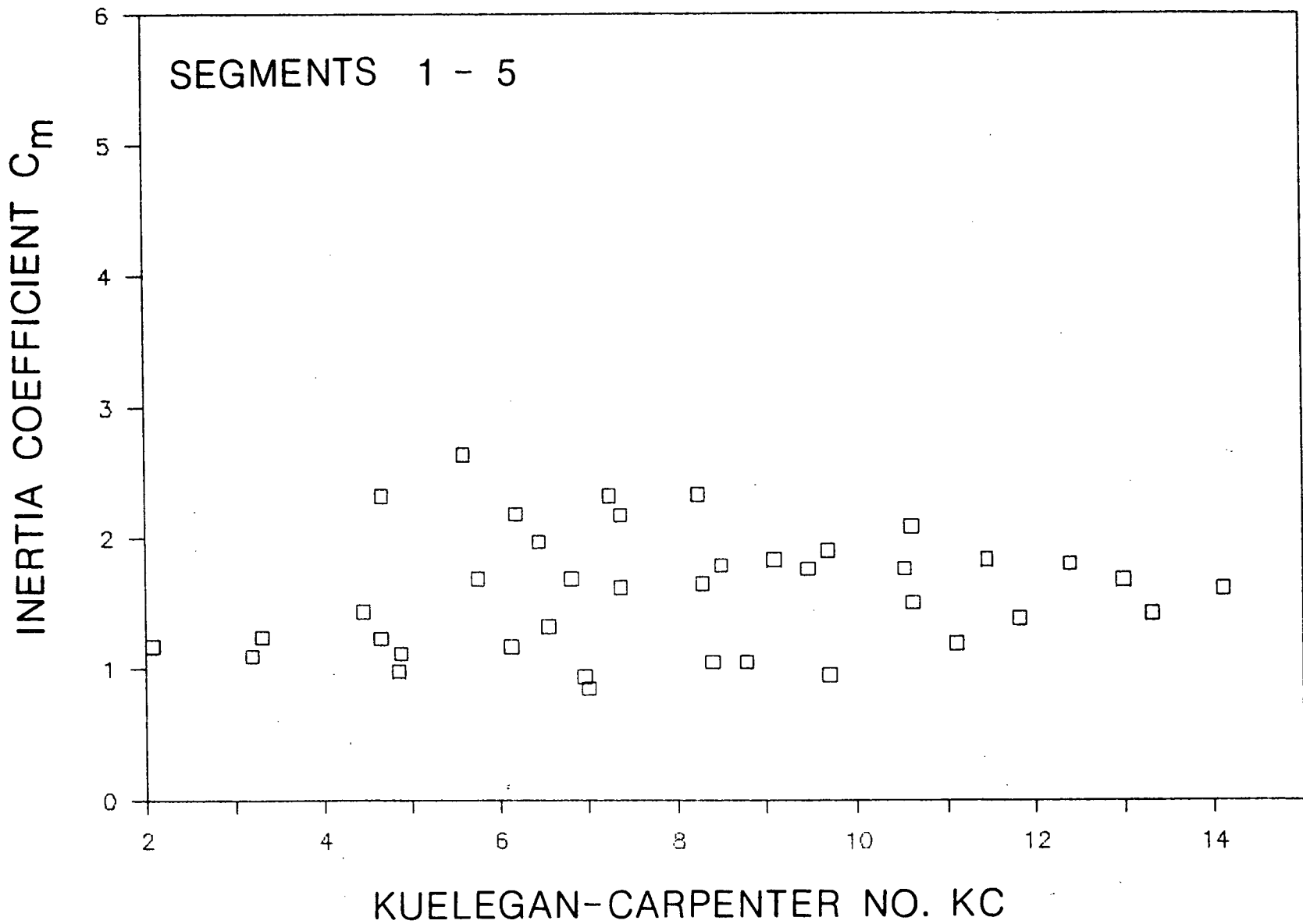


Figure 5.5: Plot of C_m versus KC data from segments 1-5.

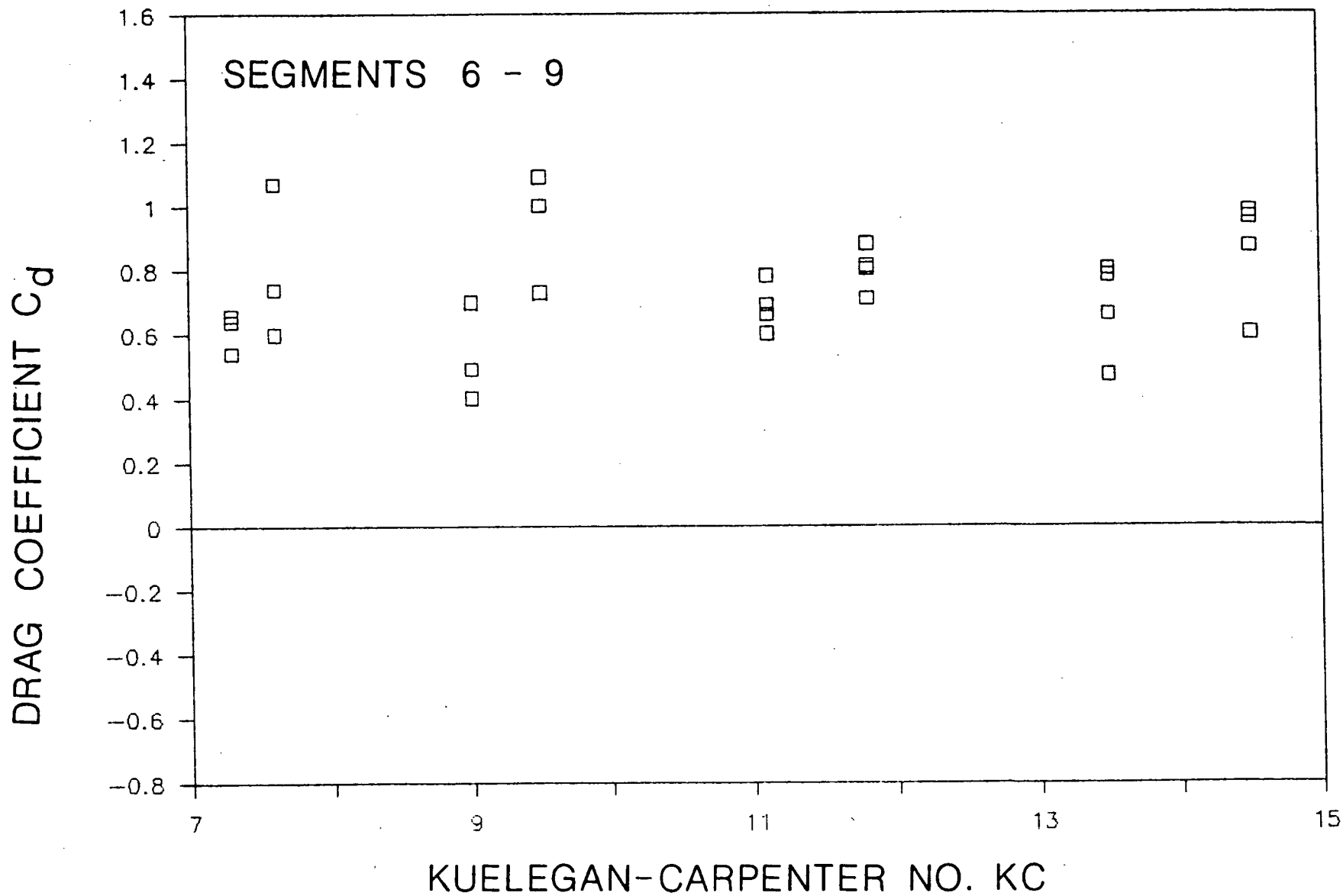


Figure 5.6: Plot of C_d versus KC data from segments 6-9.

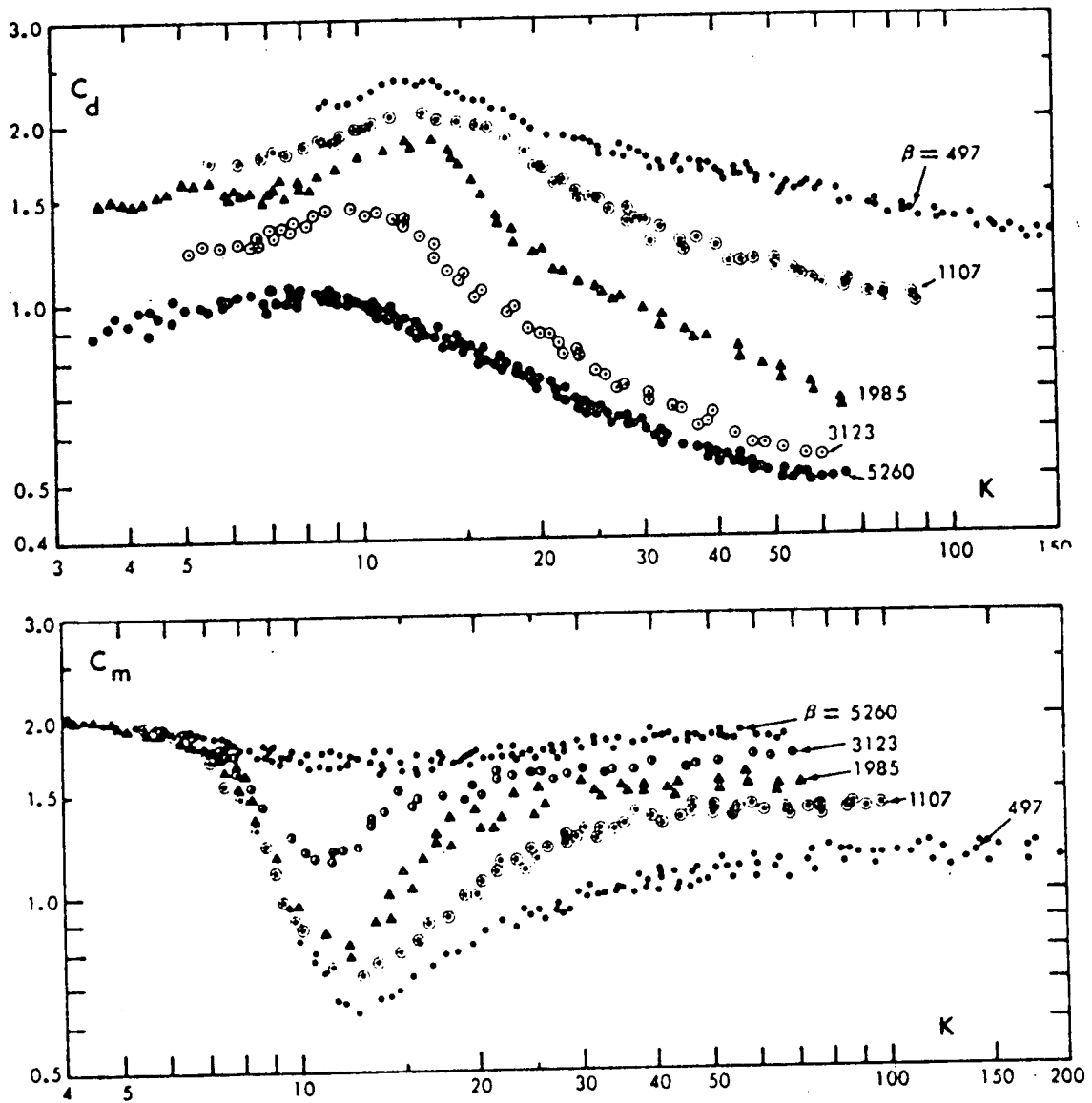


Figure 5.7: Published C_m and C_d values from 'U-tube' tests (from Sarpkaya and Isaacson, 1981).

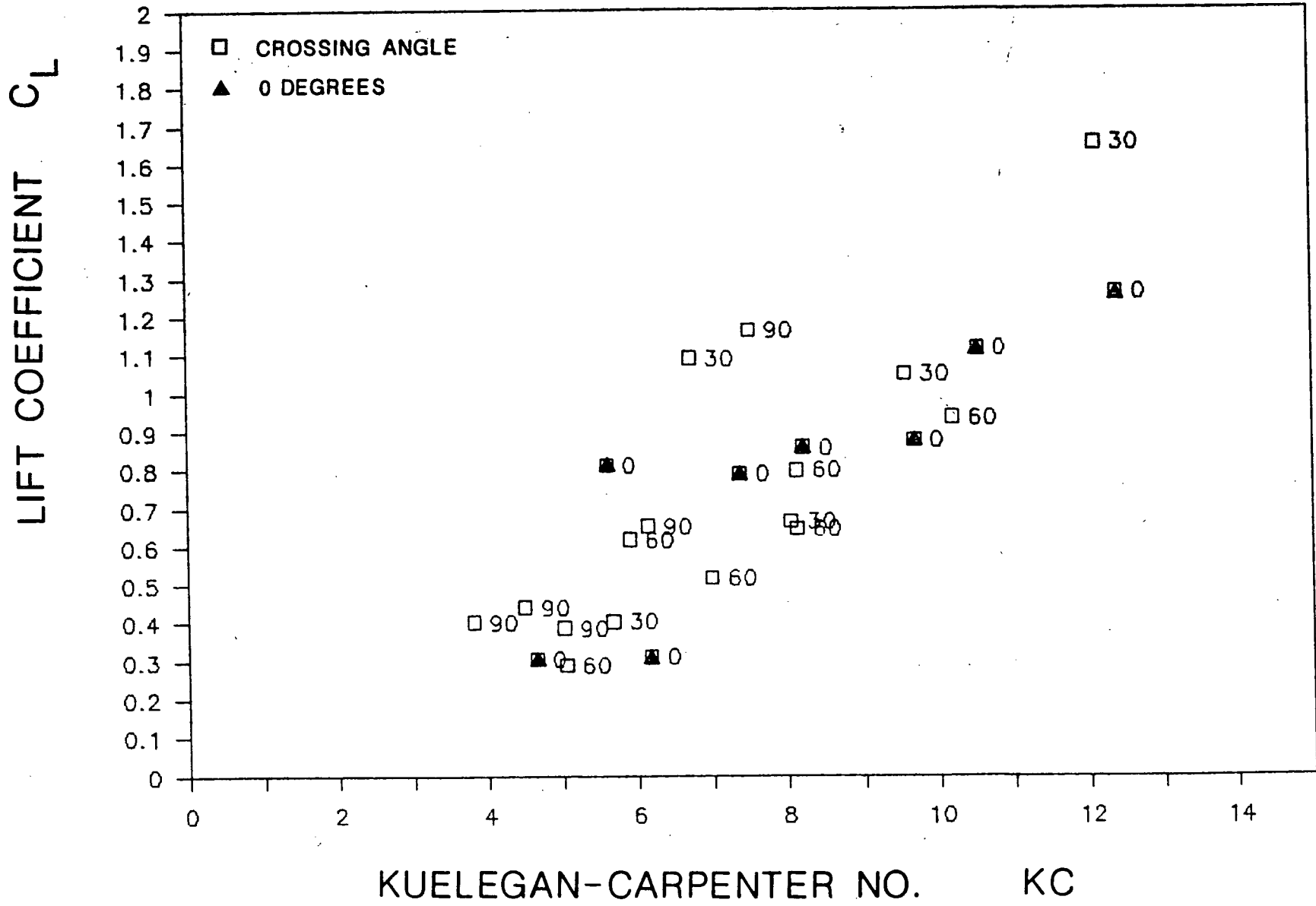


Figure 5.8: Plot of C_L versus KC. Data from segment 3

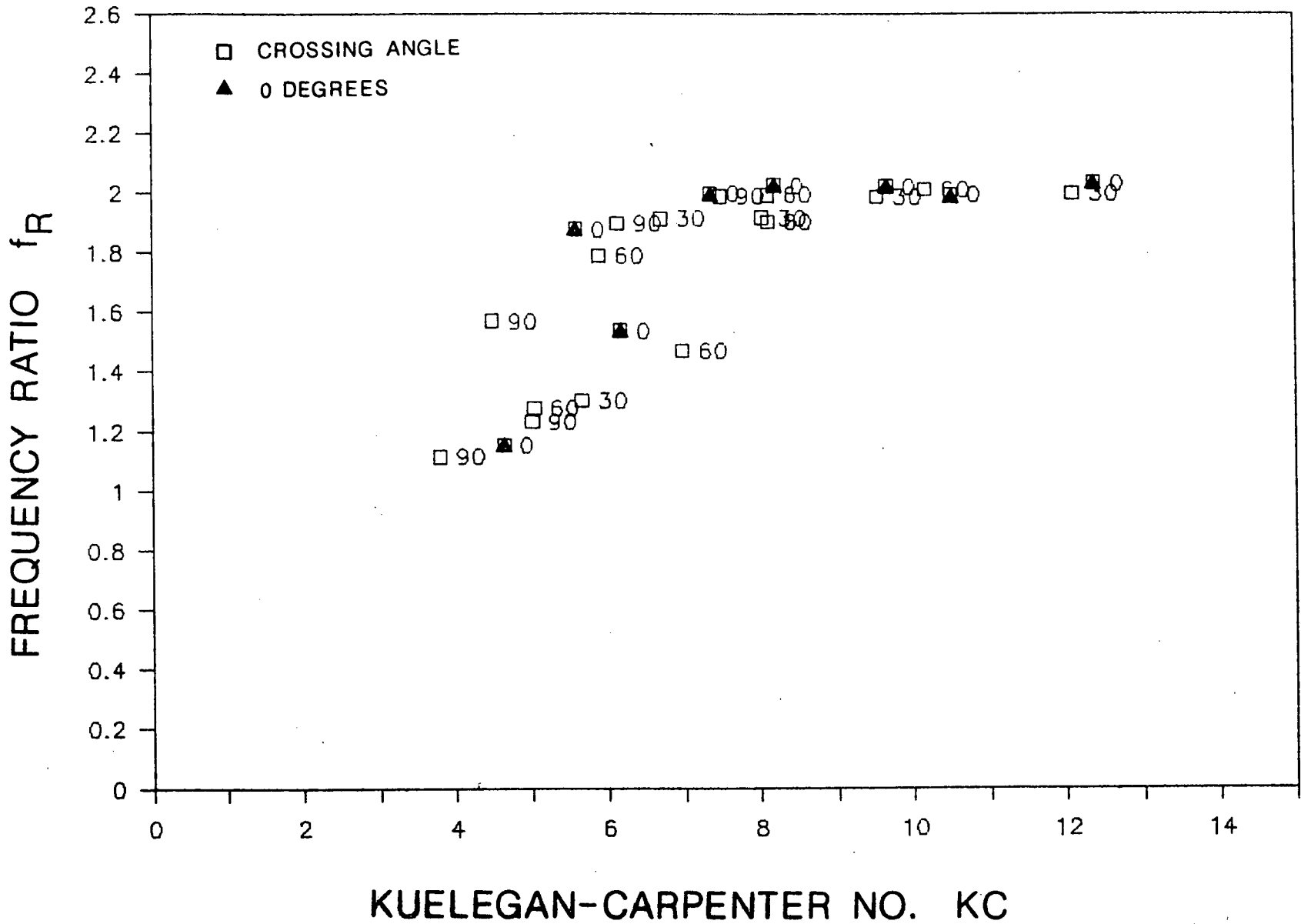


Figure 5.9: Plot of f_R versus KC . Data from segment 3.

X - AXIS

Y - AXIS

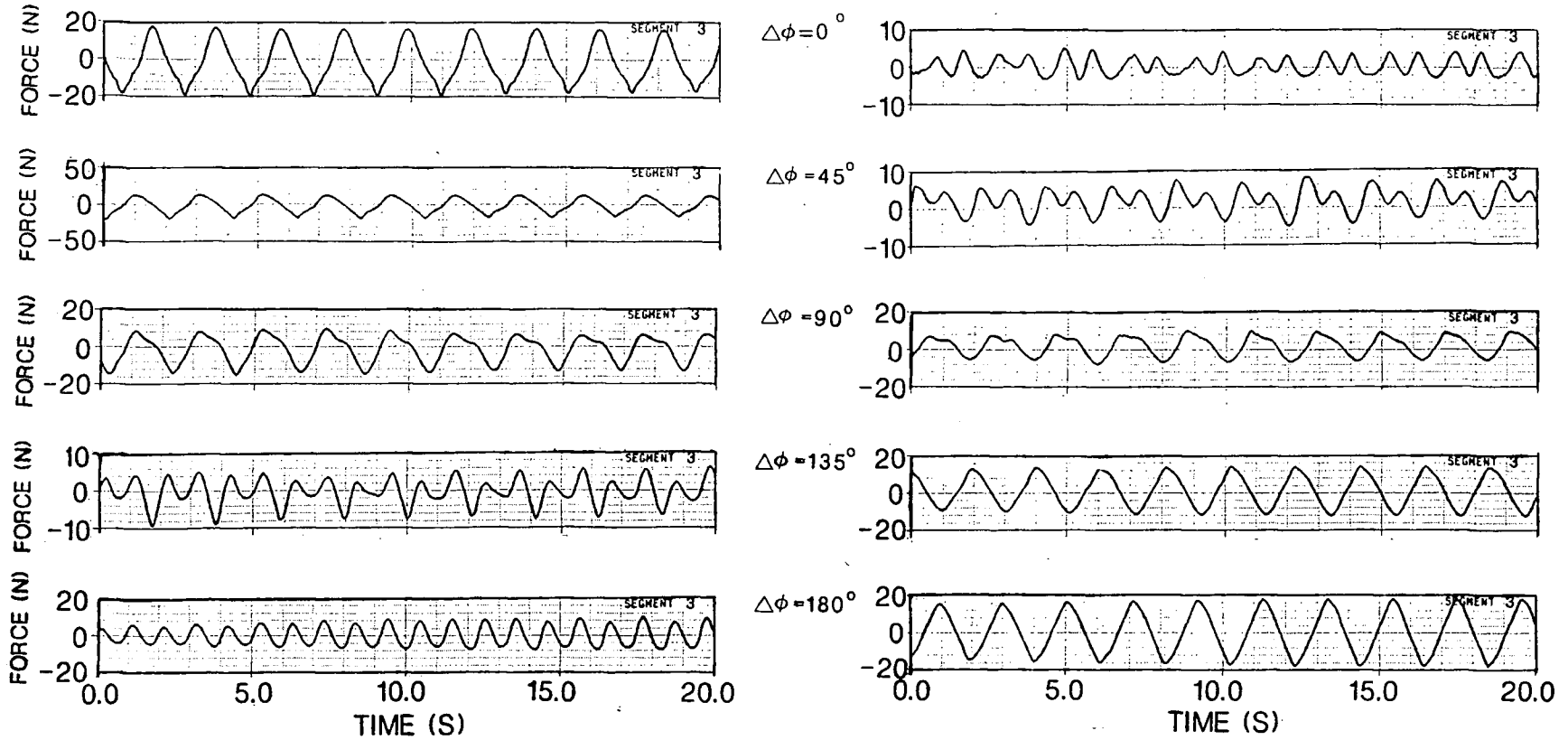


Figure 5.10: X and Y axis force time series responses from segment 3 at 5 locations in the same short-crested flow.

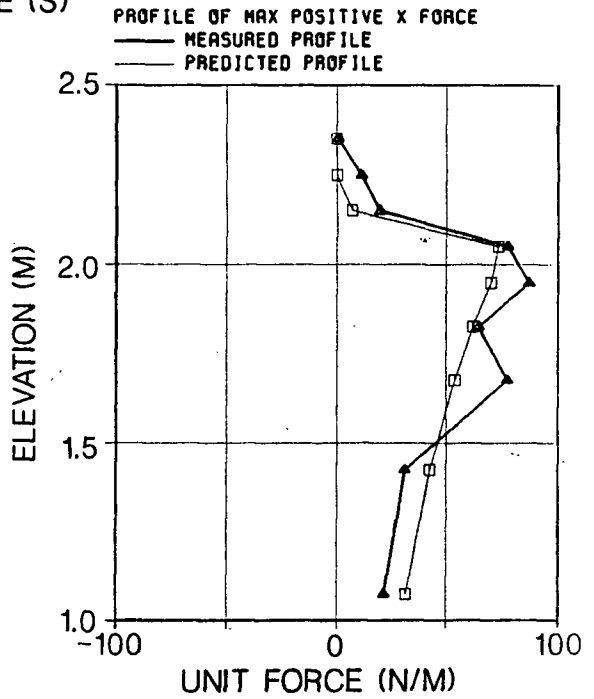
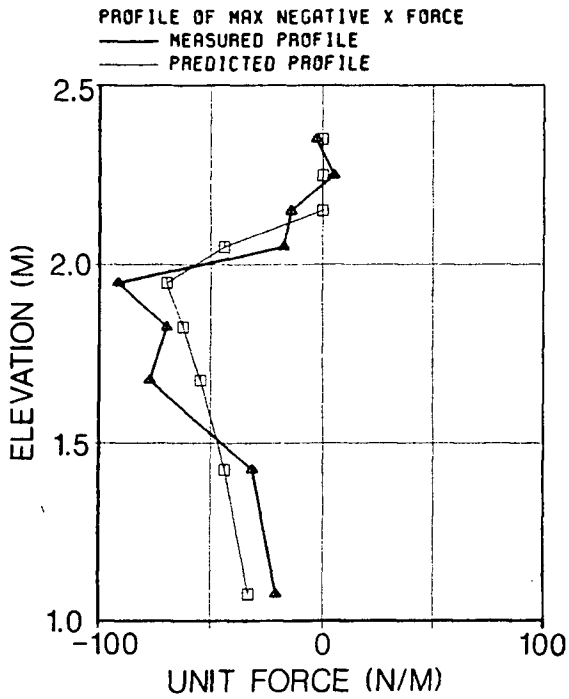
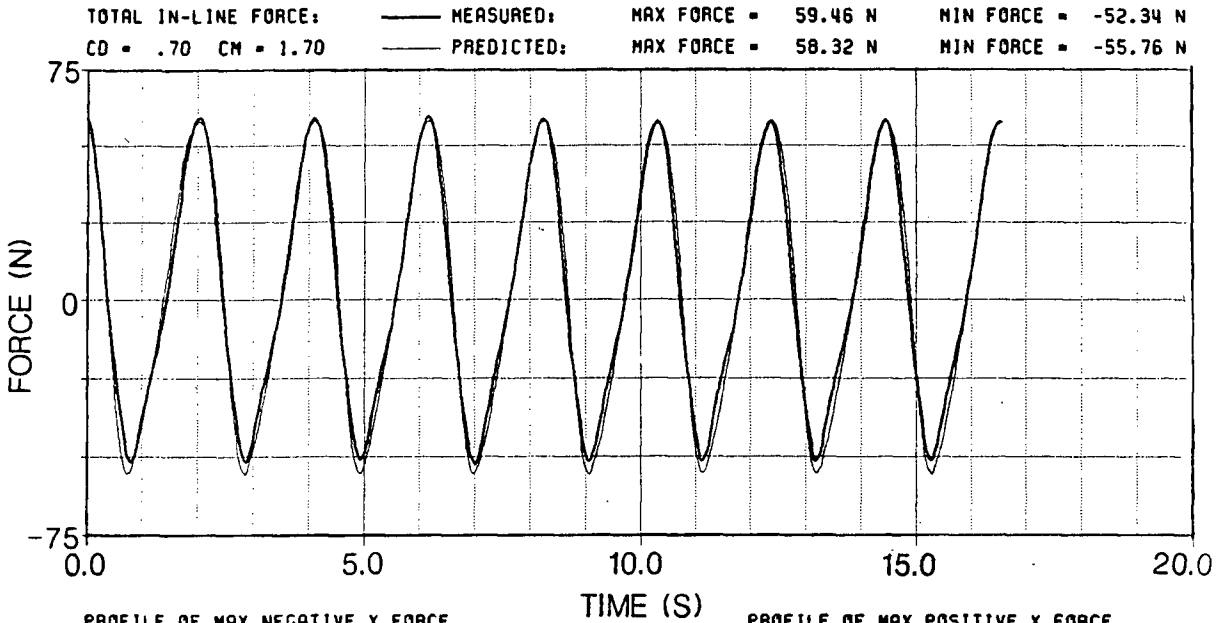
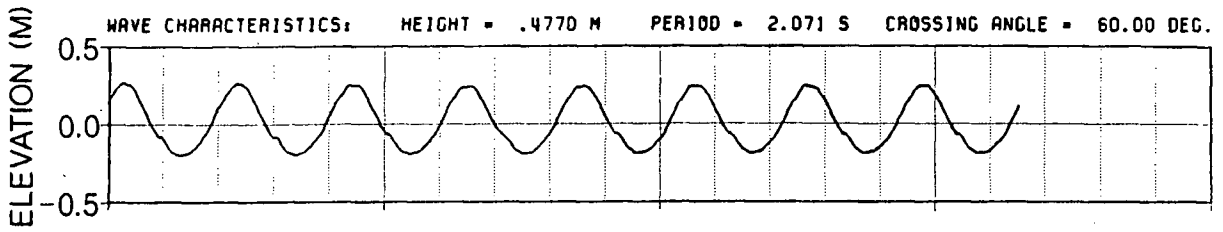


Figure 5.11: Total force comparison plot from test SC34.

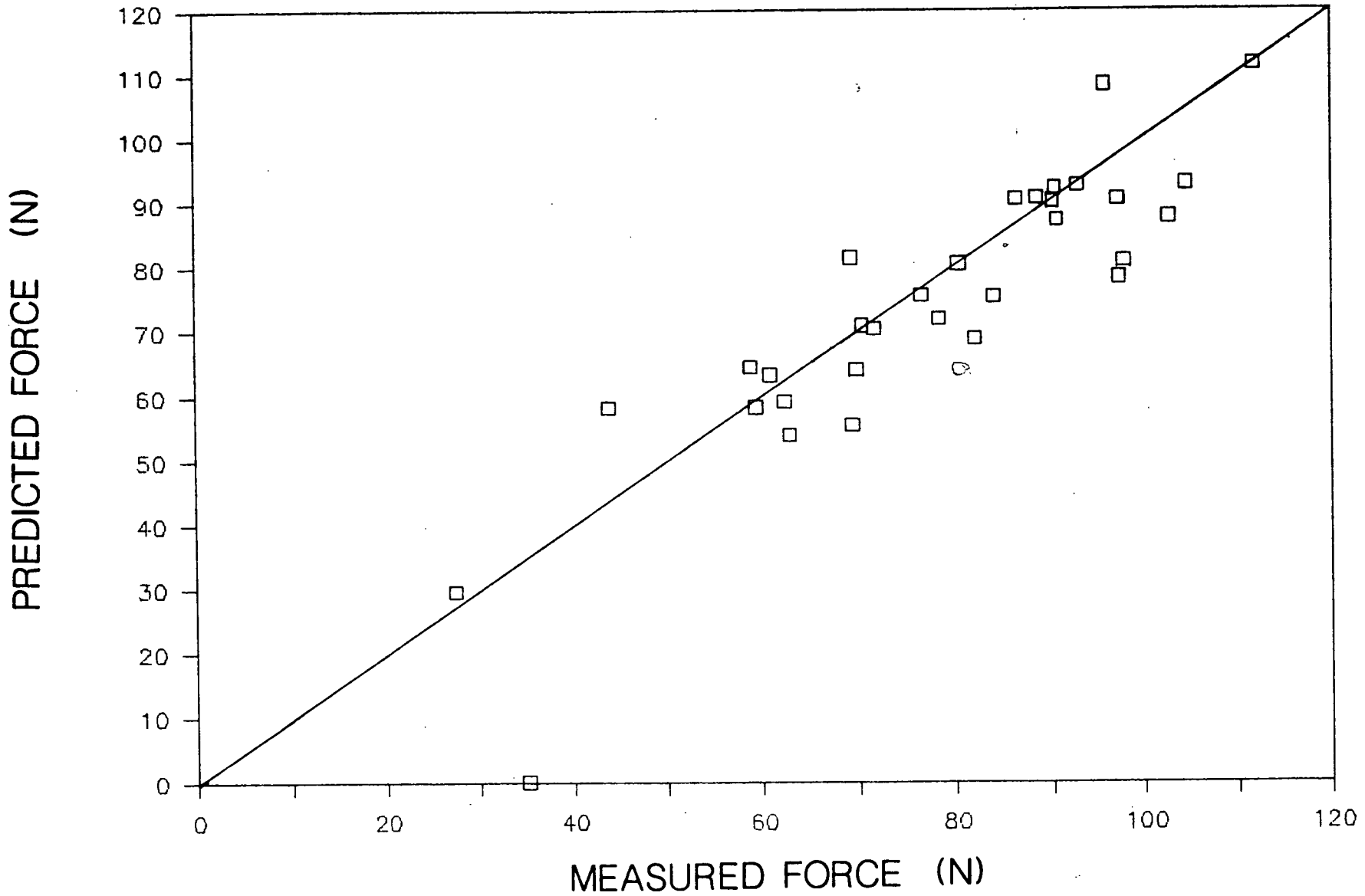


Figure 5.12: Plot of measured and predicted maximum positive total in-line forces. Data from all tests.

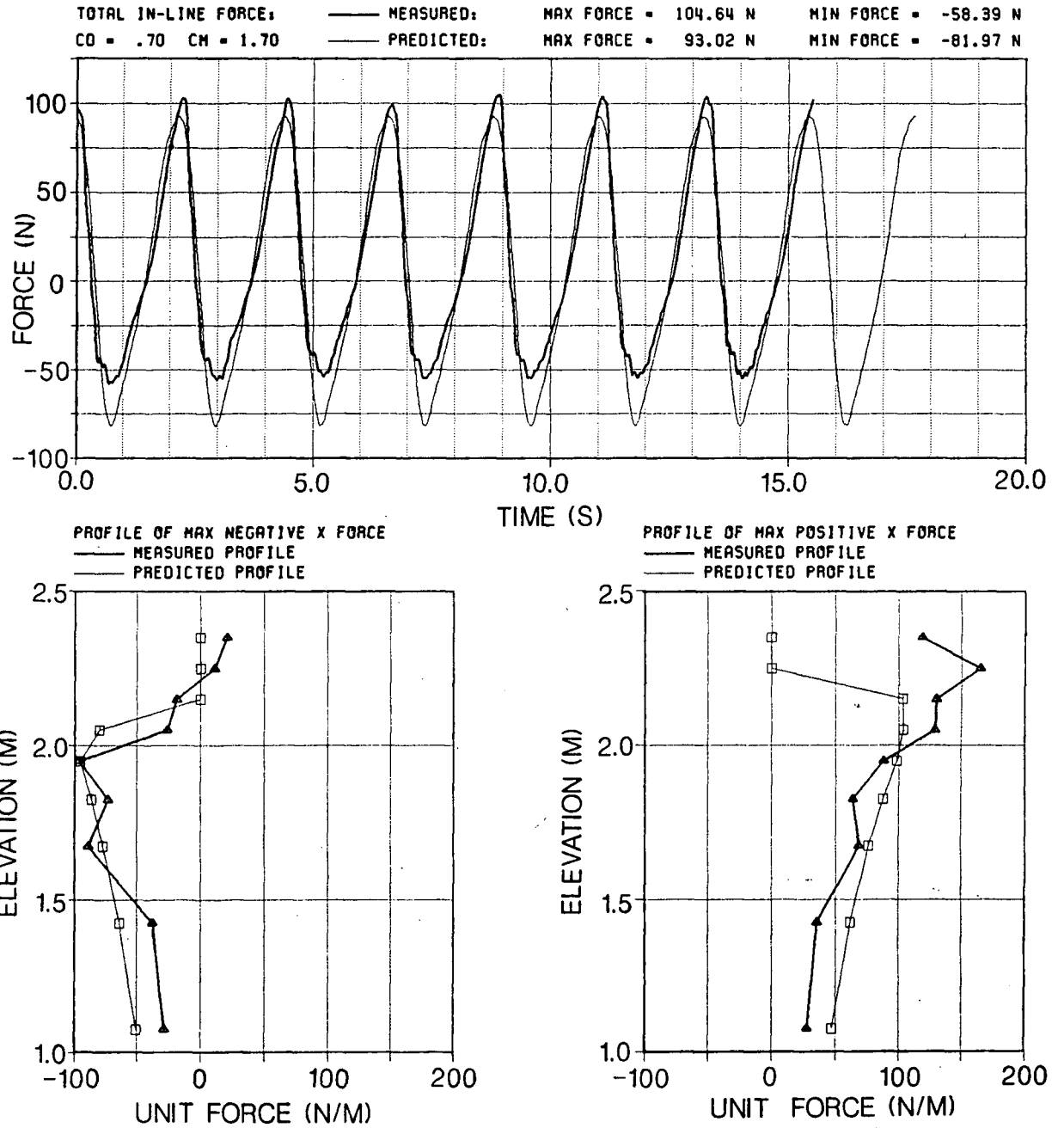


Figure 5.13: Total force comparison plot from test SB15.

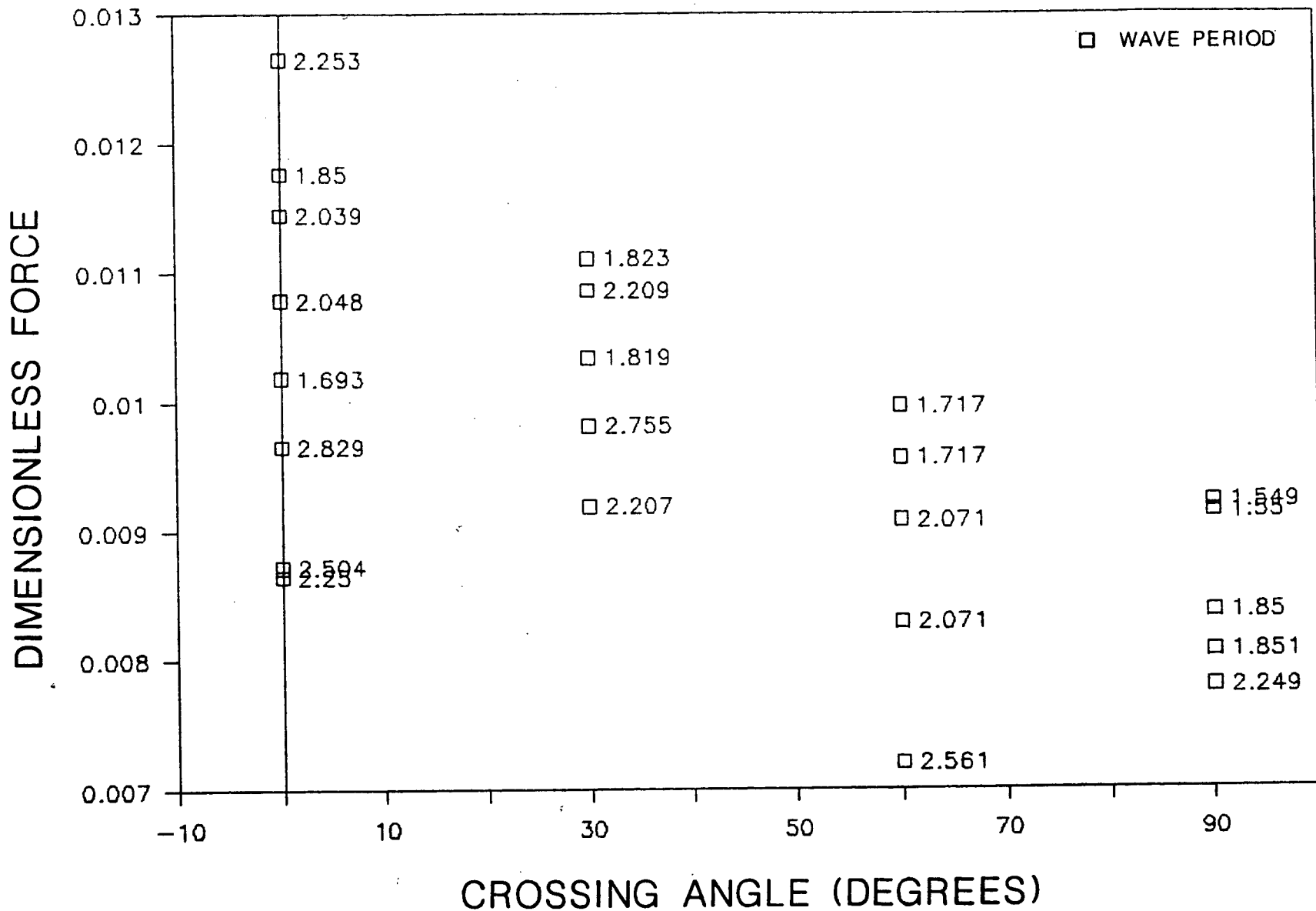


Figure 5.14: Plot of total dimensionless in-line force maxima versus crossing angle.

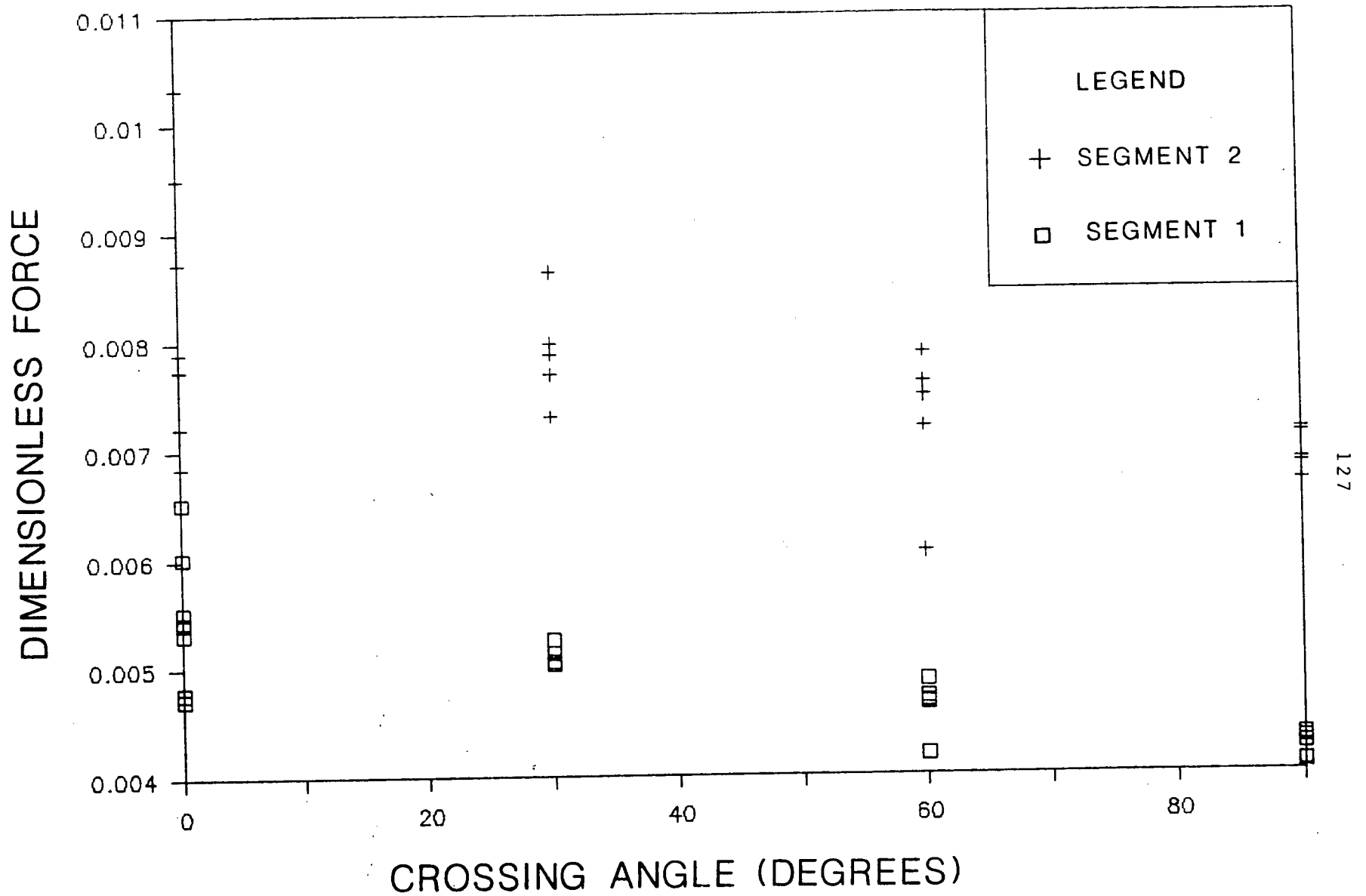


Figure 5.15: Plot of dimensionless in-line force maxima from segments 1 and 2 versus crossing angle.

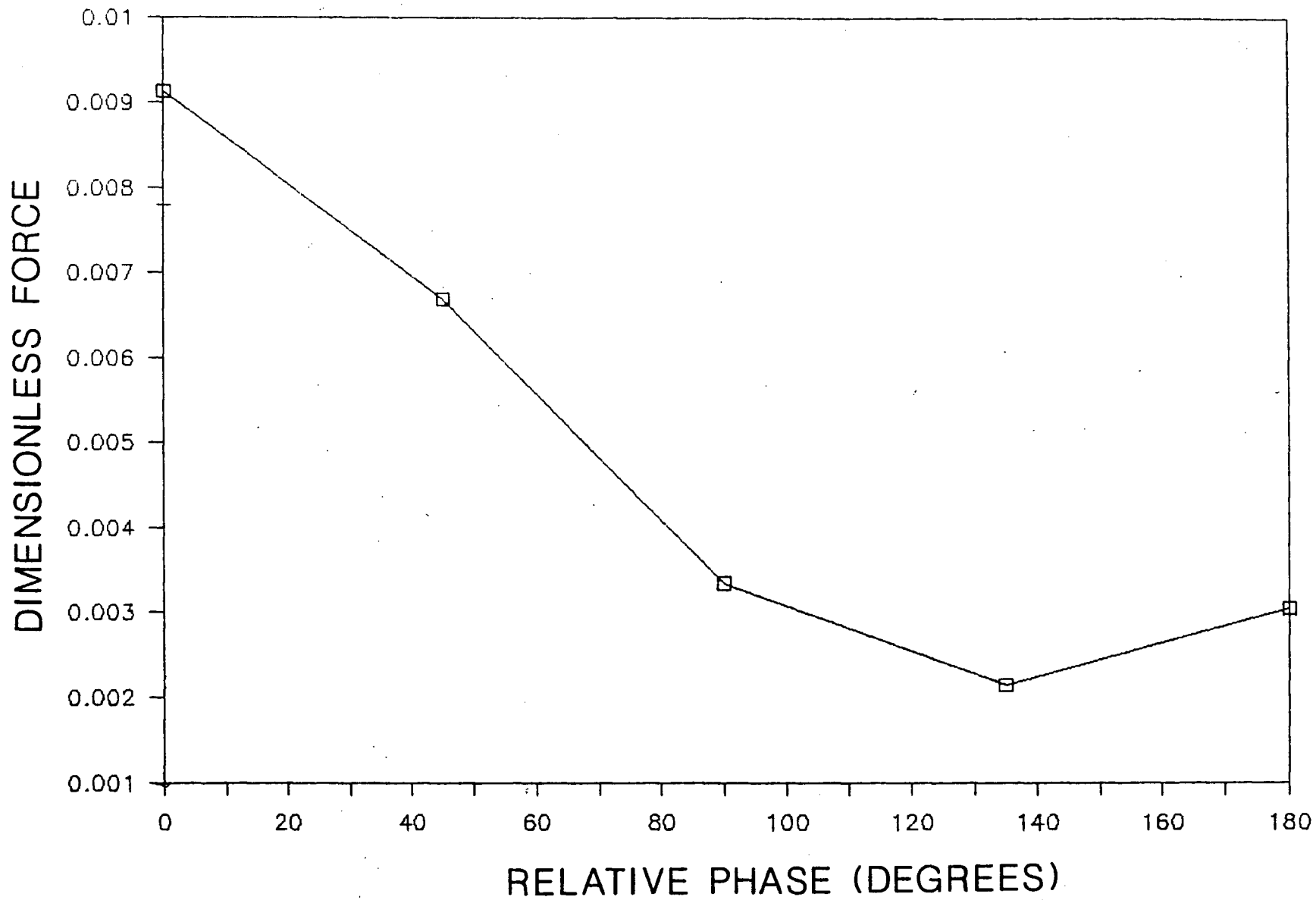


Figure 5.16: Plot of total dimensionless in-line force maxima versus phase between the two component waves.

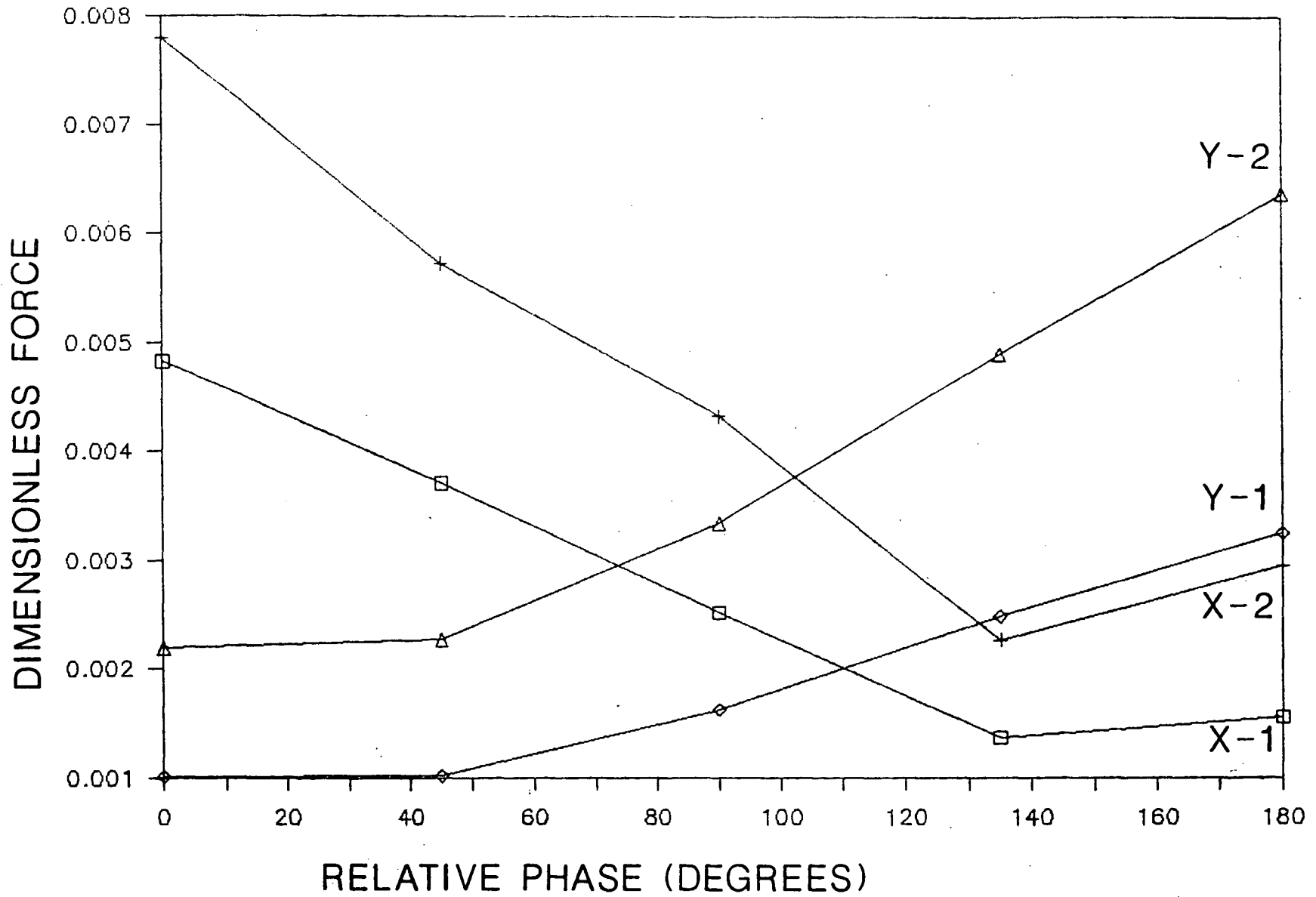


Figure 5.17: Plot of dimensionless in-line and transverse force maxima from segments 1 and 2 versus phase between the two component waves.

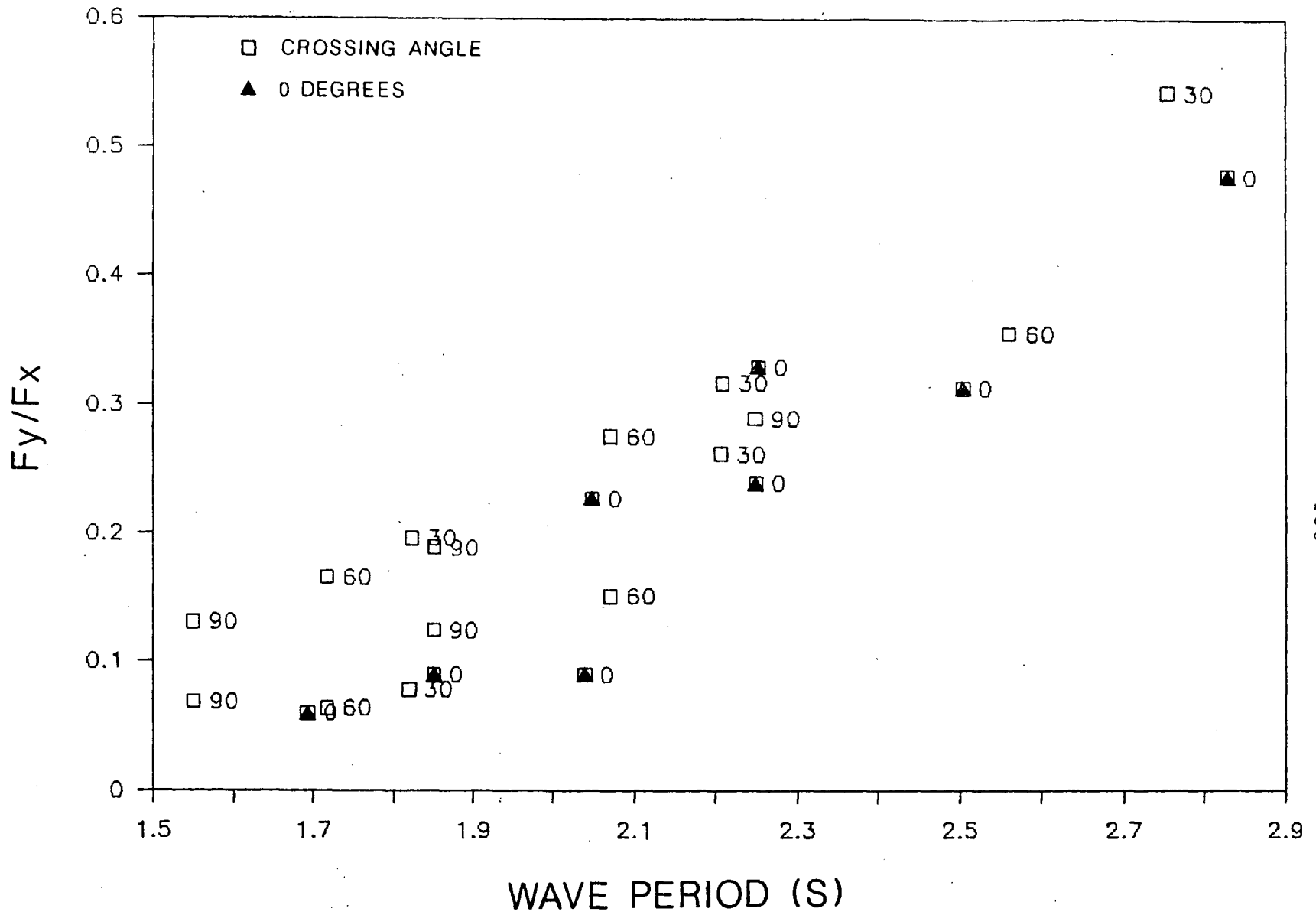


Figure 5.18: Ratio of maximum lift force to in-line force from segment 3 versus wave period.

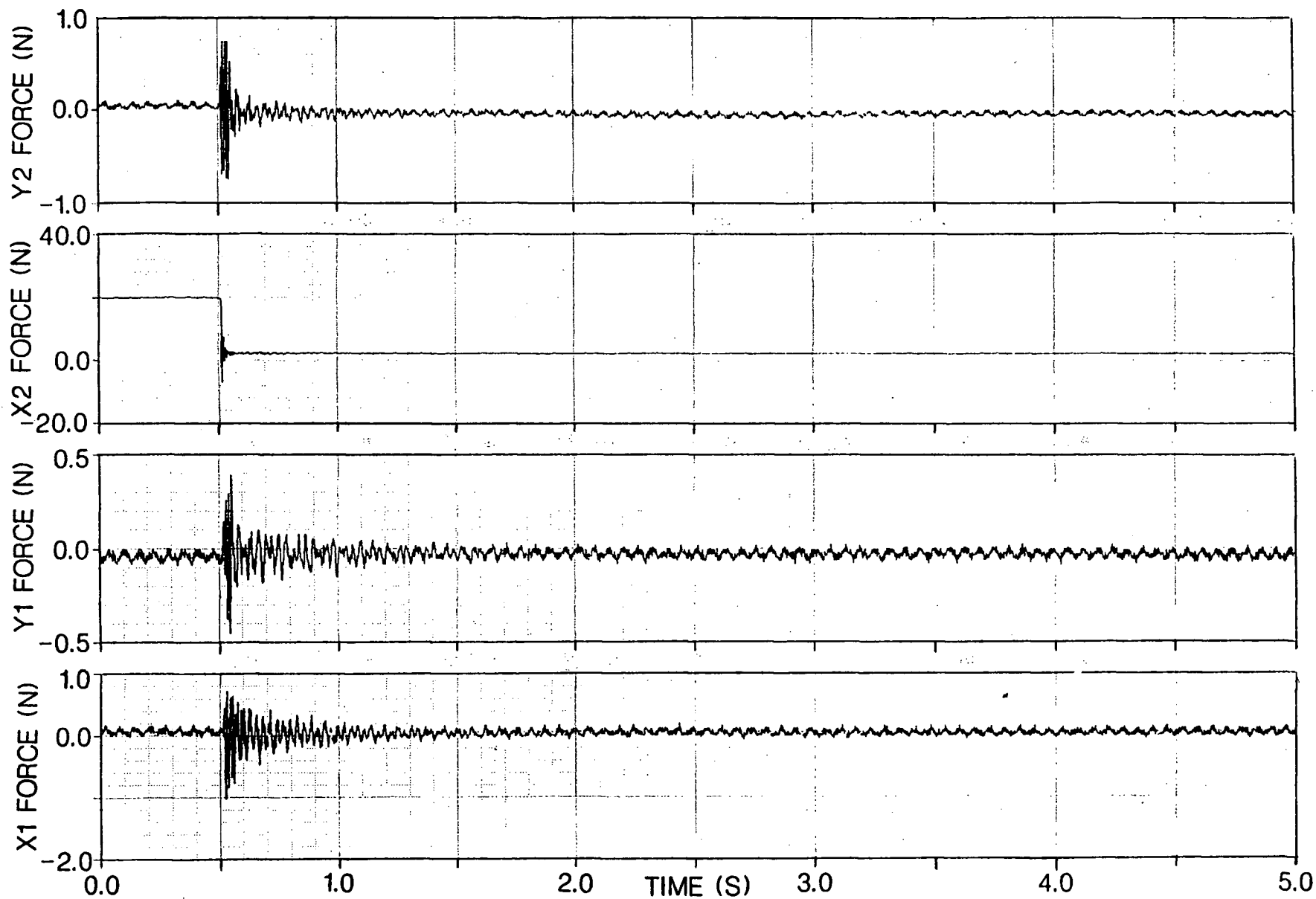


Figure A.1: Responses from initial condition testing in-line with the X axis of segment 4.

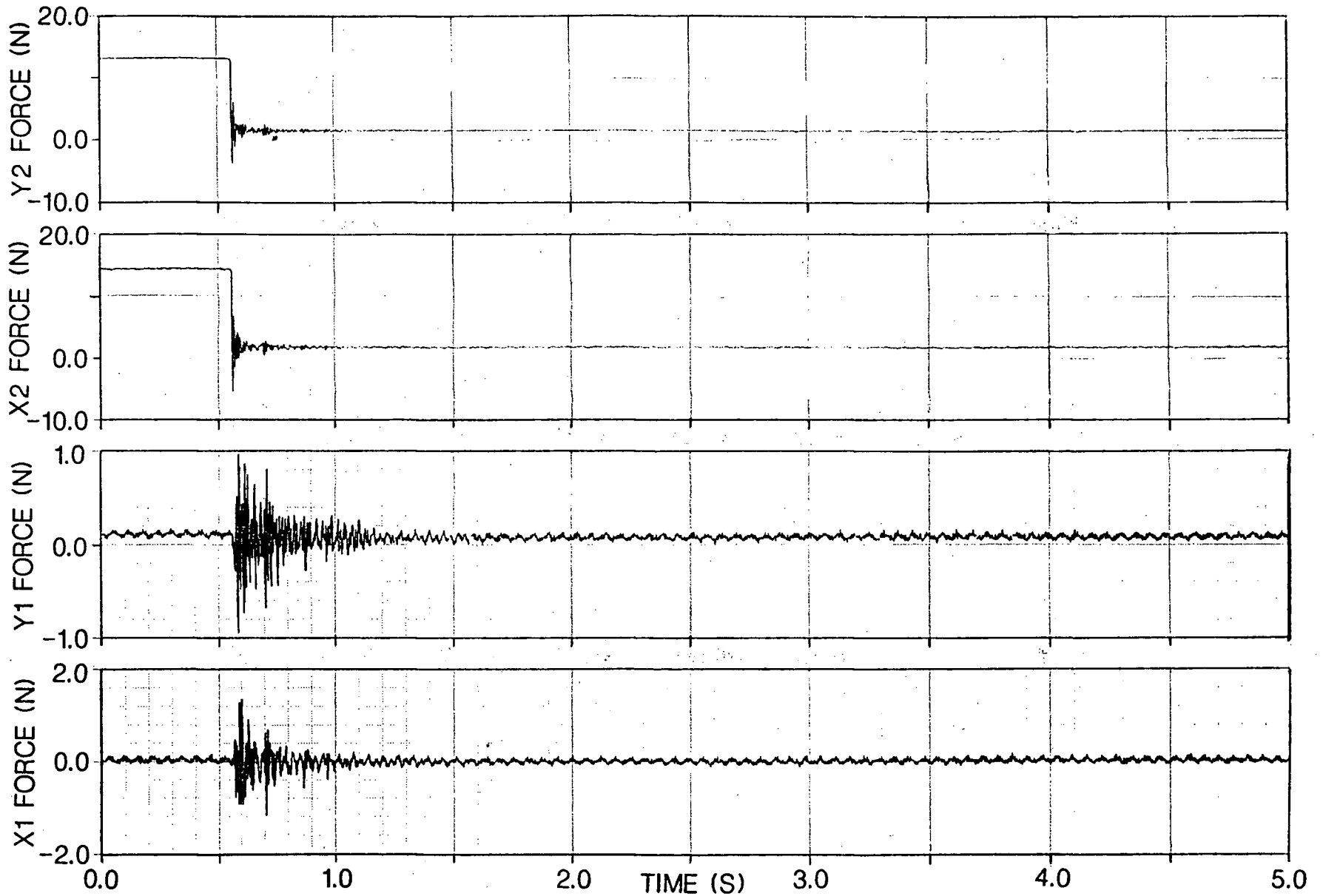


Figure A.2: Responses from initial condition testing oblique to the X and Y axes of segment 4.